

Systematic study of magnetar outbursts

Francesco Coti Zelati,^{1,2,3,4*} Nanda Rea,^{1,2} José A. Pons,⁵ Sergio Campana³
and Paolo Esposito²

¹ Institute of Space Sciences (IEEC-CSIC), Campus UAB, Carrer de Can Magrans, E-08193, Barcelona, Spain

² Anton Pannekoek Institute for Astronomy, University of Amsterdam, Postbus 94249, NL-1090-GK Amsterdam, The Netherlands

³ INAF – Osservatorio Astronomico di Brera, via Bianchi 46, I-23807 Merate (LC), Italy

⁴ Dipartimento di Scienza e Alta Tecnologia, Università dell’Insubria, via Valleggio 11, I-22100 Como, Italy

⁵ Departament de Física Aplicada, Universitat d’Alacant, Ap. Correus 99, E-03080 Alacant, Spain

Accepted 2017 October 11. Received 2017 October 11; in original form 2017 August 1

ABSTRACT

We present the results of the systematic study of all magnetar outbursts observed to date, through a reanalysis of data acquired in about 1100 X-ray observations. We track the temporal evolution of the outbursts soft X-ray spectral properties and the luminosities of the single spectral components as well as of the total emission. We model empirically all outburst light curves, and estimate the characteristic decay time-scales as well as the energetics involved. We investigate the link between different parameters (e.g., the luminosity at the peak of the outburst and in quiescence, the maximum luminosity increase, the decay time-scale and energy of the outburst, the neutron star surface dipolar magnetic field and characteristic age, etc.), and unveil several correlations among these quantities. We discuss our results in the context of the internal crustal heating and twisted bundle models for magnetar outbursts. This study is complemented by the Magnetar Outburst Online Catalogue (<http://magnetars.ice.csic.es>), an interactive data base where the user can plot any combination of the parameters derived in this work, and download all data.

Key words: methods: data analysis – methods: observational – techniques: spectroscopic – stars: magnetars – stars: magnetic field – X-rays: stars

1 INTRODUCTION

Magnetars are strongly magnetized (up to $B \sim 10^{14} - 10^{15}$ G) isolated X-ray pulsars with luminosities $L_X \sim 10^{31} - 10^{36}$ erg s⁻¹. They rotate at comparatively long periods ($P \sim 0.3 - 12$ s) with respect to the general pulsar population, and are typically characterized by large secular spin-down rates ($\dot{P} \sim 10^{-15}$ to 10^{-10} s s⁻¹). According to the magnetar scenario, their emission is ultimately powered by the decay and the instability of their ultra-strong magnetic field (e.g. Duncan & Thompson 1992; Paczyński 1992; Thompson & Duncan 1993, 1995, 1996, 2001; see Turolla, Zane & Watts 2015 and Kaspi & Beloborodov 2017 for recent reviews). The hallmark of magnetars is the unpredictable and highly variable bursting/flaring activity in the X-/gamma-ray energy range, which encompasses a wide interval of time-scales (from a few milliseconds up to tens of seconds) and luminosities ($10^{39} - 10^{47}$ erg s⁻¹ at the peak; Turolla et al. 2015). The bursting episodes are often accompanied by large and rapid enhancements of the persistent X-ray emission (typically by a factor of $\sim 10 - 1000$), which then decline and attain the quiescent level on a time-scale ranging from

a few weeks up to several years. We will refer to these phases as outbursts, to distinguish from the bursting/flaring activity (see Rea & Esposito 2011, for an observational review).

At the moment of writing (2017 July), 26 isolated X-ray pulsars have unambiguously shown magnetar-like activity, including the rotation-powered pulsars PSR J1846–0258 and PSR J1119–6127 (Gavriil et al. 2008; Kumar & Safi-Harb 2008; Kuiper & Hermsen 2009; Archibald et al. 2016a; Göğüş et al. 2016; Archibald et al. 2017a), the low-field magnetars SGR 0418+5729 and Swift J1822.3–1606 (e.g., Rea et al. 2010, 2012a), and the central compact object 1E 161348–5055 (D’Aì et al. 2016; Rea et al. 2016). These discoveries demonstrate how magnetar activity might have a larger spread within the neutron star population.

The soft X-ray ($\lesssim 10$ keV) emission of magnetars is typically well described by a combination of a thermal component (a black-body with temperature $kT \sim 0.3 - 0.9$ keV) plus a power law with photon index $\Gamma \sim 2 - 4$, commonly interpreted in terms of repeated resonant cyclotron up-scattering of thermal photons from the star surface on to charged particles flowing in a twisted magnetosphere (e.g., Thompson, Lyutikov & Kulkarni 2002; Nobili, Turolla & Zane 2008a,b). In some cases, a multiple-blackbody model provides an adequate description as well, and it is usually ascribed to thermal emission from regions of different temperature and size

* E-mail: cotizelati@ice.csic.es

on the star surface (e.g., Tiengo, Esposito & Mereghetti 2008; Alford & Halpern 2016).

In the last decades and especially following the advent of the new generation of imaging instruments on board *Swift*, *Chandra* and *XMM-Newton*, several magnetar outbursts were monitored in the X-rays, leading to a number of unexpected breakthroughs which have changed our understanding of these strongly magnetized neutron stars (Turolla et al. 2015; Kaspi & Beloborodov 2017). The large field of view (FoV) and the fast response of the *Swift* satellite proved (and still prove) to be key ingredients to spot the bursting/flaring activity of magnetars and precisely track spectral variations since the very first active phases and on time-scales ranging from days to months. *Chandra* and *XMM-Newton* have revealed to be of paramount importance to characterize adequately the X-ray emission of faint outbursts particularly at later stages, thanks to dedicated follow-up observational programmes and the large collecting area of their instruments. In some cases, the monitoring campaigns covered the whole outburst evolution, and disclosed the source quiescent level. Although the cooling pattern varies significantly from outburst to outburst, the spectral softening throughout the decay seems an ubiquitous characteristic for these events (Rea & Esposito 2011).

1.1 Magnetar outbursts: mechanisms

Although it is widely accepted that magnetar outbursts are attributable to some form of heat deposition in a restricted region of the star surface which then cools, the mechanism responsible for their activation, as well as the energy supply responsible for sustaining their long-term emission, still remain somewhat elusive. They are probably triggered by local internal magnetic stresses strong enough to deform irreversibly part of the stellar crust, possibly in the form of a prolonged avalanche of plastic failures (Li, Levin & Beloborodov 2016). An additional contribution may be provided by magnetospheric Alfvén waves created during flaring activity (Parfrey, Beloborodov & Hui 2013). According to Li & Beloborodov (2015), these waves are impulsively transmitted inside the star, and induce a strong oscillating plastic flow in the crust that subsists for a few ms, after which the waves are damped.

Regardless of the triggering mechanism, the plastic flows induced in the crust lead to transient thermoplastic waves that move the crust, convert mechanically its magnetic energy into heat and relieve the stresses (Beloborodov & Levin 2014). A fraction of the deposited heat is then conducted up to the surface and radiated, producing a delayed thermal afterglow emission that can be sustained up to a few years, also depending on the flare rate (see also Beloborodov & Li 2016). The crustal cooling time-scale chiefly depends on the thermal properties of the outer crust, the depth at which the energy is released and the neutrino emission processes operating in the crust (Pons & Rea 2012; Li et al. 2016). Moreover, the crustal displacements implant a strong external magnetic twist, presumably confined to a bundle of current-carrying closed field lines anchored in the crust. Additional heating of the surface layers is then produced as the currents flowing along the field lines of the twisted bundle impact upon the star (e.g. Thompson et al. 2002; Beloborodov & Thompson 2007; Beloborodov 2009). As the energy reservoir stored in the star interior is progressively depleted, the twist must decay to support its currents. Consequently, the spatial extent of the bundle gets gradually more and more limited, the area on the star surface hit by the charges shrinks and the luminosity decreases. The time-scale of the resistive untwisting can be of the order of a few years if the crustal motions take place at high lati-

tudes and the footpoints of the bundle are positioned close to the magnetic poles (Beloborodov 2009).

Both heating mechanisms – internal and external – are likely at work during outbursts.

1.2 Motivation of the study and plan of the paper

Although several detailed studies were conducted for each of these events, an overall systematic and homogeneous analysis of the spectral properties of these stars, from the very first active phases of their outbursts throughout their decays, is still missing. A systematic reanalysis of all data sets is required to compare properly these properties, model accurately the outbursts cooling curves in a consistent way and unveil possible correlations among different parameters such as maximum luminosity, quiescent luminosity, luminosity increase during the outburst, energetics, decay time-scale, magnetic field, rotational energy loss rate and age.

This paper presents the results of the X-ray spectral modelling for 23 magnetar outbursts from 17 different sources using all the available data acquired by the *Swift*, *Chandra* and *XMM-Newton* X-ray observatories, as well as data collected in a handful of observations by the instruments aboard *BeppoSAX*, *Roentgen Satellite (ROSAT)* and *RXTE*. This sums up to about 1100 observations, for a total dead-time corrected on source exposure time of more than 12 Ms. The paper is structured as follows: in Section 2 we introduce the sample of magnetars considered in this study, and the monitoring campaigns that were activated following the detection of their outbursts. In Section 3 we describe the data reduction and extraction procedures. In Section 4 we report details on the spectral analysis. In Section 5 we exploit the results of our analysis to extract the light curves for each outburst and estimate the outburst energetics and decay time-scale. In Section 6 we report on accurate estimates of peak and quiescent luminosities of magnetars, including those showing only subtle variability on top of their persistent emission. In Section 7 we present the results of a search for possible (anti)correlations between several different parameters. In Section 8 we discuss the results of our study. A brief description of the Magnetar Outburst Online Catalogue (MOOC) follows in Section 9. The results of the detailed modelling of the outbursts evolution with physically motivated models will be presented in a forthcoming work.

2 THE SAMPLE

This section summarizes the properties of the 17 magnetars that so far have undergone at least one outburst. The sources are listed according to the chronological order of their (first) outburst activation, except for the three sources PSR J1119–6127, PSR J1846–0258 and 1E 161348–5055, which are described at the end of the section. Details about the prompt and follow-up X-ray observations used in this work are reported in a series of tables in Appendix A. In the following, all the values reported for the magnetic field are computed using the spin-down formula for force-free magnetospheres by Spitkovsky (2006), and assuming an aligned rotator. They refer to the dipolar component of the magnetic field at the polar caps (this is a factor of ~ 2 larger than the value computed at the equator).

2.1 SGR 1627–41

SGR 1627–41 was discovered on 1998 June 15 (Kouveliotou et al. 1998), when three consecutive bursts were detected by the Burst

and Transient Source Experiment (BATSE) aboard the *Compton Gamma Ray Observatory*. More than 100 bursts were recorded from the same location within the subsequent 6 weeks, and the X-ray counterpart was identified 2 months later by the narrow field instruments on board *BeppeSAX* (Woods et al. 1999). The burst detections marked the onset of an outburst, which gradually recovered the quiescent level over the course of the ensuing decade (see Table A1).

On 2008 May 28 the Burst Alert Telescope (BAT; Barthelmy et al. 2005) aboard *Swift* triggered on dozens of bursts from SGR 1627–41 (Palmer et al. 2008). A conspicuous enhancement of the persistent X-ray flux was measured (a factor of about 100 larger with respect to 3 months and a half before), and the magnetar nature of the source was incontrovertibly settled with the detection of 2.59-s X-ray pulsations in *XMM-Newton* data sets (with $\dot{P} \sim 1.9 \times 10^{-11} \text{ s s}^{-1}$; Esposito et al. 2009b). Table A6 reports the log of the X-ray observations carried out after the second outburst. We assume a distance of 11 kpc throughout the paper.

2.2 1E 2259+586

After more than two decades of rather persistent X-ray emission since its discovery at the centre of the supernova remnant (SNR) G109.1-1.0 (CTB 109) in 1979 December (Fahlman & Gregory 1981), the 6.98-s X-ray pulsar 1E 2259+586 attracted attention on 2002 June 18, when more than 80 bursts were detected within 3 h of observing time by the *Rossi X-ray Timing Explorer* (*RXTE*), and the persistent flux rose by a factor of ~ 10 compared to the quiescent level (Kaspi et al. 2003). Eight *XMM-Newton* observations were carried out to study the subsequent evolution of the outburst (see Table A2).

Nearly 10 yr later, on 2012 April 21, the Gamma-ray Burst Monitor (GBM) on board *Fermi* triggered on a single 40-ms long event (Foley et al. 2012), which was accompanied by an increase in the soft X-ray flux (as observed about a week later by the X-ray Telescope (XRT) on board *Swift*; see Table A16 for a journal comprising this and all the follow-up observations of the first ~ 1400 d since the outburst onset). We assume a distance of 3.2 kpc throughout the paper.

2.3 XTE J1810–197

Originally a soft and faint X-ray source serendipitously recorded by the *ROSAT* during four observations between 1991 and 1993, the transient nature of XTE J1810–197 was disclosed in 2003, when the *RXTE* detected it at an X-ray flux a factor about 100 larger with respect to the pre-outburst level. X-ray pulsations were measured at a period of 5.54 s (Ibrahim et al. 2004). Radio pulsations at the spin period were detected in 2006 (about 3 yr later), a property never observed before in any other magnetar, which definitely proved that pulsed radio emission could be produced even in sources with magnetar-strength fields (Camilo et al. 2006). Although the initial phases of the outburst were missed, XTE J1810–197 has been studied in great detail over the last 12 yr, especially with the *XMM-Newton* observatory and up to the return to quiescence (see Table A3)¹. We assume a distance of 3.5 kpc throughout the paper.

¹ The source was observed also with *Chandra* for 12 times and with *Swift* for 5 times. We focus here on the *XMM-Newton* pointings alone, because they provide a good coverage of the whole outburst evolution down to the quiescent level, as well as the spectra with the largest counting statistics.

2.4 SGR 1806–20

Initially catalogued as a classical γ -ray burst (GRB 790107) based on observations by the *Konus* experiment (Mazets et al. 1981) and other all-sky monitors of the interplanetary network (Laros et al. 1986), SGR 1806–20 was recognized to be a member of a distinct class of astrophysical transients after the detection of more than 100 bursts of soft γ -rays between 1979 and 1986 (Laros et al. 1987). Two observations were carried out by the *Advanced Satellite for Cosmology and Astrophysics* (*ASCA*) soon after an intense bursting activity in 1993 October (as unveiled by BATSE), leading to the identification of a previously uncatalogued, persistent, point-like X-ray counterpart (Murakami et al. 1994; Sonobe et al. 1994). The spin period, ~ 7.5 s, was measured in 1996 November by means of five *RXTE* observations that were performed following another reactivation of the source (Kouveliotou et al. 1998).

SGR 1806–20 experienced an exceptionally intense flare on 2004 December 27 with a peak luminosity of a few $10^{47} \text{ erg s}^{-1}$ (for a distance of 8.7 kpc and under the assumption of isotropic emission; Hurley et al. 2005; Palmer et al. 2005), which then decayed by a factor of ~ 50 per cent, and stabilized at an approximately steady level over the subsequent 7 yr (Younes, Kouveliotou & Kaspi 2015). Table A4 reports a log of all 10 *XMM-Newton* observations tracking the post-flare evolution (no *Swift* observations were performed during the first 2 months of the outburst). We assume a distance of 8.7 kpc throughout the paper.

2.5 CXOU J164710.2–455216

CXOU J164710.2–455216 was discovered in 2005 during an X-ray survey of the young cluster of massive stars Westerlund 1, and tentatively identified as a magnetar candidate based on the value of its spin period, 10.61 s, and the X-ray spectral properties (Muno et al. 2006). The case was clinched the following year, when a rather intense burst lasting about 20 ms was fortuitously detected by the *Swift* BAT from the direction of the source, on 2006 September 21 (Krimm et al. 2006). This episode was indeed associated with an abrupt enhancement of the X-ray flux, which marked the onset of a magnetar-like outburst. Table A5 reports a summary of all follow-up X-ray observations.

The source underwent another weaker outburst on 2011 September 19, when four more sporadic bursts were detected from the source position (Baumgartner et al. 2011; Rodríguez Castillo et al. 2014). Table A14 lists the few X-ray observations of this outburst. We assume a distance of 4 kpc throughout the paper.

2.6 SGR 0501+4516

SGR 0501+4516 joined the magnetar family on 2008 August 22, after the *Swift* BAT detection of a series of short bursts of soft γ -rays (< 100 keV; Barthelmy et al. 2008) and the discovery of pulsations at a period of 5.76 s from the X-ray counterpart (Gögüs et al. 2008). The source continued to be active over the following 36 h, showing a total of about 30 bursts. It was soon recognized that the bursting activity was related to the onset of an outburst, and several X-ray observations were promptly undertaken (see Table A7). We assume a distance of 1.5 kpc throughout the paper.

ties. Note that a recent *Swift* XRT observation performed in 2017 February caught the source again at the historical quiescent flux.

2.7 1E 1547–5408

Discovered by the *Einstein* satellite on 1980 March 2 during a search for X-ray counterparts of unidentified γ -ray sources (Lamb & Markert 1981), 1E 1547–5408 (aka SGR 1550–5418) was later suspected to be a magnetar candidate based on its X-ray spectral properties, the observed long-term X-ray variability between 1980 and 2006, and its putative association with the SNR G327.24–0.13 (Gelfand & Gaensler 2007). The ‘smoking gun’ in favour of this classification came with the measurement of 2.07-s pulsations from the radio counterpart (Camilo et al. 2007), later confirmed also in the X-rays (Halpern et al. 2008).

On 2008 October 3, the *Swift* BAT triggered on and localized a short burst from a position consistent with that of 1E 1547–5408 (Krimm et al. 2008). *Swift* executed a prompt slew, and the XRT started observing the field only 99 s after the BAT trigger, catching the source at a flux a factor about 20 above that in quiescence (see Table A8 for the log of all the follow-up X-ray observations).

No further bursts were reported until 2009 January 22, when the source resumed a new state of extreme bursting activity (Connaughton & Briggs 2009; Gronwall et al. 2009), culminating in a storm of more than 200 soft γ -ray bursts recorded by the *International Gamma-Ray Astrophysics Laboratory* (*INTEGRAL*) in a few hours (Mereghetti et al. 2009), and characterized by a considerable increase in the persistent X-ray flux. The source was repeatedly observed in the X-rays after the burst trigger (especially with *Swift*), leading to one of the most intensive samplings of a magnetar outburst ever performed (see Table A9)². We assume a distance of 4.5 kpc throughout the paper.

2.8 SGR 0418+5729

SGR 0418+5729 was discovered after the detection of a couple of short hard X-ray bursts on 2009 June 5 with *Fermi* GBM and other instruments sensitive to the hard X-ray range (van der Horst et al. 2010). Coherent X-ray pulsations were observed at a period of 9.1 s 5 d later during an *RXTE* pointing (Göögüs et al. 2009). Since then, *Swift*, *Chandra* and *XMM-Newton* observed the field of the new source for a total of 39 pointings (see Table A10). It took more than 3 yr of continuous monitoring to establish unambiguously the first derivative of the spin period, making this source the magnetar with the lowest inferred surface dipolar magnetic field known to date, $\sim 1.2 \times 10^{13}$ G (Rea et al. 2013a). We assume a distance of 2 kpc throughout the paper.

2.9 SGR 1833–0832

SGR 1833–0832 was discovered on 2010 March 19, when the *Swift* BAT triggered on and localized a short (<1 s) hard X-ray burst in a region close to the Galactic plane (Gelbord et al. 2010;

² *Swift* and *XMM-Newton* observations performed from 2007 June to October caught the magnetar while recovering from another outburst likely occurred prior to 2007 June (Halpern et al. 2008). We do not include the analysis of this outburst in this study owing to the unknown epoch of the episode onset and the sparse X-ray coverage. Our analysis of the 2009 event is limited to the first 1000 d of the outburst, but the source is currently being observed by *Swift*. However, a preliminary extraction of the long-term light curve with the *Swift* online tool (see below), reveals an extremely slow decay which is consistent with the extrapolation of our long-term light curve, giving no significant differences in the estimate of the total energetics and decay time-scale.

Göögüs et al. 2010a) and the fast slew of the XRT promptly detected a previously unnoticed 7.57-s X-ray pulsator (Göögüs et al. 2010a; Esposito et al. 2011). Starting right after its discovery, *Swift* and *XMM-Newton* pointed their instruments towards the source multiple times for the first ~ 160 d of the outburst decay (see Table A11). We assume an arbitrary distance of 10 kpc throughout the paper.

2.10 Swift J1822.3–1606

On 2011 July 14, the detection of a magnetar-like burst by the *Swift* BAT and of an associated bright and persistent XRT counterpart heralded the existence of a new magnetar, Swift J1822.3–1606 (Cummings et al. 2011), with a spin period of 8.43 s (Göögüs et al. 2011a). Swift J1822.3–1606 was densely monitored in the X-rays until 2012 November 17, covering a time span of ~ 1.3 yr (see Table A12). With an estimated surface dipolar magnetic field of $\sim 6.8 \times 10^{13}$ G (Rodríguez Castillo et al. 2016, and references therein), it also belongs to the sub-class of the so called ‘low- \dot{P} magnetars’. We assume a distance of 1.6 kpc throughout the paper.

2.11 Swift J1834.9–0846

The BAT aboard *Swift* was triggered by a short SGR-like burst on 2011 August 7 (D’Elia et al. 2011). This episode was not isolated: a second burst from the same direction on the sky was recorded by the *Fermi* GBM approximately 3.3 h later (Guiriec et al. 2011), and another similar event triggered the BAT again on August 29 (Hovesten et al. 2011). The magnetar nature of this newly discovered source was nailed down with the discovery of pulsations at 2.48 s from the X-ray counterpart (Göögüs & Kouveliotou 2011). *Swift*, *Chandra* and *XMM-Newton* observed this new SGR for a total of 25 times since the first burst detection (see Table A13).

Swift J1834.9–0846 represents a unique case among magnetars. It is indeed embedded in a patch of diffuse X-ray emission with a complex spatial structure consisting of a symmetric component within ~ 50 arcsec around the magnetar, and an asymmetric component stretched towards the south-west of the point source and extending up to ~ 150 arcsec. The former was interpreted as a halo created by the scattering of X-rays by intervening dust (dust-scattering halo; Kargaltsev et al. 2012; Esposito et al. 2013). The latter was attributed to a magnetar-powered wind nebula based on its highly absorbed power law-like X-ray spectrum, the flux constancy and the absence of statistically significant variations in the spectral shape over a time span of 9 yr, between 2005 and 2014 (Younes et al. 2016). Swift J1834.9–0846 would then provide the first observational evidence for the existence of wind nebulae around magnetically powered pulsars (see also Granot et al. 2017; Torres 2017). We assume a distance of 4.2 kpc throughout the paper.

2.12 1E 1048.1–5937

The discovery of 1E 1048.1–5937 dates back to 1979 July 13, when *Einstein* detected 6.44-s pulsed X-ray emission from a point-like source in the Carina Nebula (Seward, Charles & Smale 1986). With five long-term outbursts shown to date, this source holds the record as the most prolific outbursting magnetar hitherto known. The first three flux enhancements were observed in 2001, 2002 and 2007 by *RXTE*, which monitored this source about twice per month from 1999 February to 2011 December (see Dib & Kaspi

2014 and references therein). An additional flux increase was observed in 2011, and the subsequent evolution was the object of a prolonged monitoring campaign with *Swift*, to which two *Chandra* and one *XMM–Newton* observations have to be added (see Table A15 for the observations of the first ~ 1000 d of the outburst decay). The last outburst from this source dates back to 2016 July 23 (Archibald et al. 2016b), and its evolution was again densely monitored thanks to the ongoing *Swift* campaign (see Table A19). The outbursts are remarkably periodic, with a recurrence time of about 1800 d (Archibald et al. 2015). In this study we focus on the last two outbursts. We assume a distance of 9 kpc throughout the paper.

2.13 SGR 1745–2900

At a projected separation of ~ 0.1 pc from the supermassive black hole at the Centre of the Milky Way, Sagittarius A* (hereafter Sgr A*), the magnetar SGR 1745–2900 is the closest neutron star to a black hole ever observed, and it spins at a period of about 3.76 s (e.g., Coti Zelati et al. 2015a, 2017). According to numerical simulations and to the recently detected proper motion, it is likely in a bound orbit around Sgr A* (Rea et al. 2013b; Bower et al. 2015).

SGR 1745–2900 is the object of an ongoing intensive monitoring campaign by *Chandra* (see Table A17), still more than 3 yr after the detection of the first ~ 30 ms long soft gamma-ray burst from the source on 2013 April 25 (Kennea et al. 2013a). We assume a distance of 8.3 kpc throughout the paper.

2.14 SGR 1935+2154

The most recent addition to the magnetar class is represented by SGR 1935+2154, whose existence was announced on 2014 July 5 once more through the detection of low-Galactic latitude short bursts by *Swift* BAT (Stamatikos et al. 2014). A deep follow-up observation carried out by *Chandra* enabled to determine its spin period (3.24 s; Israel et al. 2014), and the post-outburst behaviour was then observed with *Swift*, *Chandra* and *XMM–Newton*. On 2015 February 22 the BAT triggered on another burst from the source (D’Avanzo et al. 2015), which led to further monitoring through 14 observations with *Swift* and two with *XMM–Newton*. Another 50-ms long burst was detected in 2015 December by *INTEGRAL* in the soft gamma rays (Mereghetti et al. 2015), albeit no concurrent increase in the X-ray emission over the long-term behaviour was observed (Coti Zelati et al. 2015b). The source reactivated once more on 2016 May 16 (Barthelmy et al. 2016), and bursting activity was observed over the following ~ 5 d. Some of these flux enhancements were recently studied in detail by Younes et al. (2017). See Table A18 for the log of the observations. We assume a distance of 9 kpc throughout the paper.

2.15 PSR J1119–6127

The 0.4-s radio pulsar PSR J1119–6127 was discovered in the Parkes multibeam 1.4-GHz survey (Camilo et al. 2000), and it is likely associated with the SNR G292.2–0.5 (Crawford et al. 2001). The dipolar surface magnetic field implied by the timing parameters is about 8.2×10^{13} G, among the highest known among radio pulsars. On 2016 July 27 and 28 two magnetar-like bursts signalled the onset of an outburst from this source (Archibald et al. 2016a; Kennea et al. 2016; Younes, Kouveliotou & Roberts 2016). Table A20 lists the follow-up *Swift* observations analysed in this work.

Interestingly, simultaneous radio and X-ray observations about 1 month after the outburst onset revealed a significant anticorrelation between the emission in the two bands: the rotation-powered radio emission switched off during periods of multiple magnetar-like X-ray bursts (Archibald et al. 2017a). We assume a distance of 8.4 kpc throughout the paper.

2.16 PSR J1846–0258

PSR J1846–0258 is a young (<1 kyr) rotation-powered pulsar located at the centre of the SNR Kesteven 75 (Gotthelf et al. 2000). It rotates at a period of ~ 326 ms (Livingstone et al. 2011a) and is endowed with a surface dipolar magnetic field of $\sim 1 \times 10^{14}$ G, which is higher than the vast majority of rotation-powered pulsars. On 2006 June 8 several magnetar-like X-ray bursts were detected in the time series of the *RXTE* data sets, and a sudden X-ray outburst took place (Gavriil et al. 2008; see also Kumar & Safi-Harb 2008; Kuiper & Hermsen 2009). The source then returned to the quiescent state in about 6 weeks. In this study we will adopt the values estimated by Gavriil et al. (2008) for the total energy released during the outburst, as well as the time-scale of the decay (see Table 2). We assume a distance of 6 kpc throughout the paper.

2.17 1E 161348–5055

The source 1E 161348–5055 near the geometrical centre of the SNR RCW 103 defied any interpretation for more than two decades because of its puzzling phenomenology (in particular, a periodicity at 6.67 h and the lack of an optical/infrared counterpart; De Luca et al. 2006, 2008). On 2016 June 22, the *Swift* BAT detected a magnetar-like burst from 1E 161348–5055, also coincident with a large long-term X-ray outburst (D’Ai et al. 2016). The long-term light curve of the source from 1999 to 2016 July was already extracted by Rea et al. (2016; see in particular their fig. 2) in a way completely consistent with the procedure reported in this work for the other magnetar outbursts, and shows that the source experienced another major outburst in 2000 February. In the following, we will thus refer to that publication when quoting our estimates for the energetics and decay time-scale for the first outburst. On the other hand, the *Swift* XRT monitoring campaign of this object is ongoing on a monthly cadence and we are currently tracking the decay of the second outburst to refine the time-scale and energetics of this episode. The outburst is showing a slower evolution with respect to that we predicted in Rea et al. (2016), and in the following we will consider our updated values for the energetics and time-scales (up to mid-July 2017; see Table 2). We assume a distance of 3.3 kpc throughout the paper.

3 DATA REDUCTION AND EXTRACTION

This section describes the standard procedures employed to extract the scientific products (source and background spectra) and create or assign the response and auxiliary files starting from the raw *Swift*, *XMM–Newton* and *Chandra* data files publicly available. In addition to these data sets, we also looked at other few observations carried out with the Medium-Energy Concentrator Spectrometer (MECS; Boella et al. 1997) on board *BeppoSAX*, the *ROSAT* Position Sensitive Proportional Counter (PSPC; Pfeffermann et al. 1987), and the Proportional Counter Array (PCA; Jahoda et al. 2006) instrument of the *RXTE*. In particular, we focused on the data concerning the quiescent stages (pre-outburst observations),

or the very early phases, of the outbursts. These data sets revealed to be crucial to estimate fluxes and luminosities for the magnetar XTE J1810–197 during quiescence or for other magnetars (i.e., SGR 1627–41 during its 1998 event and SGR 0418+5729) at the very early stages of the outburst decay, and were reduced and analysed as described by Esposito et al. (2008, 2010a) and Rea et al. (2009, 2012a).

3.1 *Swift* data

XRT (Burrows et al. 2005) on board the *Swift* satellite uses a front-illuminated charge-coupled device (CCD) detector sensitive to photons with energies between 0.2 and 10 keV, with an effective area of about 110 cm^2 at 1.5 keV. Two readout modes are now available: photon counting (PC) and windowed timing (WT). In the former, the entire CCD is read every ~ 2.5 s, whereas in the latter 10 rows are compressed in one, and only the central 200 (out of 600) columns are read out. One-dimensional imaging is preserved, achieving a time resolution of ~ 1.7 ms and thus providing a larger dynamic range of measurable source intensities (see Hill et al. 2004 for a detailed description of the XRT readout modes).

We processed the data with standard screening criteria (see Capalbi et al. 2005) and generated exposure maps with the task XRTPipeline (version 0.13.3) from the FTOOLS package (Blackburn 1995), using the spacecraft attitude file. We selected events with grades 0–12 and 0 for the PC and WT data³, respectively, and extracted the source and background spectra using XSELECT (v. 2.4). We accumulated the source counts from a circular region centred on the source position and with a radius of 20 pixels (one XRT pixel corresponds to about 2.36 arcsec). Noteworthy exceptions are represented by the magnetar Swift J1834.9–0846 and the source 1E 161348–5055, for which we opted for a circle of radius 6 and 10 pixels, respectively, to minimize the contribution from the surrounding diffuse emission (see Section 2.11). To estimate the background in the PC-mode data, we extracted the events within an annulus centred on the source position with inner and outer radius of 40 and 80 pixels, respectively (12 and 19 pixels for Swift J1834.9–0846, 10 and 20 pixels for 1E 161348–5055). For the observations targeting the 2009 outburst of 1E 1547–5408 we considered instead a circle as far as possible from the source, to reduce the contamination by the three expanding dust scattering X-ray rings (see Tiengo et al. 2010). For the WT-mode data we adopted a region far from the target and of the same size as that used for the source.

For all the observations we built exposure-corrected and background-subtracted light curves using XRTLCCORR and LCMATH (the latter accounting also for different areas of the source and background extraction regions). We binned them with different time resolutions, and removed possible bursts/flares episodes by applying intensity filters to the event lists. This procedure aims at minimizing flux overestimates, and avoiding possible spectral distortions induced by the bursting emission, which is typically harder than that of the underlying continuum.

In case an observation in PC mode suffered from photon pile-up (typically this occurs when the source net count rate exceeds

³ Because of issues in the modelling of the response matrix files, spectra of heavily absorbed sources ($N_{\text{H}} \gtrsim 10^{22} \text{ cm}^{-2}$) occasionally are known to exhibit a bump and/or turn-up at low energy (typically below 1 keV) in WT mode for events with grades ≥ 1 . See http://www.swift.ac.uk/analysis/xrt/digest_cal.php.

$\sim 0.6 \text{ counts s}^{-1}$), we determined the extent of the piled-up region as follows. First, we modelled the wings of the radial profile of the source point-spread function (at a distance > 15 arcsec from the centre) with a King function reproducing the PSF of the XRT (Moretti et al. 2005). We then extrapolated the model back to the core of the PSF, and compared it to the data points. The region where the observed PSF lies underneath the extrapolation of the King function was then excluded from our analysis⁴.

We created the observation-specific ancillary response files with XRTMKARF (v. 0.6.3), thereby correcting for the loss of counts due to hot columns and bad pixels, and accounting for different extraction regions, telescope vignetting and PSF corrections. We then assigned the appropriate redistribution matrix available in the HEASARC calibration data base, and excluded bad spectral channels (at energy < 0.3 keV). We co-added individual spectra and responses for contiguous observations with very few counts and that were carried out with the same observing mode, to improve the statistics quality and increase the signal-to-noise ratio⁵. For extensively monitored outbursts we also constructed the long-term 0.3–10 keV count rate light curves (using the online *Swift* XRT data products generator; see Evans et al. 2009 for details), to gauge the decay time-scales (see Appendix B).

3.2 *XMM-Newton* data

The *XMM-Newton* satellite carries three co-aligned X-ray telescopes, each with an European Photon Imaging Camera (EPIC) imaging spectrometer at the focus. Two of the EPIC spectrometers use Metal Oxide Semiconductor CCD arrays (MOS cameras; Turner et al. 2001) and one uses pn CCDs (pn camera; Strüder et al. 2001). They all cover the 0.1–15 keV energy range with an effective area of about 500 cm^2 for each MOS and 1400 cm^2 for the pn at 1.5 keV. In this work we shall consider only data acquired with the pn camera, which provides the spectra with the highest counting statistics owing to its larger effective area.

The pn camera can operate in different modes. In full frame mode (FF; 73.4-ms time resolution), all pixels of the 12 CCDs are read out simultaneously and the full FoV is covered. In large window mode (LW; 47.7-ms time resolution), only half of the area in all CCDs is read out and in small window mode (SW; 5.7-ms time resolution) just part of one single CCD is used to collect data. The pn can also operate in timing mode, where data from a predefined area on one CCD chip are collapsed into a one-dimensional row to be read every 30 μs .

We retrieved the raw observation data files from the *XMM-Newton* Science Archive, and processed them to produce calibrated, concatenated photon event lists using the EPPROC tool of the *XMM-Newton* Science Analysis System (SAS v. 15.0; Gabriel et al. 2004) and the most up to date calibration files available (XMM-CCF-REL-332). For each observation we built a light curve of single pixel events (PATTERN = 0) for the entire FoV, and discarded episodes (if any) of strong soft-proton flares of solar origin using intensity filters. We then estimated the amount of residual contamination in each event file by comparing the area-corrected count rates in the in- and out-of-FoV regions of the detector⁶, and

⁴ See <http://www.swift.ac.uk/analysis/xrt/xrtpileup.php>.

⁵ Ancillary response files were weighted by the net number of counts of the source in each observation.

⁶ We used the script provided by the *XMM-Newton* EPIC Background

verified that it was negligible or low in all cases (here ‘negligible’ and ‘low’ are defined following De Luca & Molendi 2004). We extracted the source photons from a circular region centred on the source position and with a typical radius of 20–30 arcsec, depending on the source brightness, the presence of closeby sources and the distance from the edge of the CCD. The background was extracted from a circle located on the same CCD, and the position and size of the region were determined so as to guarantee similar low-energy noise subtraction and avoid detector areas possibly contaminated by out-of-time events from the source or too near to the CCD edges (we used the EBKGREG tool, which typically yielded larger radii for the cases where the source was particularly faint, e.g. SGR 1627–41 or SGR 0418+5729 close to the quiescent level). The case of Swift J1834.9–0846 stands apart owing to the surrounding extended emission (see Section 2.11), and the photon counts were collected within similar regions as those adopted by Younes et al. (2016).

We built background-subtracted and exposure-corrected light curves with different time binnings using the EPICLCCORR task, which also corrects the time series for any relevant instrumental effect such as bad pixels, chip gaps, PSF variation, vignetting, quantum efficiency and dead time, and accounts for the different sizes of the source and background extraction regions. We then removed possible source flaring episodes by applying ad hoc intensity filters on the light curves.

We estimated the potential impact of pile-up by comparing the observed event pattern distribution as a function of energy with the theoretical prediction in the 0.3–10 keV energy interval, by means of the EPATPLOT task. For piled-up sources, we selected the most suitable annular extraction region for the source counts via an iterative procedure, by excising larger and larger portions of the inner core of the source PSF until a match was achieved between the observed and expected distributions at the 1σ confidence level (c.l.) for both single and double pixel events.

We employed the standard filtering procedure in the extraction of the scientific products, retaining only single and double pixel events optimally calibrated for spectral analysis ($\text{PATTERN} \leq 4$), and excluding border pixels and columns with higher offset for which the pattern type and the total energy are known with significantly lower precision ($\text{FLAG} = 0$). We calculated the area of source and background regions using the BACKSCALE tool, and generated the redistribution matrices and effective area files with RMFGEN and ARFGEN, respectively. We used the EPISPECCOMBINE task to co-add the spectra and average the response files of closeby observations carried out with the same instrumental setup (i.e. same observing mode and optical blocking filter in front of the pn CCD) and with a scarce number of counts, to obtain a reasonable number of spectral bins for a meaningful spectral analysis.

3.3 Chandra data

The *Chandra X-Ray Observatory* includes two focal plane instruments: the Advanced CCD Imaging Spectrometer (ACIS; Garmire et al. 2003) and the High Resolution Camera (HRC; Zombeck et al. 1995). The ACIS operates in the 0.2–10 keV energy range with an effective area of about 340 cm^2 at 1 keV. It consists of an imaging (ACIS-I) and a spectroscopic (ACIS-S) CCD arrays. The HRC covers the 0.1–10 keV interval with an effective area of about 225 cm^2

working group available at <http://www.cosmos.esa.int/web/xmm-newton/epic-scripts#flare>.

at 1 keV and comprises the HRC-I and the HRC-S detectors. The former optimized for wide-field imaging, and the latter designed for spectroscopy⁷.

The ACIS detectors enable two modes of data acquisition: the timed exposure (TE) mode, and the continuous clocking (CC) mode. In the former, each chip is exposed for a nominal time of 3.241 s (or a sub-multiple, if only a sub-array of a chip is being read-out). In the latter, data are transferred from the imaging array to the frame store array every 2.85 ms, at the expense of one dimension of spatial information.

We analysed the data following the standard analysis threads for a point-like source with the *Chandra* Interactive Analysis of Observations software (CIAO, v. 4.8; Fruscione et al. 2006) and the calibration files stored in the *Chandra* CALDB (v. 4.7.1). Only non-dispersed (zeroth-order) spectra were extracted for observations where a grating array was used. We used the CHANDRA_REPRO script to reprocess the data and generate new ‘level 2’ events files with the latest time-dependent gain, charge transfer inefficiency correction, and sub-pixel adjustments. For TE-mode data and on-axis targets, we collected the source photons from a circular region around the source position with a radius of 2 arcsec. An important outlier is SGR 1745–2900 amid the Galactic Centre, for which the counts were accumulated within a 1.5-arcsec radius circular region. A larger radius would have included too many counts from Sgr A* (see Coti Zelati et al. 2015a, 2017 for details). The *Chandra* PSF exhibits significant variations in size and shape across the focal plane. Therefore, for the few cases where the target of interest was located far from the position of the aim point, we proceeded as follows. First, we accurately measured the coordinates of the source centroid by applying the CIAO source detection algorithm WAVDETECT (Freeman et al. 2002) to the exposure-corrected image. We adopted the default ‘Ricker’ wavelet (‘Mexican Hat’ wavelet) functions with scales ranging from 1 to 16 pixels with a $\sqrt{2}$ step size and the default value for the source pixel threshold ($\text{SIGTHRESH} = 10^{-6}$). We then calculated the off-axis angle from the pointing direction, and used the CIAO tool PSFSIZE_SRCS to estimate the radius of the 90 per cent encircled counts fraction at 3 keV. In all cases the background was extracted from an annulus centred on the source location. For observations with the ACIS set in CC mode, source events were instead collected through a rectangular region of dimension 4 arcsec along the readout direction of the CCD. Background events were extracted within two similar boxes oriented along the image strip, symmetrically placed with respect to the target and sufficiently far from the position of the source, to minimize the contribution from the PSF wings.

We filtered the data for flares from particle-induced background (e.g., Markevitch et al. 2003) by running the DEFLARE routine on the lightcurves, and estimated the impact of photon pile-up in the TE-mode observations using the PILEUP_MAP tool. On the other hand, the fast readout of the ACIS in the CC-mode ensured in all cases that the corresponding spectra were not affected by pile-up. Because of the sharp *Chandra* PSF, discarding photons in the core of the PSF to correct for pile-up effects results in a significant loss of counts. Spectral distortions were then mitigated directly in the spectral modelling, as described in Section 4.

We created the source and background spectra, the associated redistribution matrices and ancillary response files using the

⁷ Observations performed with the HRC-I were not analysed because this camera provides only a limited energy resolution on the detected photons.

SPECEXTRACT script⁸. Spectra and auxiliary and response files for contiguous observations with low counting statistics were combined using the COMBINE–SPECTRA script.

4 SPECTRAL ANALYSIS

We generally grouped the background-subtracted spectra to have at least 20 counts in each spectral bin using GRPPHA, to allow for fitting using the χ^2 statistics. For the spectra with the largest number of counts (typically those extracted from *XMM–Newton* and *Chandra* observations, but in some cases also from *Swift* pointings at the earliest stages of the most powerful outbursts), we adopted a higher grouping minimum and the optimal binning prescription of Kaastra & Bleeker (2016)⁹. For the spectra with too few counts for the χ^2 -fitting, we opted to group the data to a lower degree (or even not to group them in the case of the *Swift* XRT spectra of SGR 1627–41 and Swift J1834.9–0846), and use the Cash statistics (*C*-statistics; Cash 1979).

We performed the spectral analysis separately for the *Swift*, *Chandra* and *XMM–Newton* data, owing to known cross-calibration uncertainties (e.g. Tsujimoto et al. 2011) and their remarkably different effective areas and energy dependence, which translate into different counting statistics and therefore best-fitting models in most cases (the larger the statistics available, the larger the number of spectral components required to properly fit the data).

For the spectral modelling we employed the XSPEC spectral fitting package (v. 12.9.1; Arnaud 1996), and applied the Levenberg–Marquardt minimization algorithm (Press et al. 1992). We restricted our analysis to the energy interval whereby the calibration of the spectral responses is best known, i.e. 0.3–10 keV for *Swift* XRT and *XMM–Newton* EPIC (with some exceptions for the XRT WT-mode data; see below), 0.3–8 keV for *Chandra*, 1.8–10 keV for *BeppoSAX* MECS, 0.1–2.4 keV for *ROSAT* PSPC and 3–10 keV for *RXTE* PCA. For the faintest outbursts (e.g. those of CXOUJ164710.2–455216 and the 2008 event from 1E 1547–5408) and heavily absorbed sources (e.g. SGR 1833–0832 and Swift J1834.9–0846), we further limited our study to photons with energy above 1–2 keV, owing to the few available counts at lower energy. On the other hand, the spectra of SGR 0418+5729 softened significantly as the source approached the quiescent phase. The few photons at energy $\gtrsim 3$ keV were overwhelmed by the background and hence discarded. In some cases, spectra acquired by *Swift* and with the XRT configured in WT mode exhibited some residual bumps due to calibration uncertainties below ~ 1 keV. Because these features would yield a misleading (systematically underestimated) value for the absorption column density, we decided to filter out the spectral channels at low energy (< 0.8 keV).

4.1 Spectral models

For the continuum emission we tested a set of different single and double-component empirical models: a blackbody (BBODYRAD; BB), a power law (PL), a blackbody plus a power law (BB+PL), the superposition of two blackbodies (2BB) and resonant cyclotron

⁸ Ancillary response files are automatically corrected to account for continuous degradation in the ACIS CCD quantum efficiency.

⁹ See <http://cms.unige.ch/isdc/ferrigno/developed-code>.

scattering models. In particular, we applied the NTZ model developed by Nobili et al. (2008a,b), which is based on three-dimensional Monte Carlo simulations. The topology of the magnetic field is assumed to be a globally twisted, force-free dipole in the model, and its parameters are the surface temperature (assumed to be the same over the whole surface), the bulk motion velocity of the charged particles in the magnetosphere (assumed constant through the magnetosphere), the twist angle and a normalization constant. This model has the same number of free parameters as the empirical two-component models mentioned above (2BB and BB+PL). In the cases of XTE J1810–197 and the 2002 outburst of 1E 2259+586, the higher statistics quality available from *XMM–Newton* observations allowed us to probe more complicated models, such as the sum of three thermal components (3BB). Because the internal calibration accuracy of the pn CCD for on-axis sources is estimated to be better than 2 per cent at the 1σ c.l. (Smith 2016¹⁰), we added an extra 2 per cent systematic error term to each spectral channel in these cases, as also recommended by the online threads. We then assessed the number of required spectral components by means of the Fisher test (e.g. Bevington 1969), setting a minimum threshold of 3σ (99.7 per cent) for the statistical significance of the improvement in the fit.

If pile-up was detected in a *Chandra* observation (typically at the early stages of the outburst), the multiplicative pile-up model of Davis (2001) was included, as implemented in XSPEC. Following the prescriptions reported in ‘The *Chandra* ABC Guide to Pile-up’¹¹, the only parameters allowed to vary were the grade-migration parameter and the fraction of events within the central, piled up, portion of the source PSF.

The photoelectric absorption by the interstellar medium along the line of sight was described through the Tuebingen–Boulder model (TBABS in XSPEC), and we adopted the photoionization cross-sections from Verner et al. (1996) and the chemical abundances from Wilms, Allen & McCray (2000). The choice of these abundances typically translates into values for the column density about 30 per cent larger than those estimated assuming the solar abundance tables from Anders & Grevesse (1989).

For SGR 1745–2900 the FGCDUST model was also included to correct for the effects of scattering of X-ray photons on interstellar dust grains located along the line of sight towards the source (likely in the Galactic disc and a few kpc away from the Galactic Centre according to Jin et al. 2017; see also Coti Zelati et al. 2017). For SGR 1833–0832 and Swift J1834.9–0846, i.e. the most absorbed sources of our sample besides SGR 1745–2900 (see Table 1), we tested the inclusion of the XSCAT model (Smith, Valencic & Corrales 2016) to account for the effect of dust scattering of spreading the photons along the line of sight around the source, an effect that is more relevant for the most heavily absorbed objects¹².

Although both the adoption of different chemical abundances and the correction for dust scattering opacity yield some differences in the values for the hydrogen column density and hence the unabsorbed fluxes, they provide only a secondary source of systematic error on the estimate of the luminosities compared to the uncertainties on the sources distances (see Section 5). Furthermore, we

¹⁰ See <http://xmm2.esac.esa.int/docs/documents/CAL-TN-0018.pdf>.

¹¹ See http://cxc.harvard.edu/ciao/download/doc/pileup_abc.pdf.

¹² We assumed different models for the dust composition and grain size distribution (see Mathis, Rumpl & Nordsieck 1977; Weingartner & Draine 2001; Zubko et al. 2004).

checked that they did not translate into significantly different decay patterns and estimates for the total energy released during the outburst.

4.2 Spectral fits

For each outburst, we started by fitting together the absorbed BB+PL and 2BB models to the spectra acquired by *Swift* XRT¹³ (with the exception of XTEJ1810–197, the 2008 outburst of SGR 1627–41, SGR 0418+5729, SGR 1833–0832, Swift J1834.9–0846, the 2011 outburst of CXOU J164710.2–455216, SGR 1935+2154 and PSR J1119–6127, for which a single absorbed blackbody model provided an acceptable fit across the entire data set). All parameters of the BB and PL components were left free to vary from observation to observation. The absorption column density was left free to vary as well, but with the request to be the same at all stages of the outburst evolution. For extensively monitored sources (i.e., SGR 0501+4516, 1E 1547–5408 during the 2009 outburst, Swift J1822.3–1606, 1E 1048.1–5937, 1E 2259+586 during the 2012 outburst, SGR 1935+2154 and PSR J1119–6127), the joint modelling was performed on groups of 20 spectra, to reduce the time-scale of the convergence of the fit and of the computation of parameter uncertainties.

In most cases, spectra of observations carried out at late stages of the outburst were described adequately by an absorbed blackbody alone and the addition of a second component was not statistically required. However, we decided to retain the second component in the spectral fits, and freeze its pivotal parameter (the power law photon index in the BB+PL model or the temperature of the second, hotter, blackbody in the 2BB model) to the value inferred for the spectrum of the last pointing where the second component is significantly detected. Alternatively, this parameter was tied up between all these data sets. For both alternative strategies, the normalizations of the spectral components were left free to vary. We then derived stringent upper limits on the contribution of the additional spectral component, and verified that the fits to the single spectra yielded values for the parameters consistent with those inferred from the joint modelling.

The above-mentioned fitting procedure was subsequently repeated for the *XMM-Newton* and *Chandra* data sets. Table 1 reports the best-fitting models. Appendix C reports a series of figures (Fig. C1) showing a set of high-quality X-ray spectra and the best-fitting empirical models for several outbursts that were repeatedly monitored by the *XMM-Newton* or *Chandra* observatories.

For the cases where the C -statistics was employed, we evaluated the quality of the fit by Monte Carlo simulations. We used the GOODNESS command within XSPEC to simulate a total of 1000 spectra (based on a Gaussian distribution of parameters centred on the best-fitting model parameters and with Gaussian width set by the 1σ uncertainties on the parameters), and determined the percentage of simulations having a C -statistics value much lower or higher than that obtained from the best fit of the data.

¹³ For SGR 1745–2900, we considered instead *Chandra* data alone, because only the exquisitely sharp PSF of the ACIS instrument enables to single out the magnetar counterpart in the crowded region of the Galactic Centre. See Coti Zelati et al. (2015a, 2017) for details.

5 LIGHT CURVES

For each fitted spectrum, we calculated the absorbed flux for the total source emission, as well as the unabsorbed flux and the luminosity for the single spectral components and for the total source emission (all in the 0.3–10 keV energy range). Unabsorbed fluxes were calculated using the convolution model CFLUX, and converted to luminosities (as measured by an observer at infinity) assuming isotropic emission and the most reliable value for the distance of the source (see Section 2 and Table 5). All the uncertainties are quoted at the 1σ c.l. for a single parameter of interest ($\Delta\chi^2 = 1$; Lampton, Margon & Bowyer 1976) throughout this work, whereas upper limits are reported at the 3σ c.l. For each outburst, we checked that the unabsorbed fluxes inferred for observations carried out with different instruments approximately at the same epoch were consistent with each other within the cross-correlation uncertainties.

The determination of unabsorbed fluxes from models comprising absorbed power law components is known to overestimate the source flux by a large factor, owing to the divergence of the power law component at low energy. We hence considered the results obtained from the NTZ model (Nobili et al. 2008a,b) to estimate bolometric (0.01–100 keV) luminosities for the cases where a power law spectral component was required in the spectral fits. In all cases the bolometric fluxes were determined after having defined dummy response matrices with the DUMMYRSP command in XSPEC. An uncertainty of 15 per cent was assigned to each flux. We note that, in some cases, an additional spectral component was observed in the hard X-rays at the outburst peak, which then became undetectable within the following few weeks. However, the paucity of hard X-ray monitorings of magnetar outbursts prevents a proper study of the appearance, disappearance, and total energetics of this component over the whole class. If we consider all the hard X-ray observations of magnetar outbursts performed so far by *INTEGRAL*, *Suzaku* and *NuSTAR* (for SGR 0501+4516, SGR 1806–20, 1E 1547–5408, SGR 1745–2900, SGR 1935+2154, PSR J1119–6127, 1E 161348–5055; see Esposito et al. 2007; Rea et al. 2009; Enoto et al. 2010a,b; Kuiper et al. 2012; Kaspi et al. 2014; Archibald et al. 2016a; Rea et al. 2016; Younes et al. 2017; see Enoto et al. 2017 for a review of all these cases), our values for the bolometric fluxes neglecting this component are underestimated (only close to the outburst peak though) by a factor $\lesssim 20$ per cent in all cases but SGR 1806–20 and 1E 1547–5408. For these two magnetars we might be underestimating our bolometric flux at the outburst peak by a factor of $\sim 2 - 3$, however the lack of a proper monitoring of the hard X-ray component precludes an accurate modelling of the time evolution of the hard X-ray emission.

All cooling curves are shown in a series of figures in Appendix D (see Figs D4–D20), and include the evolution of the absorbed fluxes, of the 0.3–10 keV luminosities (for the single spectral components and for the total emission) and of the bolometric luminosities.

Fig. 1 shows the temporal decays of the bolometric luminosities for all outbursts. We refer each curve to the epoch of the outburst onset, defined as the time of the first burst detection from the source (mostly with *Swift* BAT or *Fermi* GBM), or of the giant flare in the case of SGR 1806–20 (note however that the source flux already doubled during the first half of 2004 with respect to the quiescent level; Mereghetti et al. 2005). For XTEJ1810–197 and 1E 1048.1–5937, for which no bursts were detected prior to their outbursts (see Sections 2.3 and 2.12, respectively), we adopted the

epoch of the observation where an increase in the X-ray flux was first measured as the reference epoch.

5.1 Phenomenological modelling

We modelled the decays of the X-ray luminosities of the single spectral components and of the total bolometric luminosities using a constant (dubbed L_q and representing the quiescent level; see Table 4) plus one or more exponential functions (dubbed EXP, 2EXP, and 3EXP in the following) of the form

$$L(t) = L_q + \sum_{i=1}^j A_i \times \exp(-t/\tau_i), \quad (1)$$

with $j \leq 3$ (τ_i denotes the e -folding time). The number of required exponential functions was evaluated by means of the F -test, i.e., an additional exponential was included only if it yielded an improvement in the fit of at least 3σ . A superexponential function of the form

$$L(t) = L_q + B \times \exp[-(t/\tau)^\alpha] \quad (2)$$

was also tested as an alternative to the double-exponential model in several cases, leading however to an extrapolated luminosity at the very early stages of the outburst systematically overestimated compared to that obtained with the double-exponential function. We assume conservatively that the peak luminosity attains a value not so different from that measured in the earliest observation available, and favour the double-exponential model in the following.

L_q was fixed at the quiescent value or, in cases of non-detections, constrained to be lower than the upper limit (see Table 4 for our estimates of the quiescent bolometric luminosities). There are however two exceptions for the modelling of the bolometric light curves: in the case of the 2008 outburst of 1E 1547–5408 and of the 1998 outburst of SGR 1627–41, the sources did not reach the historical quiescent level while recovering from the outburst. In these cases the constant term was held fixed at the quiescent value reached after that particular outburst (which is larger than the historical minimum reported in Table 4).

Although other alternative phenomenological models such as broken power laws or those consisting in the combination of one or multiple linear and power law terms could satisfactorily reproduce the decays of several outbursts, we opted to fit exponential functions to all light curves, to allow a direct comparison of the decay time-scales (i.e., the τ parameter) among different outbursts. On the other hand, the estimate of the outburst energetics is not sensitive to the model used to fit the luminosity decay.

5.2 Outburst energetics

We estimated the total outburst impulsive energetics by integrating the best-fitting model for the bolometric light curves over the whole duration of the event, and extrapolating it to the quiescent value for the cases where the observational campaign was not extended enough to follow completely the return to the pre-outburst state:

$$E = \int_0^{t_q} L_{\text{bol}}(t) dt, \quad (3)$$

where t_q is the epoch of the recovery of the quiescent state expressed as time since the outburst onset. For the sources that are still recovering from their outbursts (i.e., 1E 1547–5408, SGR 1745–2900, 1E 1048.1–5937, PSR J1119–6127 and 1E 161348–5055), we assumed no changes in the decay pattern

down to quiescence for the estimate of the time-scales and energetics (in these cases the derived decay time-scale and the total outburst energetics should be considered as upper limits). Fig. 2 shows the best-fitting models (see also the right-hand panels of Figs D4–D20 for the individual cases), and Table 2 reports the corresponding parameters. The assumed 15 per cent error on each bolometric value is likely an underestimate (the largest uncertainty arising from the poorly constrained distance of the source in almost all cases). For some extensively monitored outbursts we verified that the choice of larger uncertainties on these values yielded no significant alteration of the decay pattern and of our estimates for the characteristic time-scales and the amount of energy released during the event.

6 PEAK AND QUIESCENT LUMINOSITIES

Fig. 3 shows the maximum luminosity increase as a function of the quiescent (steady) X-ray luminosity for all magnetars that so far have displayed substantial enhancements and/or variability in their X-ray emission. To have a more complete sample, we have also included SGR 1900+14, 4U 0142+61 and 1E 1841–045. In fact, although extensive X-ray observations in the *Swift*, *XMM–Newton* and *Chandra* era did not detect major X-ray outbursts from these targets, re-brightenings or subtle variations around their persistent activity have been nevertheless reported throughout the last 15 yr. SGR 1900+14 exhibited a giant flare in 1998 (Hurley et al. 1999), and re-brightened in the X-rays on two occasions, 2001 April and 2006 March (Göögüs et al. 2011b and references therein). Its flux decline was monitored by *Chandra* and *XMM–Newton* until 2008, and after both episodes the source reached the same minimum flux level, which we identify as the bona fide quiescent one (see Fig. B1 for the *Swift* XRT light curve). 4U 0142+61 showed repeated low-level variability on top of its persistent emission on at least two occasions, in 2011 July and 2015 February (Archibald et al. 2017b)¹⁴. 1E 1841–045 also showed sporadic bursting/flaring activity between 2010 May and 2011 July (a total of nine bursts were indeed recorded by *Swift* BAT and *Fermi* GBM), and some deviation from the source historical persistent X-ray flux has been noticed between 2008 and 2011 (Lin et al. 2011). The source has been subsequently monitored by *Swift* XRT about 145 times until the end of 2017 April. Finally, a recent analysis by Scholz et al. (2014) showed that the flux of magnetar 1RXS J170849.0–4009 remained constant within uncertainties between 2003 and 2013, in contradiction with what reported by Göögüs et al. (2007). In particular, the maximum variability for the X-ray flux is constrained to be lower than 10 per cent over this decade. We also verified that the source flux remained approximately steady between 2013 April and 2017 May by visually inspecting the long-term X-ray light curve generated using all the *Swift* XRT observations carried out during this period (which also covers the epoch of the detection of a magnetar-like burst, on 2017 February 17; see Archibald, Scholz & Kaspi 2017). In light of these characteristics, we decided not to include this source in our sample.

For each magnetar, spectra relative to the first observation following the outburst onset were used to measure accurately fluxes and luminosities at the very early phases of the outburst. For the sources showing low-level variability (see above), we extracted and

¹⁴ An additional magnetar-like burst in 2017 July was recently reported by Hamburg (2017).

fitted the spectrum relative to the observation where the source is found at the highest flux ever. Table 3 lists the inferred values. The quiescent 0.3–10 keV fluxes and luminosities for all magnetars monitored so far are reported in Table 4. Bolometric luminosities are also quoted. We also calculated the flux during pre-outburst observations (if available), and considered the lowest value historically to estimate the quiescent level. For the sources where only low-level variability has been reported, we focused on the observations with high counting statistics to derive the persistent flux.

In all cases, the spectra were fitted using thermal models (i.e., one or multiple blackbody components) or the NTZ model, to avoid possible overestimates in the values for the fluxes introduced when fitting a power law model to the data. For *ROSAT* data, we extrapolated the 0.3–2.4 keV fluxes using the DUMMYRSP tool. For the cases where the source is not detected, we applied the SRCFLUX task of CIAO (for the *Chandra* observations of Swift J1834.9–0846 and SGR 1745–2900) and the EUPPER tool of SAS (for the *XMM-Newton* observation of SGR 1833–0832) to derive 3σ upper limits on the net count rates at the source position (the background was estimated locally). We found values of 2×10^{-4} , 1.1×10^{-3} and 7×10^{-4} counts s $^{-1}$ for Swift J1834.9–0846, SGR 1745–2900 and SGR 1833–0832, respectively. We then assumed a blackbody spectral model with $kT = 0.3$ keV (similarly to what observed in other quiescent magnetars; see e.g. table 3 by Olausen & Kaspi 2014), and the same column density derived from the joint spectral fits of the outburst decay, to infer upper limits on the fluxes with the Portable, Interactive Multi-Mission Simulator (PIMMS, v. 4.8; Mukai 1993).

7 SEARCH FOR CORRELATIONS

Our systematic analysis allows us to search for correlations between different parameters for all sources of our sample and their outbursts, in particular between parameters measured in this work (e.g., quiescent luminosity, maximum luminosity, maximum luminosity increase, outburst energetics and time-scale) and the timing-inferred parameters (e.g., surface dipolar magnetic field, rotational energy loss rate, characteristic age).

Table 5 reports the most up-to-date values for the spin period and the spin-down rate for our sample of magnetars, and for the other sources we included in our correlation study (see below). We list the strength of the surface dipolar component of the magnetic field at the pole, the spin-down luminosity and characteristic age (all estimated assuming simple magnetic dipole braking in vacuo, the initial spin period to be much smaller than the current value, and no variation of the magnetic field in time). Several magnetars displayed a high level of timing noise in their rotational evolution across the outburst decay, and significant deviations from simple spin-down were often detected. For these cases we assumed a long-term average value for the spin-down rate to infer the characteristic parameters, following Olausen & Kaspi (2014).

Table 6 reports the significance for the (anti)correlations among several different combinations of parameters. The significance was evaluated from the two-sided null-hypothesis probability (p -value) obtained from the Spearman and Kendall τ rank correlation tests. We did not include upper limit measurements in our computations, but verified that the reported upper limits were consistent with the observed trend for all cases where a significant ($> 2\sigma$) correlation or anticorrelation was observed. The table also reports on the shape of the (anti)correlation. The power law index was estimated for each case via a power law regression test based

on the least squares fitting method (only for the cases where the significance for the correlation was above 2σ). The table also indicates whether the observed/unobserved correlation/anticorrelation fits either the internal crustal cooling model (Perna & Pons 2011; Pons & Perna 2011; Pons & Rea 2012) or the untwisting bundle model (Beloborodov 2009) proposed to account for the evolution of magnetar outbursts (see also Section 8).

All plots are shown in Figs 3–8. In all figures, the black triangles denote all magnetars of our sample; black squares represent the high-field rotation-powered pulsars that underwent an outburst (i.e., PSR J1119–6127 and PSR J1846–0258) and the grey cross denotes 1E 161348–5055. The year of outburst onset is indicated in parentheses for sources that underwent more than one luminosity enhancement. To have a more complete sample, we included also the other few magnetars (black stars), the central compact objects (grey crosses), the rotation-powered pulsars clearly showing a thermal component in their spectra (red diamonds) and the X-ray dim isolated neutron stars (orange crosses) already reported by Viganò et al. (2013; see in particular their table 1 for a list and their section 2 for the criteria adopted to select the sample). PSR J1119–6127 and the magnetars XTE J1810–197, 1E 1547–5408 and SGR 1745–2900, for which radio pulsed emission was detected (Camilo et al. 2006, 2007; Eatough et al. 2013), are marked by black circles. Upper and lower limits are indicated by black arrowheads.

8 DISCUSSION

We carried out the first systematic study of all sources experiencing magnetar-like outbursts up to the end of 2016, and for which extensive X-ray monitoring campaigns of their outbursts are available. We re-analysed in a coherent way about 1100 X-ray observations, adopting the same assumptions and spectral models throughout the whole sample. This work allows us to study possible correlations and anticorrelations between several different combinations of parameters, and put the results in the context of the models proposed to explain the triggering mechanism and evolution of magnetar outbursts.

8.1 On the relation between the outburst luminosity increase and the quiescent luminosity

A few years ago, Pons & Rea (2012) showed how magnetars with low quiescent luminosities ($L_q \sim 10^{31} - 10^{33}$ erg s $^{-1}$) experience large luminosity increases during an outburst, whereas the brightest sources in quiescence ($L_q \sim 10^{34} - 10^{35}$ erg s $^{-1}$) undergo only subtle enhancements in luminosity. This discovery clarified that the distinction between ‘transient’ and ‘persistent’ sources within the magnetar population is deceptive, and only dependent on the initial quiescent luminosity of each source.

The anticorrelation between magnetars quiescent luminosities and their luminosity increases is observed at a significance of 5.7σ (according to the Spearman test; see Table 3 and Fig. 3), and suggests the existence of a limiting luminosity of $\sim 10^{36}$ erg s $^{-1}$ for magnetar outbursts (regardless of the quiescent level of the source). This result was interpreted in the framework of the internal crustal heating model as the observational manifestation of the self-regulating effect resulting from the strong temperature-dependence of the neutrino emissivity (Pons & Rea 2012): the surface photon luminosity for injected energies larger than $\sim 10^{43}$ erg reaches a limiting value of $\sim 10^{36}$ erg s $^{-1}$, because the crust is so hot that

most of the energy is released in the form of neutrinos before reaching the star surface. The observed anticorrelation is expected also in the untwisting magnetospheric bundle model, where the maximum theoretically predicted luminosity could be somewhat higher, a few 10^{36} erg s $^{-1}$ for the generous case of a twist with $\psi \sim 1$ rad extended to a large part of the magnetospheric volume. The generally lower values observed for the peak luminosity are interpreted, in this model, as a consequence of the limited size of the current bundle and the twist (Beloborodov 2009).

We used our updated sample (see Fig. 3) to gauge the general trend of this anticorrelation via a power law regression test:

$$\Delta L_X \equiv \frac{L_{X,peak}}{L_{X,q}} \propto L_{X,q}^{-0.7}. \quad (4)$$

We observed a similar trend when considering fluxes, suggesting a weak dependence on the sources distance.

We note that, although there is no observational bias in detecting large luminosity increases in sources with a high quiescent luminosity (see the empty regions on the top-right corners of Fig. 3), the lack of detections of weak outbursts in magnetars with a low quiescent level (see the empty regions on the bottom-left corners of Fig. 3) might follow from the lack of sufficient sensibility of the current all sky X-ray monitors in detecting relatively subtle outbursts in low-luminosity sources.

We also point out that, throughout this study, the epoch of the outburst onset was defined as the time of the first burst detection from the source (mostly with *Swift* BAT or *Fermi* GBM), or of the giant flare in the case of SGR 1806–20. This is a somewhat arbitrary choice, because the increase of the persistent flux during the time interval preceding the detection of magnetars bursting/flaring activity is usually missed by X-ray instruments. In some cases (e.g., CXOU J164710.2–455216 and SGR 1745–2900; see Muno et al. 2007 and Kennea et al. 2013b, respectively), the time-scale for the flux rise was constrained to be shorter than a couple of days, but this might not be necessarily the case for all magnetars. However, given the large sample, and the clear trend observed over several orders of magnitude, we do not expect to measure significantly different values for the outburst peak luminosity.

Different estimates on the time-scale of the luminosity increase were proposed in the past years. The internal crustal cooling models by Pons & Rea (2012) show that the internal heat wave takes some time to propagate from the location in the crust where the energy is injected up to the surface layers. Therefore, the luminosity increase is not instantaneous but relatively fast, and might range from a few hours up to a few days depending on the depth of the region where heat is released. On the other hand, simplified one-dimensional models show that the time-scale of magnetospheric twisting by a large thermoplastic wave (corresponding to the rise time of the outburst) can span from days to weeks (Li et al. 2016). Within the large uncertainties, both models are compatible with a typical rise time of a few days.

8.2 On the quiescent luminosity versus the spin-down luminosity and the dipolar magnetic field

The top panel of Fig. 4 reports the quiescent thermal bolometric luminosity ($L_{bol,q}$) of magnetars and of the other classes of isolated X-ray pulsars as a function of their spin-down luminosity (\dot{E}_{rot}). The dashed line represents $L_{bol,q} = \dot{E}_{\text{rot}}$. The emission of all sources lying above the dashed line must be ultimately powered by magnetic energy. On the other hand, the emission of all sources located below the dashed line might be entirely rotation-powered, or

switch between magnetar-like and rotation-powered emission. An interesting case is represented by the magnetar XTE J1810–197, whose steady, quiescent, luminosity, $L_{bol,q} \sim 4 \times 10^{34}$ erg s $^{-1}$ attained in the past ~ 5 yr (see Fig. D3) is a factor of ~ 60 larger than its spin-down luminosity $\dot{E}_{\text{rot}} \sim 6.7 \times 10^{32}$ erg s $^{-1}$, accurately estimated from timing analysis of X-ray data taken over the last 12 yr (see Table 5). This result contradicts the prediction put forward by Rea et al. (2012b), according to which a magnetar with $L_{X,q} \gtrsim \dot{E}_{\text{rot}}$ is expected to be radio quiet, regardless of its possible X-ray outburst activity.

The bottom panel of Fig. 4 shows the quiescent thermal bolometric luminosity as a function of the surface dipolar magnetic field. We observe a significant correlation (3.2σ according to the Spearman test) when including all sources belonging to the different classes considered in this study (the correlation is 3.9σ after excluding the central compact objects). This correlation is naturally explained in terms of magnetic field decay and Joule heating (Pons, Miralles & Geppert 2009; Viganò et al. 2013). The central compact objects clearly depart from the general trend. The peculiar behaviour of these objects might be explained in the framework of the ‘hidden magnetic field’ scenario: hypercritical accretion on to the neutron star surface during the initial stages of the star life can bury a magnetic field of a few 10^{13} G into the inner crust, yielding a strength for the external magnetic field that is significantly lower than the internal ‘hidden’ magnetic field. The large luminosity observed for these objects is most probably due to the toroidal and higher order multipolar components of the magnetic field trapped inside the crust (Geppert, Page & Zannias 1999; Ho 2011; Shabaltas & Lai 2012; Viganò & Pons 2012; Torres-Forné et al. 2016). The magnetic field will eventually re-emerge, after a few thousands of years, settling on a value comparable to that at birth. If this picture is correct, we would expect a ‘shift’ of the central compact objects towards the right in the quiescent luminosity versus dipolar magnetic field diagram, as the CCOs get older. Some of the rotation-powered pulsars also depart slightly from the observed trend (e.g., PSR J0538+2817, PSR B1055–52 and PSR J0633+1746). This might be possibly due to an additional contribution to the surface heating from slamming particles on to the stellar surface, as typically observed for pulsars with a high rotational energy loss rate.

We investigated the shape of the correlation via a power law regression test, and found

$$L_{bol,q} \propto B_{p,dip}^2 \quad (5)$$

(see Table 6). This is in agreement with the dependence reported by Pons et al. (2007) using a reduced sample of sources.

8.3 On the dipolar magnetic field versus the outburst properties

We also investigated possible correlations between the strength of the surface dipolar magnetic field and all the outburst parameters derived in this work. There is no significant correlation between the magnetic field and either the maximum luminosity or the decay time-scale. Furthermore, in a few cases the same source was observed to undergo two different outbursts with distinct properties (see Fig. 5).

The correlation between the magnetic field and the outburst energetics is more evident (3.4σ according to the Spearman test; see Fig. 6), and supports the idea that the energy reservoir of the outbursts is mainly provided by the dissipation of the magnetic field. The two variables are linearly related (i.e., $E \propto B_{p,dip}$).

We observe a sort of limiting energy as a function of age. Young magnetars tend to experience more energetic outbursts than older magnetars, a characteristic that can be explained simply in terms of field decay. The expected energetics distribution was estimated by Perna & Pons (2011), who did not find a significant dependence of the energy of the events with age, but the fact that magnetic field decay limits the energy budget available for old magnetars, compared to young sources. They also estimated the recurrence times between consecutive outbursts, and found as a general trend that the older the object, the longer the average recurrence time.

8.4 On the outburst energy versus other properties

The outburst energy correlates with the peak luminosity reached during the outburst (at a significance of 4.0σ according to the Spearman test), but not with the quiescent X-ray luminosity ($<2\sigma$; see Fig. 6). These results suggest that a larger luminosity at the peak of the outburst results in a larger energy released during the entire outburst event, regardless of the quiescent level of the source, and reflect similar decay patterns for magnetar outbursts. This is expected in both internal crustal cooling and untwisting bundle scenarios, since it only reflects the normalization of the decay curve.

The energetics correlates significantly with the decay time-scale (at a significance of 3.9σ according to the Spearman test): the longer the outburst, the more energetic (Fig. 7). This suggests again that the decay pattern is similar from outburst to outburst. For example, we never observe a magnetar undergoing a rather weak outburst and then returning to quiescence over an extremely long time interval, or a magnetar showing an extremely powerful outburst and then rapidly decaying back to quiescence.

9 THE MAGNETAR OUTBURST ONLINE CATALOGUE

All the key parameters derived for the magnetar outbursts presented in this study, as well as the reduced spectral files, are available at the MOOC (<http://magnetars.ice.csic.es>). We have also included all important parameters for the other thermally emitting isolated X-ray pulsars (see Table 5; see also Viganò et al. 2013), to allow a direct comparison between the different classes of isolated neutron stars.

The webpage consists of three distinct sections: Sources, Analysis and Download. In the Sources section, the user can plot any combination of the parameters for all thermally emitting isolated X-ray pulsars. In the Analysis section, the user can plot the light curves for all magnetar outbursts, as well as any combination of the parameters characterizing these events.

In both the Sources and Analysis sections, a detailed description of all parameters is provided, and the user can download all values of the plotted parameters in the form of a csv table. Furthermore, restricted ranges of values can be selected and plotted using the ‘Filter’ task. The user can also create mathematical functions linking different parameters via the ‘Create Function Field’ tool, and download the resulting plot as an image or an ascii file.

Finally, in the Download section, the user can download the fits files relative to all the observations of magnetar outbursts analysed in this study, i.e. the source and background average spectra, the redistribution matrix files and the auxiliary response files. Each file is named according to the following general scheme: ‘source name_name of the satellite_type of file_obsID.fits’, where ‘type of file’ is either src_spectrum, bg_spectrum, rmf or arf. The user

can perform a spectral analysis of the data by uploading these files in the XSPEC spectral fitting package.

The webpage will be updated periodically and expanded as new outbursts are observed.

ACKNOWLEDGEMENTS

We are indebted to Martin Folger and Santiago Serrano Elorduy from the Institute of Space Sciences (IEEC-CSIC) for designing the Magnetar Outburst Online Catalogue and implementing several plotting and analysis online tools. FCZ acknowledges Alice Borghese, Niccolò Bucciantini and Jason Hessels for useful suggestions that helped improving a preliminary version of the manuscript, Alexander Kaminker and Stefano Carignano for useful discussions, and Chichuan Jin for providing the *Chandra* ACIS-S version of the dust scattering model for Galactic Centre X-ray sources. We thank the referee for comments. The scientific results reported in this study are based on observations obtained with the *Chandra X-ray Observatory*, *XMM-Newton*, *Swift* and *RXTE*. *XMM-Newton* is an ESA science mission with instruments and contributions directly funded by ESA Member States and the National Aeronautics and Space Administration (NASA). *Swift* is a NASA/UK/ASI mission. *RXTE* is a NASA mission. This research has made extensive use of software provided by the *Chandra X-ray Center* [operated for and on behalf of NASA by the Smithsonian Astrophysical Observatory (SAO) under contract NAS8-03060] in the application package CIAO. The *XMM-Newton* SAS is developed and maintained by the Science Operations Centre at the European Space Astronomy Centre. We made use of data supplied by the UK *Swift* Science Data Centre at the University of Leicester and of the XRT Data Analysis Software (XRTDAS) developed under the responsibility of the ASI Science Data Center (ASDC), Italy. We also used softwares and tools provided by the High Energy Astrophysics Science Archive Research Center (HEASARC) Online Service, which is a service of the Astrophysics Science Division at NASA/GSFC and the High Energy Astrophysics Division of SAO. We made use of the McGill Online Magnetar Catalog (www.physics.mcgill.ca/~pulsar/magnetar/main.html) and NASA’s Astrophysics Data System Bibliographic Services. FCZ, NR and PE acknowledge funding in the framework of the Netherlands Organization for Scientific Research (NWO) Vidi award number 639.042.321 (PI: N. Rea) and the European COST Action MP1304 (NewCOMPSTAR). FCZ and NR are also supported by grants AYA2015-71042-P and SGR2014-1073. JAP acknowledges support by grants AYA2015-66899-C2-2-P and PROMETEOII-2014-069.

REFERENCES

- Alford J. A. J., Halpern J. P., 2016, ApJ, 818, 122
- An H., Kaspi V. M., Tomsick J. A., Cumming A., Bodaghee A., Gotthelf E. V., Rahoui F., 2012, ApJ, 757, 68
- An H., Kaspi V. M., Archibald R. F., Cumming A., 2013, ApJ, 763, 82
- Anders E., Grevesse N., 1989, GeCoA, 53, 197
- Archibald R. F. et al., 2013, Nature, 497, 591
- Archibald R. F., Kaspi V. M., Ng C.-Y., Scholz P., Beardmore A. P., Gehrels N., Kennea J. A., 2015, ApJ, 800, 33
- Archibald R. F., Kaspi V. M., Tendulkar S. P., Scholz P., 2016a, ApJ 829, L21
- Archibald R. F., Tendulkar S. P., Scholz P., Kaspi V. M., 2016b, Astron. Telegram, 9316, 1

- Archibald R. F., Scholz P., Kaspi V. M., 2017, Astron. Telegram, 10107, 1
- Archibald R. F. et al., 2017 ApJL, 849, 20
- Archibald R. F., Kaspi, V. M., Scholz P., Beardmore A. P., Gehrels N., Kennea J. A., 2017, ApJ, 834, 163
- Arnaud K. A., 1996, in Jacoby G. H., Barnes J., eds, ASP Conf. Ser. Vol. 101, Astronomical Data Analysis Software and Systems V. Astron. Soc. Pac., San Francisco, p. 17
- Barthelmy S. D. et al., 2005, Space Science Reviews, 120, 143
- Barthelmy S. D. et al., 2008, Astron. Telegram, 1676, 1
- Barthelmy S. D., Kennea J. A., Krimm H. A., Mangano V., Markwardt C. B., Marshall F. E., Maselli A., 2013, GRB Coordinates Network, 14443
- Barthelmy S. D., D'Avanzo P., Kennea J. A., Melandri A., Palmer D. M., 2016, GRB Coordinates Network, 19447
- Baumgartner W. H. et al., 2011, GRB Coordinates Network, 12359
- Beloborodov A. M., Thompson C., 2007, ApJ, 657, 967
- Beloborodov A. M., 2009, ApJ, 703, 1044
- Beloborodov A. M., Levin Y., 2014, ApJL, 794, 24
- Beloborodov A. M., Li X., 2016, ApJ, 833, 261
- Bernardini F. et al., 2009, A&A, 498, 195
- Bernardini F., Perna R., Gotthelf E. V., Israel G. L., Rea N., Stella L., 2011a, MNRAS, 418, 638
- Bernardini F. et al., 2011b, A&A, 529, 19
- Bevington P. R., 1969, Data Reduction and Error Analysis for the Physical Science. McGraw-Hill, New York
- Blackburn J. K., 1995, in Shaw R. A., Payne H. E., Hayes J. J. E., eds, ASP Conf. Ser. Vol. 77: Astronomical Data Analysis Software and Systems IV. Soc. Pac., San Francisco, p. 367
- Boella G., et al. 1997, A&AS, 122, 327
- Bower G. C. et al., 2015, ApJ, 798, 120
- Burrows D. N. et al., 2005, Space Science Reviews, 120, 165
- Camero A. et al., 2014, MNRAS, 438, 329
- Camilo F., Kaspi V. M., Lyne A. G., Manchester R. N., Bell J. F., D'Amico N., McKay N. P. F., Crawford F., 2000, ApJ, 541, 367
- Camilo F., Ransom S. M., Halpern J. P., Reynolds J., Helfand D. J., Zimmerman N., Sarkissian J., 2006, Nature, 442, 892
- Camilo F., Ransom S. M., Halpern J. P., Reynolds J., 2007, ApJ, 666, 93
- Camilo F. et al., 2016, ApJ, 820, 110
- Capalbi M., Perri M., Sajja B., Tamburelli F., Angelini L., 2005, The Swift XRT Data Reduction Guide, Technical Report 1.2
- Cash W., 1979, ApJ, 228, 939
- Connaughton V., Briggs M., 2009, GRB Coordinates Network, 8835, 1
- Coti Zelati F. et al., 2015a, MNRAS, 449, 2685
- Coti Zelati F., Campana S., Israel G. L., Rea N., Mereghetti S., Esposito P., Tiengo A., 2015b, Astron. Telegram, 8449, 1
- Coti Zelati F. et al., 2017, MNRAS, 471, 1819
- Crawford F., Gaensler B. M., Kaspi V. M., Manchester R. N., Camilo F., Lyne A. G., Pivovaroff M. J., 2001, ApJ, 554, 152
- Cummings J. R., Burrows D., Campana S., Kennea J. A., Krimm H. A., Palmer D. M., Sakamoto T., Zane S., 2011, Astron. Telegram, 3488, 1
- D'Ai A. et al., 2016, MNRAS, 463, 2394
- D'Avanzo P., Burrows D. N., Gehrels N., Kennea J. A., Krimm H. A., Marshall F. E., Sakamoto T., Sbarufatti B., 2015, Astron. Telegram, 7123, 1
- Davis J. E., 2001, ApJ, 562, 575
- D'Elia V. et al., 2011, GRB Coordinates Network, 12253
- De Luca A., Molendi S., 2004, A&A, 419, 837
- De Luca A., Caraveo P. A., Mereghetti S., Tiengo A., Bignami G. F. 2006, Science 313, 814
- De Luca A., Mignani R. P., Zaggia S., Beccari G., Mereghetti S., Caraveo P. A., Bignami G. F., 2008, ApJ, 682, 1185
- Dib R., Kaspi V. M., Scholz P., Gavriil F. P., 2012, ApJ, 748, 3
- Dib R., Kaspi V. M., 2014, ApJ, 784, 37
- Duncan R. C., Thompson C., 1992, ApJ, 392, L9
- Eatough R. et al., 2013, Astron. Telegram, 5058, 1
- Enoto T. et al., 2010a, PASJ, 62, 475
- Enoto T. et al., 2010b, ApJ, 715, 665
- Enoto T. et al., 2017, ApJS, 231, 8
- Esposito P. et al., 2007, A&A, 476, 321
- Esposito P. et al., 2008, MNRAS, 390, 34
- Esposito P. et al., 2009a, ApJ, 690L, 105
- Esposito P. et al., 2009b, MNRAS, 399, 44
- Esposito P., Israel G. L., Stella L., Rea N., Tiengo A., 2010, Astron. Telegram, 2494, 1
- Esposito P. et al., 2010, MNRAS, 405, 1787
- Esposito P. et al., 2011, MNRAS, 416, 205
- Esposito P. et al., 2013, MNRAS, 429, 3123
- Evans P. A. et al., 2007, A&A, 469, 379
- Evans P. A. et al., 2009, MNRAS, 397, 1177
- Fahlman G. G., Gregory P. C., 1981, Nature, 293, 202
- Foley S., Kouveliotou C., Kaneko Y., Collazzi A., 2012, GCN Circ. 13280
- Freeman P. E., Kashyap V., Rosner R., Lamb D. Q., 2002, ApJS, 138, 185
- Fruscione A. et al., 2006, in Silva D. R., Doxsey R. E., eds, Proc. SPIE, Vol. 6270, Observatory Operations: Strategies, Processes, and Systems. SPIE, Bellingham, p. 62701V
- Gabriel C. et al., 2004, in F. Ochsenbein, M. G. Allen, D. Egret, eds, ASPC. Astronomical Society of the Pacific Conference Series, 314, 759
- Garmire G. P., Bautz M. W., Ford P. G., Nousek J. A., Ricker G. R., Jr, 2003, in Truemper J. E., Tananbaum H. D., eds, Proc. SPIE, Vol. 4851, X-Ray and Gamma-Ray Telescopes and Instruments for Astronomy. SPIE, Bellingham, p. 28
- Gavriil F. P., Gonzalez M. E., Gotthelf E. V., Kaspi V. M., Livingstone M. A., Woods P. M., 2008, Science, 319, 1802
- Gehrels N., 1986, ApJ, 303, 336
- Gelbord J. M. et al., 2010, GRB Coordinates Network, 10526
- Gelfand J. D., Gaensler B. M., 2007, ApJ, 667, 1111
- Geppert U., Page D., Zannias T., 1999, A&A, 345, 847
- Göögüs E., Woods P., Kouveliotou C., 2008, Astron. Telegram, 1677, 1
- Göögüs E., Woods P., Kouveliotou C., 2009, Astron. Telegram, 2121, 1
- Göögüs E. et al., 2010a, ApJ, 718, 331
- Göögüs E., Woods P. M., Kouveliotou C., Kaneko Y., Gaensler B. M., Chatterjee S., 2010b, ApJ, 722, 899
- Göögüs E., Kouveliotou C., Strohmayer T., 2011a, Astron. Telegram, 3491, 1
- Göögüs E., Güver T., Özel F., Eichler D., Kouveliotou C., 2011b, ApJ, 728, 160
- Göögüs E., Kouveliotou C., 2011, Astron. Telegram, 3542, 1
- Göögüs E. et al. 2016, ApJ, 829, 25
- Gotthelf E. V., Vasish G., Boylan-Kolchin M., Torii K., 2000, ApJ, 542, 37
- Gotthelf E. V., Halpern J. P., Buxton M., Bailyn C., 2004, ApJ, 605, 368
- Gotthelf E. V.; Halpern J. P., 2005, ApJ, 632, 1075
- Götz et al., 2007, A&A, 475, 317
- Granot J., Gill R., Younes G., Gelfand J., Harding A., Kouveliotou C., Baring M. G., 2017, MNRAS, 464, 4895
- Gronwall C., Holland S. T., Markwardt C. B., Palmer D. M., Stamatikos M., Vetere L., 2009, GRB Coordinates Network, 8833
- Guiriec S., Kouveliotou C., van der Horst A. J., 2011, GRB Coordinates Network, 12255
- Halpern J. P., Gotthelf E. V., 2005, ApJ, 618, 874
- Halpern J. P., Gotthelf E. V., Reynolds J., Ransom S. M., Camilo F., 2008, ApJ, 676, 1178
- Hamburg R., 2017, GRB Coordinates Network, 21342
- Hill J. E. et al., 2004, SPIE, 5165, 217
- Ho W. C. G., 2011, MNRAS, 414, 2567
- Hoversten E. A. et al., 2011, GRB Coordinates Network, 12316
- Hurley K. et al., 1999, Nature, 397, 41
- Hurley K. et al., 2005, Nature, 434, 1098
- Ibrahim A. I. et al., 2004, ApJ, 609, 21
- Israel G. L., Campana S., Dall'Osso S., Munoz M. P., Cummings J., Perna R., Stella L., 2007, ApJ, 664, 448
- Israel G. L. et al., 2010, MNRAS, 408, 1387
- Israel, G. L., Rea N., Coti Zelati F., Esposito P., Burgay M., Mereghetti S., Possenti A., Tiengo A., 2014, Astron. Telegram, 6370, 1
- Israel G. L. et al., 2016, MNRAS, 457, 3448
- Jahoda K., Markwardt C. B., Radeva Y., Rots A. H., Stark M. J., Swank J. H., Strohmayer T. E., Zhang W., 2006, ApJS, 163, 401
- Jin C., Ponti G., Haberl F., Smith R., 2017, MNRAS, 468, 2532
- Kaastra J. S., Bleeker J. A. M., 2016, A&A, 587, 151

- Kargaltsev O. et al., 2012, ApJ, 748, 26
- Kaspi V. M., Gavriil F. P., Woods P. M., Jensen J. B., Roberts M. S. E., Chakrabarty D., 2003, ApJ, 588, 93
- Kaspiä V. M. et al., 2014, ApJ, 786, 84
- Kaspi V. M., Beloborodov A. M., 2017, ARA&A, 55, 261
- Kennea J. A. et al., 2013a, Astron. Telegram, 5009, 1
- Kennea J. A. et al., 2013b, ApJ, 770, 24
- Kennea J. A., Lien A. Y., Marshall F. E., Palmer D. M., Roegiers T. G. R., Sbarufatti B., 2016, GRB Coordinates Network, 19735
- Kouveliotou C., 1998, GRB Coordinates Network, 107
- Kouveliotou C. et al., 1998, Nature, 393, 235
- Kouveliotou C. et al., 2003, ApJ, 596, 79
- Krimm H., Barthelmy S., Campana S., Cummings J., Israel G. L., Palmer D., Parsons A., 2006, Astron. Telegram, 894, 1
- Krimm H. et al., 2008, GRB Coordinates Network, 8311
- Kuiper L., Hermsen W., 2009, A&A, 501, 1031
- Kuiper L., Hermsen W., den Hartog P. R., Urama J. O., 2012, ApJ, 748, 133
- Kumar H. S., Safi-Harb S., 2008, ApJ, 678, 43
- Lamb R. C., Markert T. H., 1981, ApJ, 244, 94
- Lampton M., Margon B., Bowyer S., 1976, ApJ, 208, 177
- Laros J. G., Fenimore E. E., Fikani M. M., Klebesadel R. W., Barat C., 1986, Nature, 322, 152
- Laros J. G. et al., 1987, ApJ, 320, 111
- Li X., Beloborodov A. M., 2015, ApJ, 815, 25
- Li X., Levin Y., Beloborodov A. M., 2016, ApJ, 833, 189
- Lin L. et al., 2011, ApJ, 740, 16
- Livingstone M. A., Ng C.-Y., Kaspi V. M., Gavriil F. P., Gotthelf E. V., 2011a, ApJ, 730, 66
- Livingstone M. A., Scholz P., Kaspi V. M., Ng C.-Y., Gavriil F. P., 2011b, ApJ, 743, 38
- Markevitch M. et al., 2003, ApJ, 583, 70
- Mathis J. S., Rumpl W., Nordsieck K. H., 1977, ApJ, 217, 425
- Mazets E. P. et al., 1981, Ap&SS, 80, 3
- Mereghetti S. et al., 2005, ApJ, 628, 938
- Mereghetti S. et al., 2006, A&A, 450, 759
- Mereghetti S., Esposito P., Tiengo A., 2007, Ap&SS, 308, 13
- Mereghetti S. et al., 2009, ApJ, 696L, 74
- Mereghetti S., Götz D., Ferrigno C., Bozzo E., Borkowski J., 2015, GRB Coordinates Network, 18711, 1
- Moretti A. et al., 2005, in Siegmund O. H. W., ed., UV, X-Ray, and Gamma-Ray Space Instrumentation for Astronomy XIV Vol. 5898 of SPIE Conference Series. SPIE, Bellingham, pp 348–356
- Mukai K., 1993, Legacy, 3, 21
- Muno M. P. et al., 2006, ApJ, 636, 41
- Muno M. P., Gaensler B. M., Clark J. S., de Grijs R., Pooley D., Stevens I. R., Portegies Zwart S. F., 2007, MNRAS, 378, 44
- Murakami T., Tanaka Y., Kulkarni S. R., Ogasaka Y., Sonobe T., Ogawara Y., Aoki T., Yoshida A., 1994, Nature, 368, 127
- Neilsen J. et al., 2013, ApJ, 774, 42
- Ng C.-Y. et al., 2011, ApJ, 729, 131
- Nobili L., Turolla R., Zane S., 2008a, MNRAS, 386, 1527
- Nobili L., Turolla R., Zane S., 2008b, MNRAS, 389, 989
- Olausen S. A., Kaspi V. M., 2014, ApJS, 212, 6
- Paczyński B., 1992, Acta Astron., 42, 145
- Palmer D. M. et al., 2004, GRB Coordinates Network, 2925, 1
- Palmer D. M. et al., 2005, Nature, 434, 1107
- Palmer D. M. et al., 2008, Astron. Telegram, 1548, 1
- Parfrey K., Beloborodov A. M., Hui L., 2013, ApJ, 774, 92
- Perna R., Pons J. A., 2011, ApJ, 727, L51
- Pfeffermann E. et al., 1987, in Soft X-ray optics and technology. Edited by E.-E. Koch & G. Schmahl Vol. 733 of SPIE Conference Series. SPIE, Bellingham, pp 519–532
- Pintore F. et al., 2016, MNRAS, 458, 2088
- Pons J. A., Link B., Miralles J. A., Geppert U., 2007, Phys. Rev. Letters, 98, id. 071101
- Pons J. A., Miralles J. A., Geppert U., 2009, A&A, 496, 207
- Pons J. A., Perna R., 2011, ApJ, 741, 123
- Pons J. A., Rea N., 2012, ApJ, 750, L6
- Press W. H., Teukolsky S. A., Vetterling W. T., Flannery B. P., 1992, Numerical Recipes in FORTRAN: The Art of Scientific Computing (2nd ed.; Cambridge: Cambridge Univ. Press)
- Rea N. et al., 2004, A&A, 425, 5
- Rea N. et al., 2009, MNRAS, 396, 2419
- Rea N. et al., 2010, Science, 330, 944
- Rea N., Esposito P., 2011, in Torres D. F., Rea N., eds, Astrophysics and Space Science Proceedings, High-Energy Emission from Pulsars and Their Systems. Springer-Verlag, Berlin, p. 247
- Rea N. et al., 2012a, ApJ, 754, 27
- Rea N., Pons J. A., Torres D. F., Turolla R., 2012b, ApJL, 748, 12
- Rea N. et al., 2013a, ApJ, 770, 65
- Rea N. et al., 2013b, ApJL, 775, 34
- Rea N., Borghese A., Esposito P., Coti Zelati F., Bachetti M., Israel G. L., De Luca A., 2016, ApJL, 828, 13
- Rodríguez Castillo G. A., Israel G. L., Esposito P., Pons J. A., Rea N., Turolla R., Viganò D., Zane S., 2014, MNRAS, 441, 1305
- Rodríguez Castillo G. A. et al., 2016, MNRAS, 456, 4145
- Scholz P., Kaspi V. M., 2011, ApJ, 739, 94
- Scholz P., Ng C.-Y., Livingstone M. A., Kaspi V. M., Cumming A., Archibald R. F., 2012, ApJ, 761, 66
- Scholz P., Kaspi V. M., Cumming A., 2014, ApJ, 786, 62
- Scholz P., Archibald R. F., Kaspi V. M., Ng C.-Y., Beardmore A. P., Gehrels N., Kennea J. A., 2014, ApJ, 783, 99
- Seward F. D., Charles P. A., Smale A. P., 1986, ApJ, 305, 814
- Shabaltas N., Lai D., 2012, ApJ, 748, 148
- Smith, 2016, (available at <http://xmm2.esac.esa.int/docs/documents/CAL-TN-0018.pdf>)
- Smith R. K., Valencic L. A., Corrales L., 2016, ApJ, 818, 143
- Sonobe T., Murakami T., Kulkarni S. R., Aoki T., Yoshida A., 1994, ApJ, 436, 23
- Spitkovsky A., 2006, ApJL, 648, L51
- Stamatikos M., Malesani D., Page K. L., Sakamoto T., 2014, GRB Coordinates Network, 16520
- Strüder L. et al., 2001, A&A, 365, 18
- Thompson C., Duncan R. C., 1993, ApJ, 408, 194
- Thompson C., Duncan R. C., 1995, MNRAS, 275, 255
- Thompson C., Duncan R. C., 1996, ApJ, 473, 322
- Thompson C., Duncan R. C., 2001, ApJ, 561, 980
- Thompson C., Lyutikov M., Kulkarni S. R., 2002, ApJ, 574, 332
- Tiengo A., Esposito P., Mereghetti S., Rea N., Stella L., Israel G. L., Turolla R., Zane S., 2005, A&A, 440, 63
- Tiengo A., Esposito P., Mereghetti S., 2008, ApJL, 680, 133
- Tiengo A. et al., 2010, ApJ, 710, 227
- Torres D. F., 2017, ApJ, 835, 54
- Torres-Forné A., Cerdá-Durán P., Pons J. A., Font J. A., 2016, MNRAS, 456, 3813
- Tsujimoto M. et al., 2011, A&A, 525, 25
- Turner M. J. L. et al., 2001, A&A, 365L, 27
- Turolla R., Zane S., Watts A., 2015, Reports on Progress in Physics, 78, 116901
- van der Horst A. J. et al., 2009, Astron. Telegram, 2077, 1
- van der Horst A. J. et al., 2010, ApJ, 711, 1
- Verner D. A., Ferland G. J., Korista K. T., Yakovlev D. G., 1996, ApJ, 465, 487
- Viganò D., Pons J. A., 2012, MNRAS, 425, 2487
- Viganò D., Rea N., Pons J. A., Perna R., Aguilera D. N., Miralles J. A., 2013, MNRAS, 434, 123
- Weingartner J. C., Draine B. T., 2001, ApJ, 548, 296
- Wilms J., Allen A., McCray R., 2000, ApJ, 542, 914
- Woods P. M. et al., 1999, ApJ, 519, 139
- Woods P. M. et al., 2004, ApJ, 605, 378
- Woods P. M., Kaspi V. M., Gavriil F. P., Airhart C., 2011, ApJ, 726, 37
- Younes G., Kouveliotou C., Kaspi V. M., 2015, ApJ, 809, 165
- Younes G. et al., 2016, ApJ, 824, 138
- Younes G., Kouveliotou C., Roberts O., 2016, GCN Circ. 19736
- Younes G. et al., 2017, ApJ, 847, 85

- Zhu W., Kaspi V. M., Dib R., Woods P. M., Gavriil F. P., Archibald A. M., 2008, ApJ, 686, 520
Zombeck M. V., Chappell J. H., Kenter A. T., Moore R. W., Murray S. S., Fraser G. W., Serio S., 1995, SPIE, 2518, 96
Zubko V., Dwek E., Arendt R. G., 2004, ApJS, 152, 211

Table 1. Spectral fitting results of magnetar outbursts. The year of the outburst onset is indicated in parentheses. NTZ denotes the resonant cyclotron scattering code by Nobili et al. (2008a,b), and was applied only in the cases where a power law component was needed when fitting ‘empirical’ models to the data. To account for interstellar absorption, we adopted the TBABS model, cross-sections from Verner et al. (1996) and abundances from Wilms et al. (2000). The hydrogen column density was tied up among all the observations targeting a specific source and the associated uncertainty is quoted at the 1σ c.l.

Source	Observatory (# obs)	Best-fitting model	N_{H} (emp) (10^{22} cm^{-2})	N_{H} (NTZ) (10^{22} cm^{-2})	Reference
SGR 1627–41 (1998)	<i>BeppoSAX</i> (4)	BB	6 ± 1	–	Table A1
	<i>XMM–Newton</i> (2)	BB	6^{+2}_{-1}	–	
	<i>Chandra</i> (4)	BB	10^{+2}_{-1}	–	
1E 2259+586 (2002)	<i>XMM–Newton</i> (8)	3BB	0.816 ± 0.007	–	Table A2
XTE J1810–197 (2003)	<i>XMM–Newton</i> (22)	3BB (1–11) 2BB (11–22)	1.22 ± 0.02	–	Table A3
SGR 1806–20 (2004)	<i>XMM–Newton</i> (10)	2BB	8.5 ± 0.1	–	Table A4
CXOU J164710.2–455216 (2006)	<i>Swift</i> (18)	BB+PL	3.06 ± 0.08	$2.43^{+0.04}_{-0.03}$	Table A5
	<i>XMM–Newton</i> (5) ^a	BB+PL	3.01 (fixed)	2.39 (fixed)	
	<i>Chandra</i> (5)	BB+PL	3.01 ± 0.04	$2.39^{+0.02}_{-0.01}$	
SGR 1627–41 (2008)	<i>Swift</i> (21)	BB	9 ± 2	–	Table A6
	<i>XMM–Newton</i> (2)	2BB	10^{+3}_{-2}	–	
	<i>Chandra</i> (4)	BB	10 ± 2	–	
SGR 0501+4516 (2008)	<i>Swift</i> (62) ^b	BB+PL (1–20)	1.319 (fixed)	$0.708^{+0.007}_{-0.006}$	Table A7
		BB+PL (21–40)	1.319 (fixed)	0.71 ± 0.03	
	<i>XMM–Newton</i> (6)	BB+PL (41–62)	1.319 (fixed)	0.708 (fixed)	
		BB+PL	1.319 ± 0.009	0.705 ± 0.004	
1E 1547–5408 (2008)	<i>Swift</i> (15)	BB+PL	4.9 ± 0.1	$4.65^{+0.05}_{-0.07}$	Table A8
	<i>Chandra</i> (5)	BB+PL	5.1 ± 0.2	4.83 ± 0.06	
1E 1547–5408 (2009)	<i>Swift</i> (97)	BB+PL (1–20)	$4.91^{+0.03}_{-0.13}$	4.59 ± 0.09	Table A9
		BB+PL (21–40)	4.91 (fixed)	4.59 (fixed)	
		BB+PL (41–60)	4.91 (fixed)	4.59 (fixed)	
		BB+PL (61–80)	4.91 (fixed)	4.59 (fixed)	
	<i>XMM–Newton</i> (2) ^a	BB+PL (81–97)	4.91 (fixed)	4.59 (fixed)	
		BB+PL	4.9 (fixed)	4.65 (fixed)	
		BB+PL	5.0 ± 0.1	$4.71^{+0.10}_{-0.07}$	
		BB	0.57 (fixed)	–	
SGR 0418+5729 (2009)	<i>XMM–Newton</i> (11)	2BB (1)	$0.57^{+0.04}_{-0.03}$	–	Table A10
		BB (2–11)	0.57 (fixed)	–	
	<i>Chandra</i> (4)	BB	0.57 (fixed)	–	
SGR 1833–0832 (2010)	<i>Swift</i> (27)	BB	13.1 ± 0.9	–	Table A11
		BB	15.5 ± 0.4	–	
	<i>Chandra</i> (1)	BB	13.7 ± 0.9	–	
Swift J1822.3–1606 (2011)	<i>Swift</i> (60)	BB+PL (1–20)	0.68 (fixed)	0.289 (fixed)	Table A12
		BB+PL (21–40)	0.68 (fixed)	0.289 (fixed)	
	<i>XMM–Newton</i> (5)	BB+PL (40–60)	0.68 (fixed)	0.289 (fixed)	
		BB+PL	0.68 ± 0.01	0.289 ± 0.004	
		BB+PL	0.62 ± 0.02	0.283 ± 0.005	
Swift J1834.9–0846 (2011)	<i>Swift</i> (19)	BB	19 (fixed)	–	Table A13
	<i>XMM–Newton</i> (3)	BB	15 ± 1	–	
	<i>Chandra</i> (4)	BB	19 ± 1	–	
CXOU J164710.2–455216 (2011)	<i>Swift</i> (7)	BB	2.6 ± 0.3	–	Table A14
		2BB	2.5 ± 0.1	–	
	<i>Chandra</i> (1)	BB	2.8 ± 0.1	–	
1E 1048.1–5937 (2011)	<i>Swift</i> (55)	BB (1–20)	0.61 ± 0.02	–	Table A15
		BB (21–40)	0.61 (fixed)	–	
		BB (40–55)	0.56 (fixed)	–	
1E 2259+586 (2012)	<i>Swift</i> (44)	2BB (1–20)	0.38 ± 0.01	–	Table A16
		2BB (21–44)	0.38 (fixed)	–	
SGR 1745–2900 (2013)	<i>Chandra</i> (35)	BB	18.7 ± 0.1	–	Table A17
SGR 1935+2154 (2014)	<i>Swift</i> (45)	BB (1–20)	2.3 ± 0.2	–	Table A18
		BB (21–45)	2.3 (fixed)	–	
	<i>XMM–Newton</i> (9)	2BB	2.37 ± 0.07	–	
		2BB	2.8 ± 0.1	–	
1E 1048.1–5937 (2016)	<i>Swift</i> (60)	BB (1–20)	0.56 ± 0.04	–	Table A19
		BB (21–40)	0.59 ± 0.04	–	
		BB (40–60)	0.56 (fixed)	–	
PSR J1119–6127 (2016)	<i>Swift</i> (35)	BB (1–20)	0.69 ± 0.05	–	Table A20
		BB (21–36)	0.69 (fixed)	–	
1E 161348–5055 (1999, 2016)	<i>Chandra</i> (25), <i>XMM–Newton</i> (2), <i>Swift</i> (129)	2BB	2.05 ± 0.05	–	Rea et al. (2016)

Notes. ^aThe absorption column density was fixed to a value compatible with that inferred from the fits of the data sets from the other X-ray instruments, because a significant excess in the fit residuals was detected below about 1 keV independently on the choice of the background region and of the adopted spectral model (see e.g. Bernardini et al. 2009 for this issue). We obtained acceptable fits in all cases.

^bThe absorption column density was fixed to the value obtained from the fit to the *XMM–Newton* spectra, because the XRT was operating in WT in all cases and bumps of instrumental origin were present at $\sim 0.8 – 1$ keV (see the text). We obtained acceptable fits in all cases.

Table 2. Results of the empirical modelling of the outburst decays for the 0.3–10 keV luminosities of the single spectral components (BB, PL, BB1, BB2, BB3) and for the total bolometric luminosities. The cooling curves were fitted with one or multiple exponential functions plus a constant (see the text for details). Uncertainties on the best-fitting parameters are quoted at the 1σ c.l. for a single parameter of interest. The total outburst energy is also reported. The values for PSR J1846–0258 and the first outburst of 1E 161348–5055 are taken from Gavriil et al. (2008), Rea et al. (2016), respectively. The values for the second outburst of 1E 161348–5055 are taken from the ongoing *Swift* XRT monitoring campaign.

Source	Component	Best-fitting decay model	τ (d)	$\tau_1 / \tau_2 / \tau_3$ (d)	E (erg)
SGR 1627–41 (1998)	BB/bol	2EXP	–	$234^{+37}_{-38} / 1307^{+373}_{-245}$	2×10^{42}
1E 2259+586 (2002)	BB1	EXP	1.41 ± 0.05	–	–
	BB2	EXP	47^{+40}_{-16}	–	–
	bol	EXP	21 ± 13	–	10^{41}
XTE J1810–197	BB1	EXP	376^{+72}_{-58}	–	–
	BB2	EXP	372^{+33}_{-29}	–	–
	bol	EXP	328^{+44}_{-38}	–	4×10^{42}
SGR 1806–20	bol	EXP	349 ± 52	–	2×10^{43}
CXOU J1647–4552 (2006)	BB	3EXP	–	$2.9 \pm 0.7 / 91^{+54}_{-27} / 225^{+32}_{-57}$	–
	PL	2EXP	–	$3 \pm 1 / 458^{+64}_{-60}$	–
	bol	3EXP	–	$2.4^{+0.8}_{-0.6} / 53 \pm 3 / 238^{+13}_{-17}$	10^{42}
SGR 1627–41 (2008)	BB/bol	3EXP	–	$0.56^{+0.07}_{-0.06} / 31^{+5}_{-4} / 508^{+45}_{-43}$	10^{42}
SGR 0501+4516	BB	EXP	33 ± 2	–	–
	PL	2EXP	–	$9^{+3}_{-2} / 345^{+68}_{-51}$	–
	bol	2EXP	–	$13 \pm 2 / 147^{+12}_{-11}$	9×10^{40}
1E 1547–5408 (2009)	BB	2EXP	–	$4.8^{+0.7}_{-0.6} / 1131^{+156}_{-120}$	–
	PL	EXP	364 ± 15	–	–
	bol	3EXP	–	$3 \pm 1 / 109 \pm 8 / 2870^{+528}_{-416}$	2.4×10^{43}
SGR 0418+5729	BB/bol	EXP	76 ± 1	–	8×10^{40}
SGR 1833–0832	BB/bol	EXP	128^{+26}_{-4}	–	10^{42}
Swift J1822.3–1606	BB	3EXP	–	$0.78^{+0.4}_{-0.3} / 16.7^{+1.0}_{-0.9} / 207^{+12}_{-11}$	–
	PL	2EXP	–	$14.6 \pm 0.8 / 817^{+54}_{-47}$	–
	bol	3EXP	–	$7 \pm 2 / 28^{+4}_{-3} / 460^{+35}_{-31}$	3×10^{41}
Swift J1834.9–0846	BB/bol	2EXP	–	$0.08 \pm 0.01 / 17.7 \pm 0.4$	2×10^{41}
CXOU J1647–4552 (2011)	BB/bol	EXP	47 ± 16	–	6×10^{40}
1E 1048.1–5937 (2011)	BB/bol	2EXP	–	$39^{+26}_{-16} / 382^{+45}_{-31}$	8×10^{42}
1E 2259+586 (2012)	BB1	EXP	79^{+59}_{-35}	–	–
	BB2	EXP	33.7^{+9}_{-8}	–	–
	bol	EXP	206^{+115}_{-74}	–	3×10^{41}
SGR 1745–2900	BB/bol	2EXP	–	$81^{+6}_{-20} / 324^{+27}_{-17}$	10^{43}
1E 1048.1–5937 (2016)	BB/bol	2EXP	–	$42^{+8}_{-6} / 264^{+30}_{-29}$	4×10^{42}
PSR J1119–6127	bol	3EXP	–	$0.25 \pm 0.06 / 18 \pm 2 / 73 \pm 2$	8.5×10^{41}
PSR J1846–0258	bol	EXP	56 ± 6	–	4.5×10^{41}
1E 161348–5055 (2000)	bol	2EXP	–	$110^{+13}_{-15} / 856^{+29}_{-27}$	10^{43}
1E 161348–5055 (2016)	bol	2EXP	–	$0.5^{+0.2}_{-0.1} / 507^{+59}_{-49}$	2.6×10^{42}

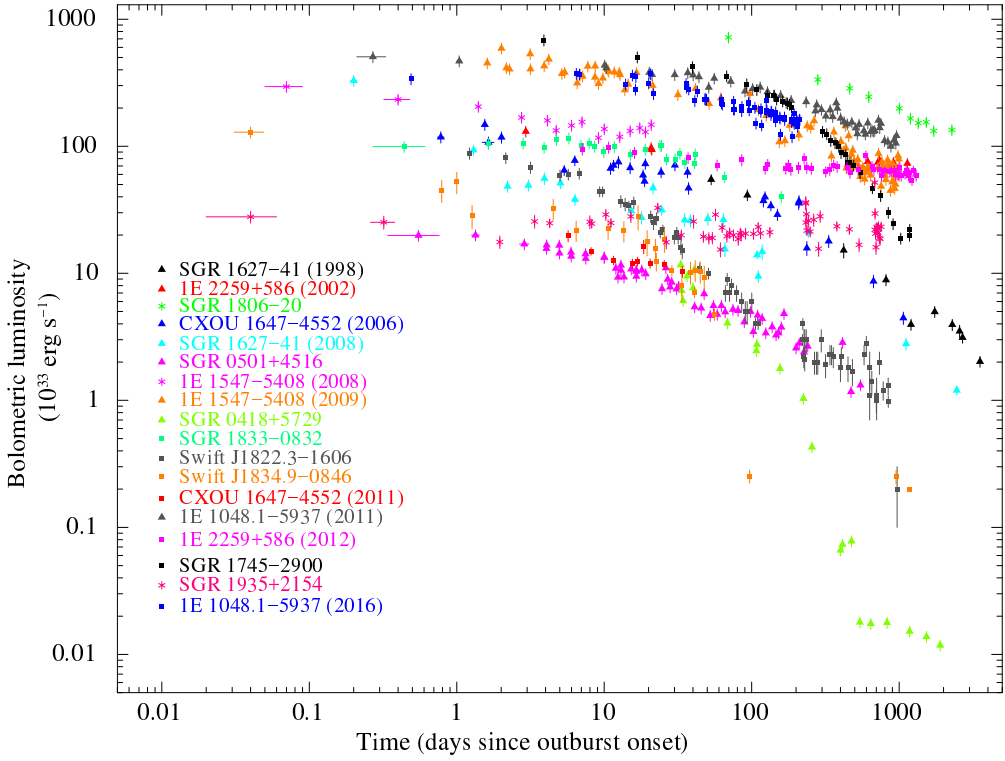


Figure 1. Temporal evolution of the bolometric (0.01–100 keV) luminosities for all outbursts re-analysed in this work. The distances assumed are those quoted in Table 5.

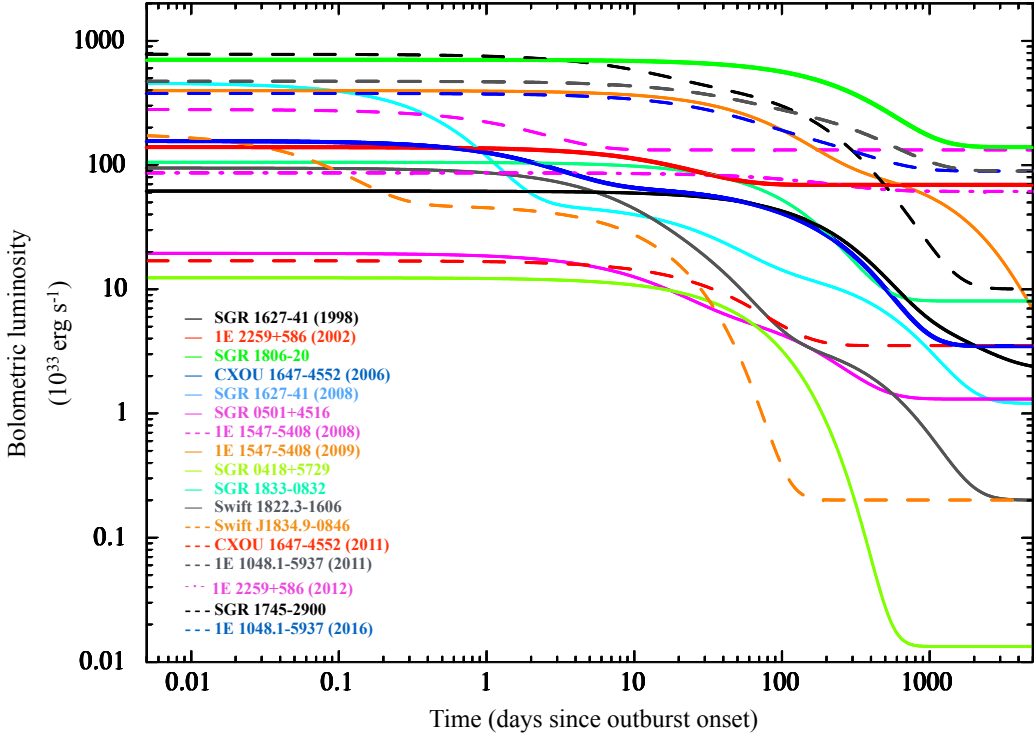


Figure 2. Models describing the temporal evolution of the bolometric (0.01–100 keV) luminosities for all outbursts re-analysed in this work.

Table 3. Maximum fluxes and luminosities (0.3–10 keV) for magnetars showing major outbursts or variations in their persistent emission. The table is ordered according to the chronological order of the outburst episodes, and the cases of the peculiar high B -field pulsars and the CCO 1E 161348–5055 are reported below the double horizontal line. Uncertainties are reported at the 1σ c.l.

Source	Date	Observatory	Obs ID	Exposure (ks)	Abs/Unabs flux (erg cm $^{-2}$ s $^{-1}$)	$L_{X,p}$ (erg s $^{-1}$)
SGR 1627–41	1998 Aug 07	<i>BeppoSAX</i>	70566001	44.9	$(2.4 \pm 0.1) \times 10^{-12}$ $(3.6 \pm 0.2) \times 10^{-12}$	$(5.2 \pm 0.3) \times 10^{34}$
SGR 1900+14	2001 Apr 22	<i>Chandra</i>	2458	20.1	$(1.02 \pm 0.02) \times 10^{-11}$ $(1.86 \pm 0.05) \times 10^{-11}$	$(3.48 \pm 0.09) \times 10^{35}$
1E 2259+586	2002 Jun 21	<i>XMM–Newton</i>	0155350301	18.4	$(5.87 \pm 0.01) \times 10^{-11}$ $(1.006 \pm 0.009) \times 10^{-10}$	$(1.23 \pm 0.01) \times 10^{35}$
XTEJ1810–197	2003 Sep 08	<i>XMM–Newton</i>	0161360301	6.6	$(3.84 \pm 0.02) \times 10^{-11}$ $(1.19 \pm 0.01) \times 10^{-10}$	$(1.74 \pm 0.01) \times 10^{35}$
SGR 1806–20	2004 Oct 06	<i>XMM–Newton</i>	0164561101	12.9	$(2.68 \pm 0.02) \times 10^{-11}$ $(4.0 \pm 0.1) \times 10^{-11}$	$(3.62 \pm 0.09) \times 10^{35}$
SGR 1900+14	2006 Mar 29	<i>Chandra</i>	6709	40.0	$(6.10 \pm 0.09) \times 10^{-12}$ $(1.20 \pm 0.03) \times 10^{-11}$	$(2.24 \pm 0.06) \times 10^{35}$
CXOUJ1647–4552	2006 Sep 21	<i>Swift</i>	00030806001	7.7	$(3.36 \pm 0.08) \times 10^{-11}$ $(6.1 \pm 0.5) \times 10^{-11}$	$(1.2 \pm 0.1) \times 10^{35}$
SGR 1627–41	2008 May 28	<i>Swift</i>	00312579001	2.0	$(1.2 \pm 0.2) \times 10^{-11}$ $(2.2 \pm 0.4) \times 10^{-11}$	$(3.2 \pm 0.6) \times 10^{35}$
SGR 0501+4516	2008 Aug 23	<i>XMM–Newton</i>	0560191501	33.8	$(4.03 \pm 0.01) \times 10^{-11}$ $(1.28 \pm 0.08) \times 10^{-10}$	$(3.4 \pm 0.2) \times 10^{34}$
1E 1547–5408	2008 Oct 03	<i>Swift</i>	00330353000	4.1	$(6.2 \pm 0.2) \times 10^{-11}$ $(9.4 \pm 0.7) \times 10^{-11}$	$(2.3 \pm 0.2) \times 10^{35}$
1E 1547–5408	2009 Jan 23	<i>Swift</i>	00340923000	1.7	$(8.2 \pm 0.5) \times 10^{-11}$ $2.0^{+1.4}_{-0.4} \times 10^{-10}$	$5^{+3}_{-1} \times 10^{35}$
SGR 0418+5729	2009 Jun 11	<i>RXTE</i>	94048–03–01–00	5.2	$(3.31 \pm 0.06) \times 10^{-11}$ $(3.41 \pm 0.06) \times 10^{-11}$	$(1.63 \pm 0.03) \times 10^{34}$
SGR 1833–0832 ^a	2010 Mar 20	<i>Swift</i>	00416485000	29.0	$(4.0 \pm 0.2) \times 10^{-12}$ $(8.5 \pm 0.7) \times 10^{-12}$	$(1.02 \pm 0.08) \times 10^{35}$
1E 1841–045	2011 Jul 02	<i>Swift</i>	00456505000	1.4	$(2.0 \pm 0.2) \times 10^{-11}$ $(2 \pm 1) \times 10^{-10}$	$(1.7 \pm 0.9) \times 10^{36}$
Swift J1822.3–1606	2011 Jul 16	<i>Swift</i>	00032033001	1.6	$(2.35 \pm 0.04) \times 10^{-10}$ $(2.61 \pm 0.05) \times 10^{-10}$	$(8.0 \pm 0.2) \times 10^{34}$
4U 0142+61	2011 Jul 29	<i>Swift</i>	00458345000	3.9	$(6.7 \pm 0.3) \times 10^{-10}$ $(7.9 \pm 0.2) \times 10^{-10}$	$(1.23 \pm 0.03) \times 10^{36}$
Swift J1834.9–0846	2011 Aug 07	<i>Swift</i>	00458907000	1.5	$(3.2 \pm 0.6) \times 10^{-11}$ $(4.8 \pm 0.8) \times 10^{-11}$	$(1.0 \pm 0.2) \times 10^{35}$
CXOUJ1647–4552	2011 Sep 25	<i>Swift</i>	00030806020	3.1	$(6.5 \pm 0.5) \times 10^{-12}$ $(1.1 \pm 0.2) \times 10^{-11}$	$(2.1 \pm 0.4) \times 10^{34}$
1E 1048.1–5937	2011 Dec 31	<i>Swift</i>	00031220066	2.0	$(4.6 \pm 0.3) \times 10^{-11}$ $(5.9 \pm 0.4) \times 10^{-11}$	$(5.7 \pm 0.4) \times 10^{35}$
1E 2259+586	2012 Apr 28	<i>Swift</i>	00032035021	3.9	$(5.7 \pm 0.1) \times 10^{-11}$ $(7.5 \pm 0.2) \times 10^{-11}$	$(9.2 \pm 0.2) \times 10^{34}$
SGR 1745–2900	2013 Apr 29	<i>Chandra</i> ^b	14701	9.7	$\sim 1.8 \times 10^{-11}$ $\sim 8.3 \times 10^{-11}$	$\sim 6.8 \times 10^{35}$
SGR 1935+2154 ^c	2014 Jul 05	<i>Swift</i>	00603488000	3.4	$(1.7 \pm 0.2) \times 10^{-12}$ $(2.6 \pm 0.4) \times 10^{-12}$	$(2.5 \pm 0.4) \times 10^{34}$
4U 0142+61	2015 Feb 28	<i>Swift</i>	00632888000	0.5	$(6.5 \pm 0.3) \times 10^{-10}$ $(8.1 \pm 0.1) \times 10^{-10}$	$(1.26 \pm 0.02) \times 10^{36}$
1E 1048.1–5937	2016 Jul 29	<i>Swift</i>	00032923249	1.4	$(3.16 \pm 0.2) \times 10^{-11}$ $(3.8 \pm 0.1) \times 10^{-11}$	$(3.7 \pm 0.1) \times 10^{35}$
PSR J1119–6127	2016 Jul 28	<i>Swift</i>	00706396000	2.2	$(4.1 \pm 0.2) \times 10^{-11}$ $(4.4 \pm 0.1) \times 10^{-11}$	$(3.72 \pm 0.08) \times 10^{35}$
PSR J1846–0258 ^d	2006 Jun 08	<i>RXTE</i>	92012–01–14–00	20.1	$\sim 1.2 \times 10^{-11}$ $\sim 9 \times 10^{-11}$	$\sim 3.9 \times 10^{35}$
1E 161348–5055	2000 Feb 08	<i>Chandra</i>	970	18.9	$(6.5 \pm 1.6) \times 10^{-11}$ $(2.66 \pm 0.06) \times 10^{-10}$	$(3.47 \pm 0.08) \times 10^{35}$
1E 161348–5055	2016 Jun 22	<i>Swift</i>	00030389032	0.6	$(1.4 \pm 0.1) \times 10^{-10}$ $(1.9 \pm 0.1) \times 10^{-10}$	$(2.5 \pm 0.1) \times 10^{35}$

Notes. ^aA distance of 10 kpc was assumed.

^bThe field around the source has been previously observed by *Swift*. In order to avoid contamination by nearby active X-ray sources, we consider here the first *Chandra* observation, which was carried out with the HRC. The flux was then estimated by assuming a blackbody model at 0.9 keV and the column density inferred from the joint fits of all *Chandra* data sets, i.e. $N_{\mathrm{H}} = 1.87 \times 10^{23} \text{ cm}^{-2}$.

^cA distance of 9 kpc was assumed.

^dWe used PIMMS to convert the absorbed 2–10 keV pulsed flux reported by Kuiper & Hermsen (2009) into unabsorbed 0.3–10 keV fluxes and luminosities.

Table 4. Quiescent fluxes and luminosities (0.3–10 keV) for magnetars showing major outbursts or variations in their persistent emission. Bolometric luminosities are also listed. Magnetars are ordered as in Table 3. Uncertainties are reported at the 1σ c.l., upper limits at the 3σ c.l.

Source	Date	Observatory	Obs ID	Exposure (ks)	Abs/Unabs flux ($\text{erg cm}^{-2} \text{s}^{-1}$)	$L_{X,q}$ (erg s^{-1})	$L_{bol,q}$ (erg s^{-1})
SGR 1627–41	2015 Feb 18	<i>XMM–Newton</i>	0742650101	19.1	$4.2^{+0.2}_{-2.1} \times 10^{-14}$ $(8 \pm 1) \times 10^{-14}$	$(1.2 \pm 0.1) \times 10^{33}$	$\sim 1.2 \times 10^{33}$
SGR 1900+14	2005 Sep 22	<i>XMM–Newton</i>	0305580201	19.1	$(3.92 \pm 0.05) \times 10^{-12}$ $(6.7 \pm 0.2) \times 10^{-12}$	$(1.25 \pm 0.04) \times 10^{35}$	$\sim 1.4 \times 10^{35}$
1E 2259+586 ^a	2014 Nov 04 – 2015 Nov 17	<i>Swift</i>	00032035087–114	40.1	$(3.55 \pm 0.02) \times 10^{-11}$ $(4.74 \pm 0.03) \times 10^{-11}$	$(5.8 \pm 0.3) \times 10^{34}$	$\sim 6.1 \times 10^{34}$
XTE J1810–197	1993 Apr 03	<i>ROSAT/PSPC</i>	RP900399N00	5.3	$\sim 5.3 \times 10^{-13}$ $\sim 1.7 \times 10^{-11}$	$\sim 2.5 \times 10^{34}$	$\sim 3.2 \times 10^{34}$
SGR 1806–20	2011 Mar 23	<i>XMM–Newton</i>	0654230401	22.4	$(5.49 \pm 0.07) \times 10^{-12}$ $(9.0 \pm 0.3) \times 10^{-12}$	$(8.2 \pm 0.3) \times 10^{34}$	$\sim 1.4 \times 10^{35}$
CXOU J1647–4552	2009 Aug 24	<i>XMM–Newton</i>	0604380101	38.2	$(8.0 \pm 0.2) \times 10^{-13}$ $(1.72 \pm 0.08) \times 10^{-12}$	$(3.3 \pm 0.2) \times 10^{33}$	$\sim 3.5 \times 10^{33}$
4U 0142+61	2004 Jul 24	<i>XMM–Newton</i>	0206670201	21.9	$(1.215 \pm 0.002) \times 10^{-10}$ $(2.309 \pm 0.003) \times 10^{-10}$	$(3.58 \pm 0.05) \times 10^{35}$	$\sim 3.8 \times 10^{35}$
SGR 0501+4516	2009 Dec 07 – 2010 Feb 21	<i>Swift</i>	0032117465–68	25.1	$(2.5 \pm 0.1) \times 10^{-12}$ $(4.4 \pm 0.3) \times 10^{-12}$	$(1.2 \pm 0.8) \times 10^{33}$	$\sim 1.3 \times 10^{33}$
1E 1547–5408	2006 Jul 01	<i>Chandra</i>	7287	9.5	$(3.2 \pm 0.3) \times 10^{-13}$ $(9 \pm 2) \times 10^{-13}$	$(2.2 \pm 0.5) \times 10^{33}$	$\sim 2.3 \times 10^{33}$
SGR 0418+5729	2014 Aug 13–18	<i>XMM–Newton</i>	0741970201–401	108.1	$(1.01 \pm 0.06) \times 10^{-14}$ $(1.6 \pm 0.2) \times 10^{-14}$	$(7 \pm 1) \times 10^{30}$	$\sim 8 \times 10^{30}$
SGR 1833–0832 ^b	2006 Sep 16	<i>XMM–Newton</i>	0400910101	8.3	$< 6 \times 10^{-14}$ $< 7 \times 10^{-13}$	$< 8 \times 10^{33}$	$< 8 \times 10^{33}$
1E 1841–045	2000 Jul 29	<i>Chandra</i> ^c	730	10.5	$(2.33 \pm 0.03) \times 10^{-11}$ $(5.00 \pm 0.04) \times 10^{-11}$	$(4.32 \pm 0.03) \times 10^{35}$	$\sim 4.6 \times 10^{35}$
Swift J1822.3–1606	2014 Mar 08	<i>XMM–Newton</i>	0722520101	40.3	$(2.3 \pm 0.8) \times 10^{-13}$ $(6.5 \pm 1.0) \times 10^{-13}$	$(2.0 \pm 0.5) \times 10^{32}$	$\sim 2.3 \times 10^{32}$
Swift J1834.9–0846	2009 Jun 06	<i>Chandra</i>	10126	46.6	$< 1 \times 10^{-14}$ $< 1 \times 10^{-13}$	$< 2 \times 10^{32}$	$< 2 \times 10^{32}$
1E 1048.1–5937	2011 Aug 06	<i>XMM–Newton</i>	0654870101	21.9	$(5.56 \pm 0.04) \times 10^{-12}$ $(8.9 \pm 0.2) \times 10^{-12}$	$(8.6 \pm 0.2) \times 10^{34}$	$\sim 8.9 \times 10^{34}$
SGR 1745–2900	1999 Sep 21 – 2012 Oct 29	<i>Chandra</i>	129 obs ^d	4808.6	$< 2 \times 10^{-14}$ $< 1.5 \times 10^{-12}$	$< 1 \times 10^{34}$	$< 1 \times 10^{34}$
SGR 1935+2154 ^e	2014 Oct 04	<i>XMM–Newton</i>	0722412701	16.1	$(8.6 \pm 0.2) \times 10^{-13}$ $(1.7 \pm 0.2) \times 10^{-12}$	$(1.6 \pm 0.1) \times 10^{34}$	$\sim 1.9 \times 10^{34}$
PSR J1119–6127	2004 Oct 31	<i>Chandra</i>	4676	60.5	$(4.8 \pm 0.6) \times 10^{-14}$ $(6.7 \pm 0.4) \times 10^{-14}$	$(5.7 \pm 0.3) \times 10^{32}$	$\sim 5.8 \times 10^{32}$
PSR J1846–0258	2000 Oct 15	<i>Chandra</i>	748	37.3	$(3.2 \pm 0.2) \times 10^{-12}$ $(3.6 \pm 0.1) \times 10^{-12}$	$(1.55 \pm 0.04) \times 10^{34}$	$\sim 2 \times 10^{34}$
1E 161348–5055	1999 Sep 26	<i>Chandra</i>	0123	13.4	$(9.8 \pm 0.6) \times 10^{-13}$ $(2.15 \pm 0.09) \times 10^{-12}$	$(2.8 \pm 0.1) \times 10^{33}$	$\sim 3 \times 10^{33}$

Notes. ^aThe steady level of the source is slightly lower after the 2012 outburst (as measured with *Swift*) compared to that after the 2002 outburst (as measured with *XMM–Newton*), but they are however consistent with each other within the uncertainties. We then consider the more precise value derived from the *XMM–Newton* data sets.

^bA distance of 10 kpc is assumed.

^cThe field around the source has been observed three times by *Chandra* (two with the ACIS set in TE mode and one in CC mode). We consider here the CC-mode observation to minimize pile-up issues.

^dSee <http://www.sgra-star.com> for the 2012 *Chandra* X-ray Visionary Project for HETGS Observations of Sgr A* (see e.g. table 1 by Neilsen et al. 2013 for the log of the observations).

^eA distance of 9 kpc was assumed.

Table 5. Distances, timing properties and timing-inferred parameters for all magnetars, high magnetic field pulsars, central compact objects, rotation-powered pulsars and X-ray dim isolated neutron stars included in our correlation study (see <http://magnetars.ice.csic.es>). Sources that underwent major and extensively monitored magnetar-like outbursts are marked in bold.

Source	Class	D (kpc)	P (s)	\dot{P} (10^{-11} s s $^{-1}$)	$B_{\text{p,dip}}^{\text{a}}$ (10^{14} G)	$\dot{E}_{\text{rot}}^{\text{b}}$ (erg s $^{-1}$)	τ_c^{c} (kyr)	Reference
SGR 1627–41^d		11	2.59	1.9	4.5	4.3×10^{34}	2	Esposito et al. (2009a)
1E 2259+586		3.2	6.98	0.048	1.2	1.3×10^{32}	230	Dib & Kaspi (2014)
XTE J1810–197		3.5	5.54	0.283	2.6	6.7×10^{32}	31	Camilo et al. (2016)
SGR 1806–20		8.7	7.55	76.95	49	7.0×10^{34}	0.2	Younes et al. (2015)
CXOU J164710.2–455216		4	10.61	0.097	2.1	3.2×10^{31}	173	Rodríguez Castillo et al. (2014)
SGR 0501+4516		1.5	5.76	0.594	3.7	1.2×10^{33}	15	Camero et al. (2014)
1E 1547–5408		4.5	2.07	4.77	6.4	2.1×10^{35}	0.7	Dib et al. (2012)
SGR 0418+5729		2	9.08	0.0004	0.1	2.1×10^{29}	~ 36000	Rea et al. (2013a)
SGR 1833–0832^e		10	7.57	0.35	3.3	3.2×10^{32}	34	Esposito et al. (2011)
Swift J1822.3–1606		1.6	8.44	0.013	0.7	8.4×10^{30}	1030	Rodríguez Castillo et al. (2016)
Swift J1834.9–0846	Magnetars	4.2	2.48	0.806	2.9	2.1×10^{34}	5	Esposito et al. (2013)
1E 1048.1–5937		9	6.46	2.18	7.6	3.2×10^{33}	4.7	Dib & Kaspi (2014)
SGR 1745–2900		8.3	3.76	3.06	6.9	2.2×10^{34}	1.9	Coti Zelati et al. (2017)
SGR 1935+2154		9	3.24	1.43	4.4	1.6×10^{34}	3.6	Israel et al. (2016)
SGR 1900+14		12.5	5.20	9.2	14.0	2.6×10^{34}	0.9	Olausen & Kaspi (2014)
4U 0142+614		3.6	8.69	0.20	2.7	1.3×10^{32}	69	Olausen & Kaspi (2014)
1E 1841–045		8.5	11.79	4.09	13.8	9.9×10^{33}	4.6	Olausen & Kaspi (2014)
1RXS J170849.0–4009		3.8	11.01	1.95	9.3	5.8×10^{32}	9.1	Olausen & Kaspi (2014)
CXOU J010043.1–721		62.4	8.02	1.88	7.9	1.4×10^{33}	6.8	Olausen & Kaspi (2014)
CXOU J171405.7–3810		13.2	3.83	6.40	10.0	4.5×10^{34}	0.95	Olausen & Kaspi (2014)
SGR 0526–66		49.7	8.05	3.8	11.0	2.9×10^{33}	3.4	Olausen & Kaspi (2014)
PSR J1119–6127		8.4	0.41	0.4	0.82	2.5×10^{36}	1.6	Viganò et al. (2013)
PSR J1846–0258		6.0	0.33	0.71	0.98	8.1×10^{36}	0.7	Viganò et al. (2013)
PSR J0726–2612	High- B pulsars	1.0	3.44	0.03	0.64	2.5×10^{32}	190	Viganò et al. (2013)
PSR J1819–1458		3.6	4.26	0.057	1.0	3.2×10^{32}	120	Viganò et al. (2013)
PSR J1718–3718		4.5	3.38	0.16	1.5	1.6×10^{33}	33	Viganò et al. (2013)
1E 161348–5055		3.3	24030	< 70	< 2600	< 2×10^{24}	> 540	Rea et al. (2016)
CXOU J185238.6+0040	CCOs	7.1	0.105	0.00000087	0.00061	3.2×10^{32}	~ 190000	Viganò et al. (2013)
1E 1207.4–5209		2.1	0.424	0.00000220	0.00196	1.2×10^{31}	~ 302000	Viganò et al. (2013)
RX J0822–4300		2.2	0.112	0.0000093	0.00058	1.9×10^{32}	~ 254000	Viganò et al. (2013)
RX J0420.0–502		0.34	3.45	0.004	0.2	2.5×10^{31}	~ 2000	Viganò et al. (2013)
RX J1856.5–375		0.12	7.06	0.003	0.3	3.2×10^{30}	~ 3800	Viganò et al. (2013)
RX J2143.0+065		0.43	9.43	0.004	0.4	2.0×10^{30}	~ 3600	Viganò et al. (2013)
RX J0720.4–312	XDINSs	0.29	8.39	0.007	0.5	4.7×10^{30}	~ 1900	Viganò et al. (2013)
RX J0806.4–412		0.25	11.37	0.0055	0.5	1.6×10^{30}	~ 3300	Viganò et al. (2013)
RX J1308.6+212		0.50	10.31	0.01	0.7	4.0×10^{30}	~ 1500	Viganò et al. (2013)
RX J1605.3+324		0.35	3.39	0.16	1.5	1.6×10^{33}	34	Viganò et al. (2013)
PSR J0538+281		1.3	0.143	0.0005	0.015	5.0×10^{34}	620	Viganò et al. (2013)
PSR B1055–52		0.73	0.197	0.0006	0.02	3.2×10^{34}	540	Viganò et al. (2013)
PSR J0633+174		0.25	0.237	0.001	0.03	3.2×10^{34}	340	Viganò et al. (2013)
PSR B1706–44	RPPs	2.6	0.102	0.009	0.06	3.2×10^{36}	17	Viganò et al. (2013)
PSR B0833–45		0.28	0.089	0.01	0.07	6.3×10^{36}	11	Viganò et al. (2013)
PSR B0656+14		0.28	0.385	0.0055	0.09	4.0×10^{34}	110	Viganò et al. (2013)
PSR B2334+61		3.1	0.495	0.02	0.2	6.3×10^{34}	41	Viganò et al. (2013)
PSR J1740+100		1.4	0.154	0.2	0.4	2.5×10^{37}	1.2	Viganò et al. (2013)

Notes. ^a Assuming a force-free magnetosphere and an aligned rotator, a star radius $R = 10$ km and moment of inertia $I = 10^{45}$ g cm 2 , the dipolar component of the surface magnetic field at the polar caps is given by $B_{\text{p,dip}} \sim 2 \cdot (3c^3 I P \dot{P} / 8\pi^2 R^6)^{1/2} \sim 6.4 \times 10^{19} (P \dot{P})^{1/2}$ G. Relativistic magnetohydrodynamic simulations of pulsar magnetospheres have shown that the estimate offered by this formula is correct within a factor of $\sim 2 - 3$ (Spitkovsky 2006).

^b With the same assumptions, the rotational energy loss is given by $\dot{E}_{\text{rot}} = 4\pi^2 I \dot{P} P^{-3} \sim 3.9 \times 10^{46} \dot{P} P^{-3}$ erg s $^{-1}$.

^c With the same assumptions and assuming that the spin period at birth was much smaller than the current value, the characteristic age is given by $\tau_c = P/2\dot{P}$.

^d The spin period and its derivative were detected only following the 2008 re-activation of the source. We assume the same spin period derivative also for the 1998 outburst, and consider the same values for $B_{\text{p,dip}}$, \dot{E}_{rot} and τ_c in our searches for correlations.

^e The value for the distance is assumed.

Table 6. Results of the search for (anti)correlations between different parameters. Letters in parentheses indicate the case of a correlation (*c*) or an anticorrelation (*a*). The decay-time-scale is defined as the *e*-folding parameter (τ) and it refers to the larger value (the parameter τ_2 in Table 2) for the cases where the outburst decay curve was modelled by more than one exponential function. Values for the significance are not reported if below 2σ . The yes / no flag in the last column indicates if a correlation or anticorrelation is predicted by either the internal crustal cooling or the untwisting bundle models for the evolution of magnetar outbursts (see the text for more details).

First parameter	Second parameter	Corr (<i>c</i>) or anticorr (<i>a</i>), Significance (σ) for Spearman / Kendall τ tests	PL index	Reference figure	Correlation expected? Internal cooling / untwisting bundle
Quiescent X-ray luminosity	Maximum luminosity increase	(<i>a</i>) , 5.7 / 4.9	-0.7	Fig. 3	Yes / yes
Spin-down luminosity	Quiescent bolometric luminosity	–	–	Fig. 4	No/no
Dipolar magnetic field	Quiescent bolometric luminosity	(<i>c</i>) , 3.2 / 2.9	2.0	Fig. 4	Does not apply
Dipolar magnetic field	Maximum luminosity	(<i>c</i>) , 2.5 / 2.4	0.5	Fig. 5	Yes/yes
Dipolar magnetic field	Decay time-scale	–	–	Fig. 5	Yes/yes
Dipolar magnetic field	Outburst energy	(<i>c</i>) , 3.7 / 3.3	1.0	Fig. 6	Yes / yes
Characteristic age	Outburst energy	(<i>a</i>) , 3.3 / 3.0	-0.4	Fig. 6	Yes / ?
Maximum luminosity	Outburst energy	(<i>c</i>) , 4.0 / 3.7	1.4	Fig. 6	Yes / yes
Quiescent bolometric luminosity	Outburst energy	–	–	Fig. 6	No / no
Maximum luminosity	Decay time-scale	–	–	Fig. 7	No / no
Outburst energy	Decay time-scale	(<i>c</i>) , 3.9 / 3.6	0.5	Fig. 7	Yes / yes
Outburst energy	Maximum luminosity increase	–	–	Fig. 8	No/no
Decay time-scale	Maximum luminosity increase	–	–	Fig. 8	No/no

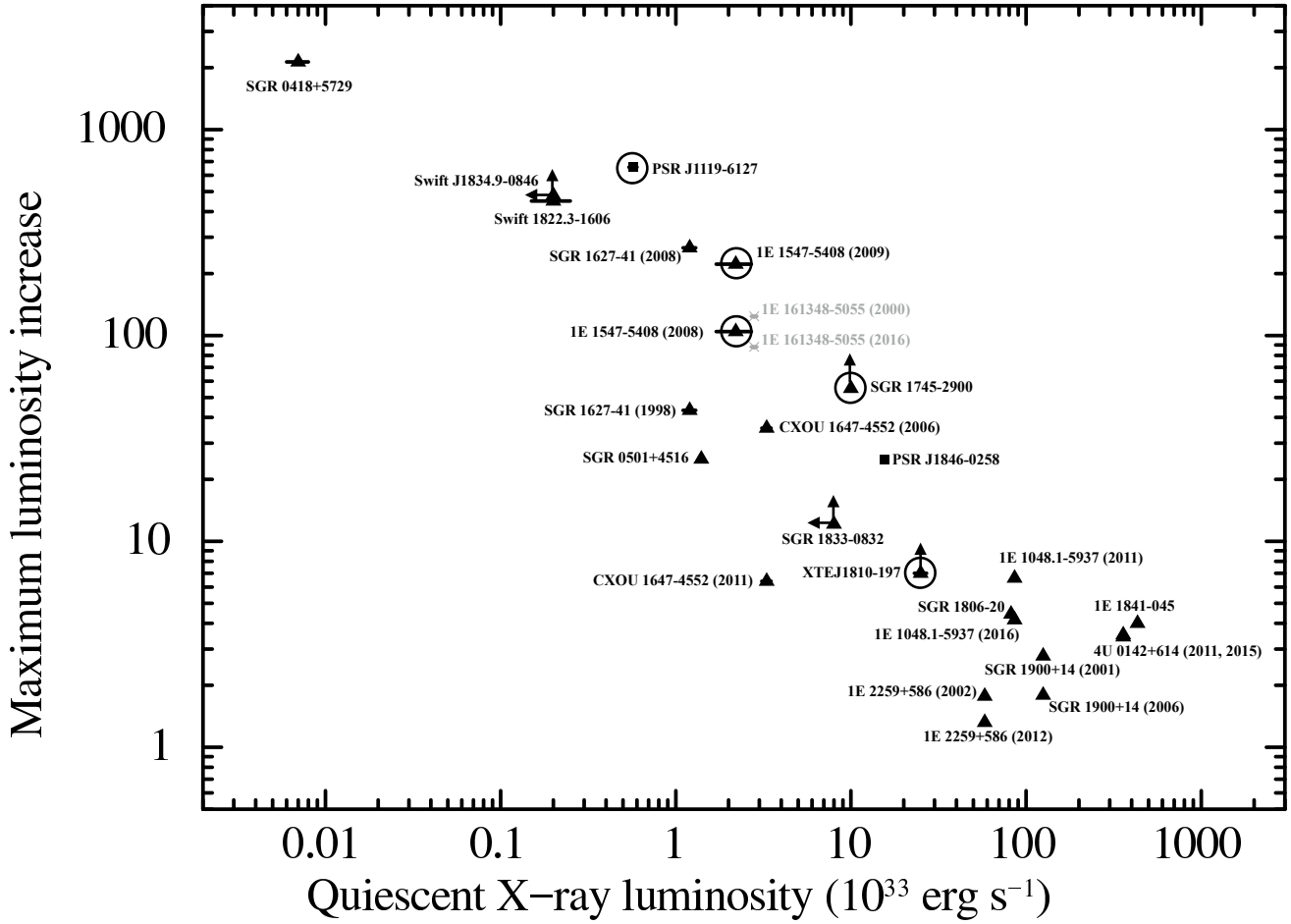


Figure 3. Maximum X-ray luminosity increase versus quiescent X-ray luminosity.

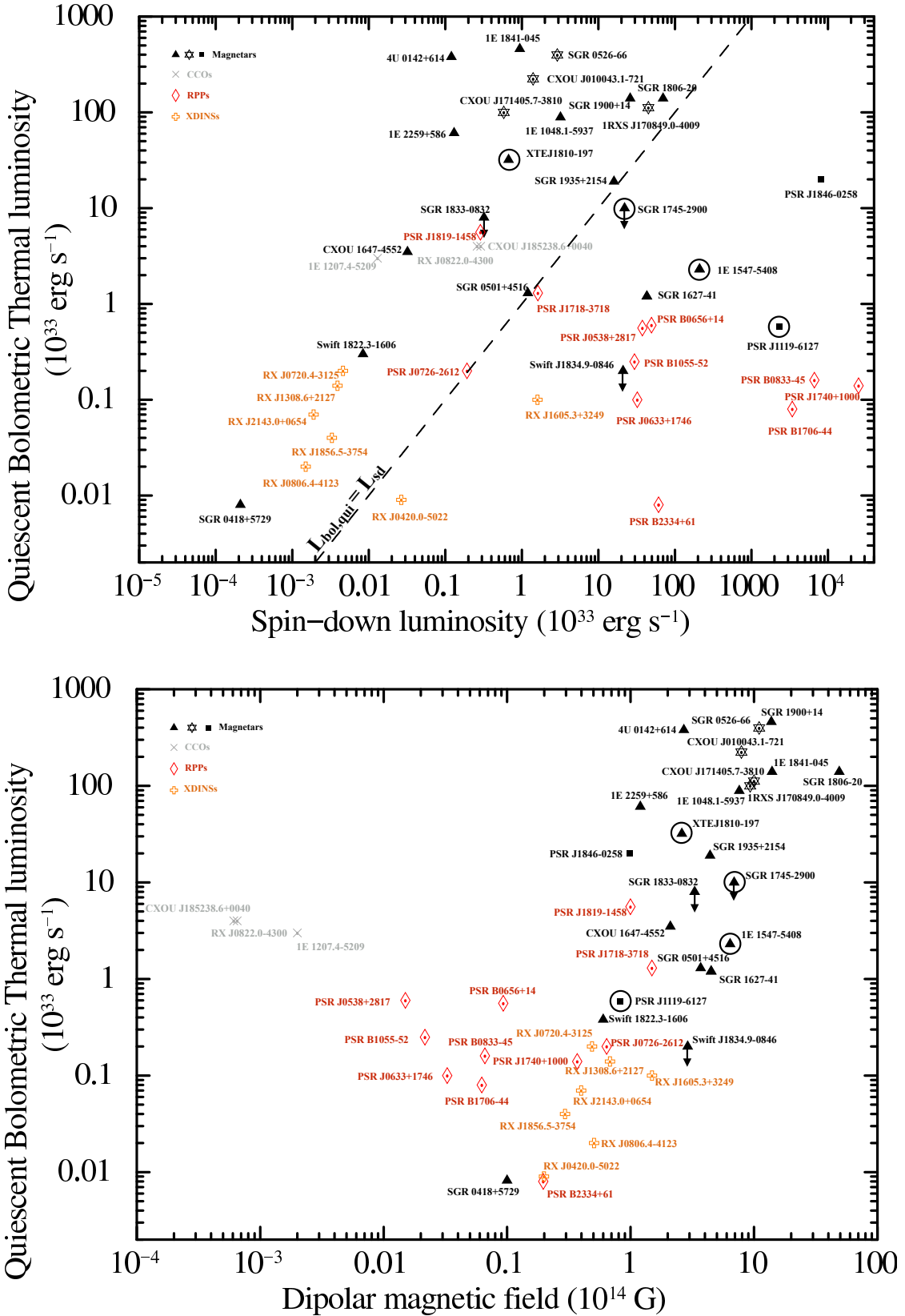


Figure 4. *Top panel:* quiescent bolometric luminosity relative to the thermal component versus the rotational energy loss rate for all isolated X-ray pulsars with clear thermal emission. The black dashed line marks the region on the diagram where the bolometric luminosity equals the spin-down luminosity. *Bottom panel:* quiescent bolometric luminosity relative to the thermal component versus the dipolar component of the magnetic field. In both figures, black triangles refer to the ‘canonical’ magnetars of our sample, black stars indicate magnetars that did not experience outburst activity, black squares denote the rotation-powered pulsars with high magnetic field that showed magnetar-like activity, light grey crosses are the central compact objects, red diamond the rotation-powered pulsars selected by Viganò et al. (2013) and orange crosses refer to the X-ray dim isolated neutron stars.

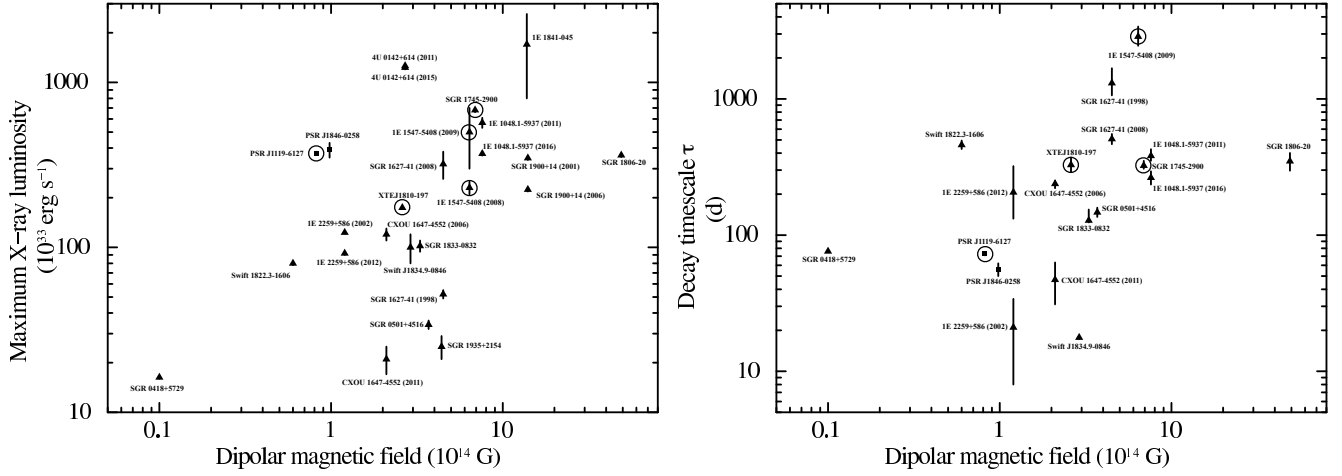


Figure 5. Left-hand panel: maximum X-ray luminosity as a function of the dipolar component of the magnetic field. Right-hand panel: decay time-scale as a function of the dipolar component of the magnetic field.

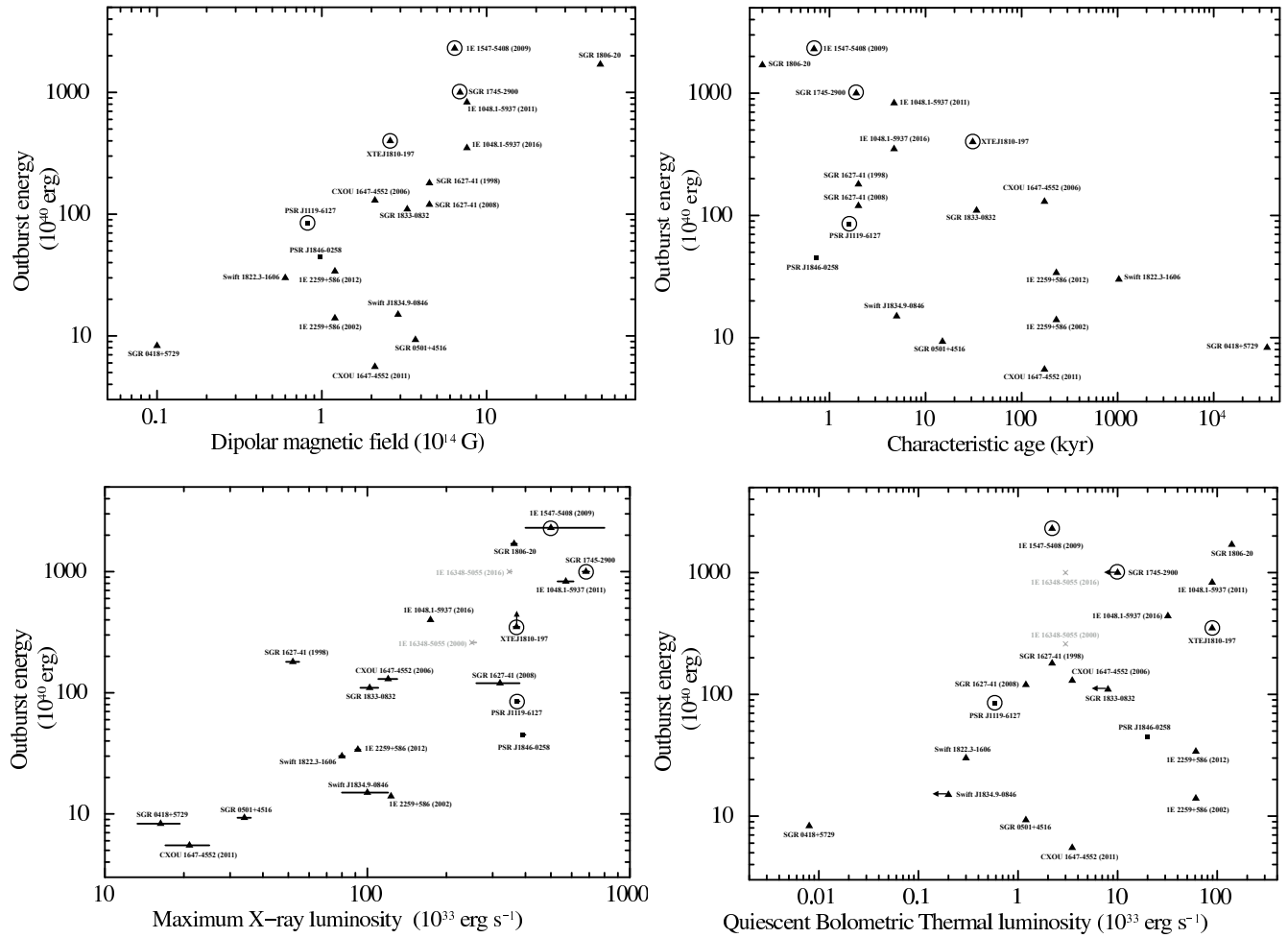


Figure 6. Top panels: total energy released during the outburst as a function of the dipolar component of the magnetic field (left), and total energy released during the outburst as a function of the characteristic age (right). Bottom panels: total energy released during the outburst versus maximum X-ray luminosity at the peak of the outburst (left), and total energy released during the outburst as a function of the quiescent bolometric luminosity relative to the thermal component (right).

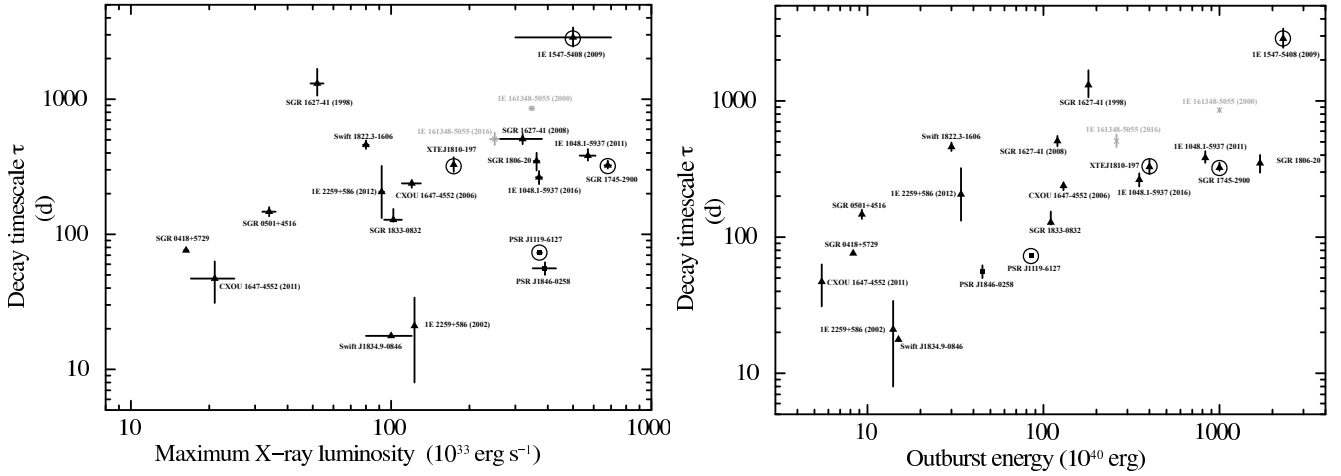


Figure 7. Left-hand panel: decay time-scale as a function of the maximum X-ray luminosity at the peak of the outburst. Right-hand panel: decay time-scale as a function of the total energy released during the outburst.

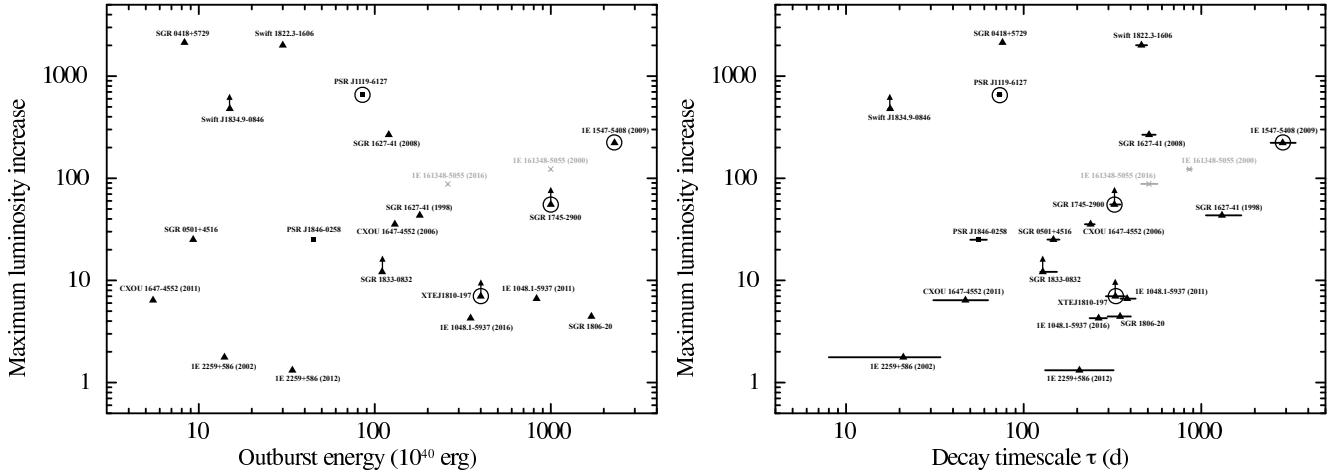


Figure 8. Left-hand panel: maximum luminosity increase as a function of the total energy released during the outburst. Right-hand panel: maximum luminosity increase as a function of the decay time-scale.

APPENDIX A: JOURNAL OF OBSERVATIONS

This Section provides a log of all observations carried out by the X-ray instruments on board the *Swift*, *XMM–Newton*, *Chandra* and *BeppoSAX* satellites, relative to the magnetar outbursts that were analysed in our study. The tables are reported following the chronological order of the outburst onsets (spanning a time interval of ~ 18 yr, from 1998 to 2016). We give references to previous papers where part of the listed observations have been already analysed. For every single observation, each table lists:

- (i) the X-ray instrument (legend: XRT = X-ray Telescope on board *Swift*; EPN = pn CCD of the EPIC camera on board *XMM–Newton*; ACIS-S = Advanced CCD Imaging Spectrometer spectroscopic array on board *Chandra*; ACIS-I = Advanced CCD Imaging Spectrometer imaging array on board *Chandra*; MECS = Medium-Energy Concentrator Spectrometer on board *BeppoSAX*);
- (ii) the operating mode of the X-ray instrument (legend: PC = photon counting; WT = windowed timing; FF = full frame; LW = large window; SW = small window; TE = timed exposure; CC = continuous clocking);
- (iii) the mid point of the observation expressed in modified Julian date (MJD);
- (iv) the time (in units of days) elapsed from the outburst onset, which is defined as the epoch when the first burst was detected in the hard X-/soft γ -rays from the target of interest as reported by the ‘Gamma-ray Burst Coordinates Network’ (http://gcn.gsfc.nasa.gov/gcn3_archive.html) and/or ‘The Astronomer’s Telegram’ website (<http://www.astronomerstelegram.org/>). Two exceptions to this definition are represented by the magnetars XTE J1810–197 and 1E 1048.1–5937, as discussed in Sections 2.3 and 2.12, respectively;
- (v) the exposure time after filtering for intrinsic source flares and bursts and, in the case of the *XMM–Newton* and *Chandra* data sets, also for particle background flaring;
- (vi) the background-subtracted count rate of the source (in units of counts s^{-1}) in the 0.3–10 keV energy band. Count rates are corrected for point spread function and vignetting effects, but not for pile-up.

Table A1. Log of all X-ray observations of SGR 1627–41 following the 1998 June outburst. The outburst onset occurred on MJD 50 979.109 (Kouveliotou 1998). Two additional *XMM–Newton* observations (obs ID: 0204500201, 0204500301, pn in FF mode) were not included because the source was detected at an off-axis angle of about 9.6 arcmin in these cases, leading to a too poor statistics for a meaningful spectral analysis. Part of these observations were already analysed by Woods et al. (1999), Kouveliotou et al. (2003), Mereghetti et al. (2006) and Esposito et al. (2008, 2009a, 2009b).

Instrument	Mode	Obs. ID	Mid point of observation (MJD)	Time since outburst onset (d)	Exposure (ks)	Source net count rate (counts s^{-1})
<i>BeppoSAX</i> /MECS ^a	—	70566001	51 032.25	53.14	44.9	0.0200 ± 0.0008
<i>BeppoSAX</i> /MECS ^a	—	70566002	51 072.51	93.41	30.4	0.0153 ± 0.0008
<i>BeppoSAX</i> /MECS ^a	—	70821005	51 399.77	420.66	80.4	0.0060 ± 0.0005
<i>BeppoSAX</i> /MECS ^a	—	70821001	51 793.58	814.47	61.3	0.0034 ± 0.0005
<i>Chandra</i> ACIS-S	TE	1981	52 182.50	1203.39	48.9	0.0049 ± 0.0003
<i>Chandra</i> ACIS-S	TE	3877	52 722.33	1743.22	25.7	0.0059 ± 0.0005
<i>XMM–Newton</i> EPN	SW	0202560101	53 270.98	2291.87	35.9	0.023 ± 0.002
<i>Chandra</i> ACIS-S	TE	5573	53 549.28	2570.17	9.8	0.0042 ± 0.0007
<i>Chandra</i> ACIS-S	TE	5574	53 668.54	2689.43	10.0	0.0038 ± 0.0006
<i>XMM–Newton</i> EPN	FF	0502140101	54 509.28	3530.17	47.5	0.0083 ± 0.0008

Note. ^aData acquired by the LECS were not considered, owing to the large value for the column density towards the source direction (the LECS is best calibrated for spectral analysis in the 0.1–4 keV range).

Table A2. Log of all X-ray observations of 1E 2259+586 following the 2002 June outburst. The outburst onset occurred on MJD 52 443.66 (Kaspi et al. 2003). An additional *Chandra* observation (obs ID: 6730, ACIS-S in TE mode) was not included owing to the combination of severe pile-up and extended emission (due to both the SNR surrounding the source and a halo from dust scattering) beyond a radial distance of about 4 arcsec. Part of these observations were already analysed by Woods et al. (2004) and Zhu et al. (2008).

Instrument	Mode	Obs. ID	Mid point of observation (MJD)	Time since outburst onset (d)	Exposure (ks)	Source net count rate (counts s^{-1})
<i>XMM–Newton</i> EPN	SW	0155350301	52 446.60	2.94	18.4	17.92 ± 0.03
<i>XMM–Newton</i> EPN	FF	0057540201	52 464.45	20.79	5.7	4.52 ± 0.03
<i>XMM–Newton</i> EPN	FF	0057540301	52 464.68	21.02	10.1	4.89 ± 0.02
<i>XMM–Newton</i> EPN	SW	0203550301	53 055.63	611.97	3.8	10.47 ± 0.05
<i>XMM–Newton</i> EPN	SW	0203550601	53 162.70	719.04	4.9	10.33 ± 0.05
<i>XMM–Newton</i> EPN	SW	0203550401	53 178.66	735.00	3.6	10.41 ± 0.05
<i>XMM–Newton</i> EPN	SW	0203550501	53 358.04	914.38	3.6	10.22 ± 0.05
<i>XMM–Newton</i> EPN	SW	0203550701	53 580.00	1136.34	3.5	9.98 ± 0.05

Table A3. Log of all *XMM–Newton* observations of XTE J1810–197 following the 2003 outburst. The outburst onset was missed and is constrained to be in the range MJD 52 595–52 662 (Ibrahim et al. 2004). Part of these observations were already analysed by Rea et al. (2004), Gotthelf et al. (2004), Halpern & Gotthelf (2005), Gotthelf & Halpern (2005), Bernardini et al. (2009, 2011a), Alford & Halpern (2016), Camilo et al. (2016) and Pintore et al. (2016).

Instrument	Mode	Obs. ID	Mid point of observation (MJD)	Time since outburst onset (d)	Exposure (ks)	Source net count rate (counts s ⁻¹)
<i>XMM–Newton</i> EPN	SW	0161360301	52 890.61	229–296	6.6	10.04 ± 0.04
<i>XMM–Newton</i> EPN	LW	0161360501	53 075.59	414–481	2.5	5.50 ± 0.05
<i>XMM–Newton</i> EPN	LW	0164560601	53 266.66	605–672	21.5	3.57 ± 0.01
<i>XMM–Newton</i> EPN	LW	0301270501	53 448.23	786–853	32.3	1.832 ± 0.008
<i>XMM–Newton</i> EPN	LW	0301270401	53 633.68	972–1039	28.3	0.919 ± 0.006
<i>XMM–Newton</i> EPN	LW	0301270301	53 807.03	1145–1212	21.3	0.641 ± 0.006
<i>XMM–Newton</i> EPN	LW	0406800601	54 002.34	1340–1407	39.8	0.493 ± 0.004
<i>XMM–Newton</i> EPN	LW	0406800701	54 166.12	1504–1571	36.7	0.459 ± 0.004
<i>XMM–Newton</i> EPN	LW	0504650201	54 359.48	1698–1765	67.0	0.455 ± 0.003
<i>XMM–Newton</i> EPN	LW	0552800201	54 896.02	2234–2301	30.3	0.418 ± 0.004
<i>XMM–Newton</i> EPN	LW	0605990201	55 079.73	2418–2485	17.9	0.423 ± 0.005
<i>XMM–Newton</i> EPN	LW	0605990301	55 081.66	2420–2487	16.3	0.418 ± 0.005
<i>XMM–Newton</i> EPN	LW	0605990401	55 097.77	2436–2503	11.1	0.419 ± 0.006
<i>XMM–Newton</i> EPN	LW	0605990501	55 295.23	2633–2700	3.5	0.43 ± 0.01
<i>XMM–Newton</i> EPN	LW	0605990601	55 444.73	2783–2850	8.4	0.428 ± 0.007
<i>XMM–Newton</i> EPN	LW	0671060101	55 654.19	2992–3059	16.0	0.430 ± 0.005
<i>XMM–Newton</i> EPN	LW	0671060201	55 813.46	3152–3219	12.0	0.418 ± 0.006
<i>XMM–Newton</i> EPN	LW	0691070301	56 177.07	3515–3582	14.6	0.423 ± 0.005
<i>XMM–Newton</i> EPN	LW	0691070401	56 354.29	3692–3759	7.4	0.421 ± 0.008
<i>XMM–Newton</i> EPN	LW	0720780201	56 540.98	3879–3946	18.0	0.429 ± 0.005
<i>XMM–Newton</i> EPN	LW	0720780301	56 721.10	4059–4126	19.3	0.429 ± 0.005

Table A4. Log of all *XMM–Newton* observations of SGR 1806–20 following the 2004 December giant flare. We assume that the outburst onset occurred in concomitance with the pinnacle of the giant flare, i.e., on MJD 53 366.89613426 (e.g., Palmer et al. 2004). Part of these observations were already analysed by Tiengo et al. (2005), Esposito et al. (2007), Mereghetti, Esposito & Tiengo (2007) and Younes et al. (2015).

Instrument	Mode	Obs. ID	Mid point of observation (MJD)	Time since outburst onset (d)	Exposure (ks)	Source net count rate (counts s ⁻¹)
<i>XMM–Newton</i> EPN	SW	0164561301	53 436.49	69.59	10.5	1.56 ± 0.01
<i>XMM–Newton</i> EPN	SW	0164561401	53 647.62	280.72	22.8	1.101 ± 0.007
<i>XMM–Newton</i> EPN	SW	0406600301	53 829.45	462.55	20.5	0.876 ± 0.007
<i>XMM–Newton</i> EPN	SW	0406600401	53 988.61	621.71	22.3	0.911 ± 0.007
<i>XMM–Newton</i> EPN	SW	0502170301	54 369.82	1002.92	21.3	0.736 ± 0.006
<i>XMM–Newton</i> EPN	SW	0502170401	54 558.74	1191.84	22.7	0.600 ± 0.005
<i>XMM–Newton</i> EPN	FF	0554600301	54 714.36	1347.46	25.9	0.560 ± 0.005
<i>XMM–Newton</i> EPN	FF	0554600401	54 893.89	1526.99	22.6	0.516 ± 0.005
<i>XMM–Newton</i> EPN	FF	0604090201	55 081.97	1715.07	23.2	0.474 ± 0.005
<i>XMM–Newton</i> EPN	FF	0654230401	55 643.69	2276.79	22.4	0.423 ± 0.004

Table A5. Log of all X-ray observations of CXOU J164710.2–455216 following the 2006 September outburst. The outburst onset occurred on MJD 53 999.06587963 (Krimm et al. 2006). Two *Swift* observations (obs. ID 00030806003 and 00030806004) were carried with the XRT in both the PC and WT modes (indeed, count rates above 1 counts s⁻¹ cause an automated shift of the PC to the WT mode, to prevent heavy pile-up). We then considered only the data from the mode which resulted in the largest counting statistics. Part of these observations were already analysed by Israel et al. (2007), Woods et al. (2011), An et al. (2013) and Rodríguez Castillo et al. (2014).

Instrument	Mode	Obs. ID	Mid point of observation (MJD)	Time since outburst onset (d)	Exposure (ks)	Source net count rate (counts s ⁻¹)
<i>Swift</i> XRT	PC	00030806001	53 999.85	0.78	7.7	0.523 ± 0.008
<i>Swift</i> XRT	WT	00030806002	54 000.62	1.55	0.7	0.60 ± 0.03
<i>XMM</i> –Newton EPN	FF	0311792001	54 000.70	1.64	26.2	3.80 ± 0.01
<i>Swift</i> XRT	WT	00030806003	54 001.07	2.01	4.9	0.49 ± 0.01
<i>Swift</i> XRT	PC	00030806004	54 004.41	5.35	2.5	0.30 ± 0.01
<i>Chandra</i> ACIS-S	CC	6724	54 005.38	6.31	15.1	1.59 ± 0.01
<i>Chandra</i> ACIS-S	CC	6725	54 010.11	11.04	20.1	1.301 ± 0.009
<i>Swift</i> XRT	WT	00030806006	54 010.64	11.57	2.0	0.37 ± 0.01
<i>Swift</i> XRT	WT	00030806007	54 011.56	12.49	2.0	0.36 ± 0.01
<i>Swift</i> XRT	WT	00030806008	54 014.05	14.99	2.1	0.36 ± 0.01
<i>Chandra</i> ACIS-S	CC	6726	54 017.42	18.35	25.1	1.221 ± 0.007
<i>Swift</i> XRT	WT	00030806009	54 017.85	18.78	3.5	0.286 ± 0.009
<i>Swift</i> XRT	WT	00030806010	54 018.05	18.99	2.8	0.33 ± 0.01
<i>Swift</i> XRT	WT	00030806011	54 023.38	24.32	5.6	0.303 ± 0.008
<i>Swift</i> XRT	WT	00030806012	54 029.24	30.17	5.5	0.276 ± 0.007
<i>Swift</i> XRT	WT	00030806013	54 035.76	36.69	2.8	0.29 ± 0.01
<i>Chandra</i> ACIS-S	CC	8455	54 036.39	37.32	15.1	0.981 ± 0.008
<i>Swift</i> XRT	WT	00030806014	54 119.21	120.15	2.0	0.21 ± 0.01
<i>Swift</i> XRT	WT	00030806015	54 122.13	123.06	3.8	0.219 ± 0.008
<i>Chandra</i> ACIS-S	CC	8506	54 133.92	134.86	20.1	0.683 ± 0.006
<i>XMM</i> –Newton EPN	LW	0410580601	54 148.47	149.41	17.3	1.224 ± 0.009
<i>Swift</i> XRT	WT	00030806016	54 207.38	208.32	4.3	0.175 ± 0.007
<i>Swift</i> XRT	WT	00030806017	54 208.23	209.16	2.2	0.183 ± 0.009
<i>Swift</i> XRT	PC	00030806018	54 235.53	236.46	2.6	0.079 ± 0.006
<i>Swift</i> XRT	PC	00030806019	54 237.53	238.47	1.1	0.13 ± 0.01
<i>XMM</i> –Newton EPN	LW	0505290201	54 331.59	332.52	28.4	0.714 ± 0.005
<i>XMM</i> –Newton EPN	LW	0555350101	54 698.68	699.61	28.4	0.292 ± 0.003
<i>XMM</i> –Newton EPN	LW	0604380101	55 067.57	1068.50	38.2	0.163 ± 0.002

Table A6. Log of all X-ray observations of SGR 1627–41 following the 2008 May outburst. The outburst onset occurred on MJD 54 614.34841435 (Palmer et al. 2008). Part of these observations were already analysed by Esposito et al. (2008, 2009a, 2009b) and An et al. (2012).

Instrument	Mode	Obs. ID	Mid point of observation (MJD)	Time since outburst onset (d)	Exposure (ks)	Source net count rate (counts s ⁻¹)
<i>Swift</i> XRT	PC	00312579001	54 614.55	0.20	2.0	0.058 ± 0.006
<i>Swift</i> XRT	PC	00312579002	54 615.65	1.30	2.0	0.017 ± 0.003
<i>Swift</i> XRT	PC	00312579003	54 616.55	2.21	1.9	0.007 ± 0.002
<i>Swift</i> XRT	PC	00312579004	54 617.41	3.06	1.8	0.009 ± 0.003
<i>Swift</i> XRT	PC	00312579005	54 618.27	3.93	2.0	0.010 ± 0.002
<i>Swift</i> XRT	PC	00312579006	54 619.40	5.05	2.1	0.009 ± 0.002
<i>Chandra</i> ACIS-S	CC	9126	54 620.68	6.33	40.0	0.029 ± 0.002
<i>Swift</i> XRT	PC	00312579007	54 623.48	9.13	0.6	<0.01 ^a
<i>Swift</i> XRT	PC	00312579008	54 626.65	12.30	0.3	<0.02 ^a
<i>Swift</i> XRT	PC	00312579009	54 629.62	15.27	1.9	0.006 ± 0.002
<i>Swift</i> XRT	PC	00312579010	54 632.26	17.91	3.8	0.005 ± 0.001
<i>Swift</i> XRT	PC	00312579011	54 635.78	21.43	2.3	0.010 ± 0.002
<i>Swift</i> XRT	PC	00312579012	54 638.88	24.54	5.2	0.007 ± 0.001
<i>Swift</i> XRT	PC	00312579013	54 649.47	35.12	1.5	0.004 ± 0.002
<i>Swift</i> XRT	PC	00312579014	54 652.78	38.43	5.6	0.005 ± 0.001
<i>Swift</i> XRT	PC	00312579015	54 664.76	50.41	7.0	0.0047 ± 0.0009
<i>Swift</i> XRT	PC	00312579016	54 678.64	64.29	5.2	0.006 ± 0.001
<i>Swift</i> XRT	PC	00312579017	54 680.14	65.80	1.7	0.002 ± 0.001
<i>Swift</i> XRT	PC	00312579018	54 723.19	108.84	3.2	0.003 ± 0.001
<i>Swift</i> XRT	PC	00312579019	54 724.26	109.91	0.6	<0.007 ^a
<i>Swift</i> XRT	PC	00312579020	54 725.19	110.84	3.5	0.002 ± 0.001
<i>Swift</i> XRT	PC	00312579022	54 732.09	117.75	3.2	0.005 ± 0.001
<i>XMM</i> –Newton EPN	FF	0560180401	54 734.76	120.41	94.7	0.0226 ± 0.0005
<i>Chandra</i> ACIS-S	TE	10519	54 856.86	242.51	6.6	0.018 ± 0.002
<i>Chandra</i> ACIS-I	TE	12528 ^b	55 728.17	1113.83	19.0	0.0026 ± 0.0004
<i>Chandra</i> ACIS-I	TE	12529 ^b	55 728.41	1114.06	19.0	0.0027 ± 0.0004
<i>XMM</i> –Newton EPN	FF	0742650101	57 071.56	2457.21	19.1	0.0046 ± 0.0007

Notes. ^aThe upper limit is quoted at the 3σ c.l., and is derived by applying the prescription for low number statistics given by Gehrels (1986). The corresponding upper limits on the fluxes and luminosities were estimated by assuming an absorbed blackbody spectral model with the same parameters as those of the spectra of the closeby observations.

^bThe spectral files and responses of these observations were combined to improve the fit statistics.

Table A7. Log of all X-ray observations of SGR 0501+4516 following the 2008 August outburst. The outburst onset occurred on MJD 54 700.52915509 (Barthelmy et al. 2008). All reported count rates are not corrected for pile-up. One *Chandra* observation was performed with the HRC-I (obs. ID 9131) and was not included in our analysis. Part of these observations were already analysed by Rea et al. (2009), Göğüş et al. (2010b) and Camero et al. (2014).

Instrument	Mode	Obs. ID	Mid point of observation (MJD)	Time since outburst onset (d)	Exposure (ks)	Source net count rate (counts s ⁻¹)
<i>Swift</i> XRT	PC	00321174000	54 701.08	0.55	37.1	0.738 ± 0.004
<i>XMM</i> –Newton EPN	SW	0560191501	54 701.33	0.80	33.8	8.48 ± 0.02
<i>Swift</i> XRT	PC	00321174001	54 701.87	1.34	14.6	0.651 ± 0.007
<i>Chandra</i> ACIS-S	CC	10164	54 703.40	2.87	36.5	4.51 ± 0.01
<i>Swift</i> XRT	WT	00321174003	54 704.59	4.06	9.0	0.80 ± 0.01
<i>Swift</i> XRT	WT	00321174004	54 705.60	4.07	16.3	0.615 ± 0.006
<i>Swift</i> XRT	WT	00321174005	54 705.48	4.96	10.6	0.780 ± 0.009
<i>Swift</i> XRT	WT	00321174006	54 705.50	4.97	14.5	0.762 ± 0.006
<i>Swift</i> XRT	WT	00321174007	54 706.49	5.96	25.0	0.756 ± 0.006
<i>Swift</i> XRT	WT	00321174008	54 706.51	5.98	7.9	0.697 ± 0.009
<i>XMM</i> –Newton EPN	SW	0552971101	54 707.44	6.91	17.1	7.12 ± 0.02
<i>Swift</i> XRT	WT	00321174009	54 708.00	7.47	43.5	0.766 ± 0.004
<i>Swift</i> XRT	WT	00321174010	54 708.02	7.49	20.7	0.669 ± 0.006
<i>XMM</i> –Newton EPN	SW	0552971201	54 709.57	9.04	7.2	6.68 ± 0.03
<i>Swift</i> XRT	WT	00321174011	54 710.55	10.02	67.6	0.728 ± 0.003
<i>Swift</i> XRT	WT	00321174012	54 710.52	10.00	32.2	0.556 ± 0.004
<i>XMM</i> –Newton EPN	SW	0552971301	54 711.54	11.01	14.3	6.05 ± 0.02
<i>Swift</i> XRT	WT	00321174013	54 712.52	11.99	6.1	0.71 ± 0.01
<i>Swift</i> XRT	WT	00321174014	54 712.93	12.40	2.0	0.58 ± 0.02
<i>Swift</i> XRT	WT	00321174017	54 713.51	12.98	2.8	0.70 ± 0.02
<i>Swift</i> XRT	WT	00321174018	54 713.52	12.99	16.7	0.695 ± 0.006
<i>Swift</i> XRT	WT	00321174019	54 714.13	13.61	2.1	0.65 ± 0.02
<i>Swift</i> XRT	WT	00321174020	54 715.78	15.25	1.3	0.36 ± 0.02
<i>Swift</i> XRT	WT	00321174021	54 717.02	16.50	4.6	0.62 ± 0.01
<i>Swift</i> XRT	WT	00321174022	54 717.00	16.47	44.0	0.640 ± 0.004
<i>Swift</i> XRT	WT	00321174023	54 717.01	16.48	14.7	0.642 ± 0.007
<i>Swift</i> XRT	WT	00321174024	54 718.50	17.97	1.8	0.53 ± 0.02
<i>Swift</i> XRT	WT	00321174025	54 719.66	19.13	1.1	0.58 ± 0.02
<i>Swift</i> XRT	WT	00321174026	54 725.19	24.66	1.0	0.39 ± 0.02
<i>Swift</i> XRT	WT	00321174027	54 726.75	26.22	1.0	0.53 ± 0.02
<i>Swift</i> XRT	WT	00321174028	54 727.47	26.94	1.7	0.47 ± 0.02
<i>Swift</i> XRT	WT	00321174029	54 728.52	27.99	1.6	0.43 ± 0.02
<i>Swift</i> XRT	WT	00321174030	54 729.19	28.66	1.3	0.45 ± 0.02
<i>Swift</i> XRT	WT	00321174032	54 731.49	30.96	1.7	0.50 ± 0.02
<i>Swift</i> XRT	WT	00321174033	54 732.56	32.04	1.1	0.46 ± 0.02
<i>XMM</i> –Newton EPN	LW	0552971401	54 739.29	38.76	28.1	3.22 ± 0.01
<i>Swift</i> XRT	WT	00321174036	54 741.57	41.04	0.9	0.29 ± 0.02
<i>Swift</i> XRT	WT	00321174037	54 745.96	45.43	1.5	0.36 ± 0.02
<i>Swift</i> XRT	WT	00321174038	54 748.09	47.57	1.0	0.26 ± 0.02
<i>Swift</i> XRT	WT	00321174039	54 752.83	52.30	2.5	0.31 ± 0.01
<i>Swift</i> XRT	WT	00321174040	54 755.54	55.01	3.8	0.36 ± 0.01
<i>Swift</i> XRT	WT	00321174041	54 758.95	58.42	4.1	0.326 ± 0.009
<i>Swift</i> XRT	WT	00321174042	54 762.86	62.34	3.7	0.35 ± 0.01
<i>Swift</i> XRT	WT	00321174043	54 766.61	66.09	4.2	0.284 ± 0.008
<i>Swift</i> XRT	WT	00321174044	54 775.16	74.63	2.9	0.31 ± 0.01
<i>Swift</i> XRT	WT	00321174045	54 781.36	80.84	3.5	0.292 ± 0.009
<i>Swift</i> XRT	WT	00321174046	54 789.69	89.16	3.3	0.254 ± 0.009
<i>Swift</i> XRT	WT	00321174047	54 798.63	98.11	3.2	0.29 ± 0.01
<i>Swift</i> XRT	WT	00321174048	54 803.13	102.60	2.4	0.25 ± 0.01
<i>Swift</i> XRT	WT	00321174049	54 810.22	109.70	3.5	0.264 ± 0.009
<i>Swift</i> XRT	WT	00321174050	54 818.20	117.68	3.6	0.242 ± 0.008
<i>Swift</i> XRT	WT	00321174051	54 825.07	124.55	4.5	0.227 ± 0.007
<i>Swift</i> XRT	WT	00321174053	54 838.18	137.65	4.4	0.237 ± 0.007
<i>Swift</i> XRT	WT	00321174054	54 846.86	146.33	2.8	0.224 ± 0.009
<i>Swift</i> XRT	WT	00321174055	54 852.51	151.98	4.5	0.251 ± 0.008
<i>Swift</i> XRT	WT	00321174056	54 859.51	158.98	3.3	0.215 ± 0.008

Table A7. – *continued*

Instrument	Mode	Obs. ID	Mid point of observation (MJD)	Time since outburst onset (d)	Exposure (ks)	Source net count rate (counts s ⁻¹)
<i>Swift</i> XRT	WT	00321174057	54 866.12	165.60	3.3	0.253 ± 0.009
<i>Swift</i> XRT	WT	00321174058	54 900.33	199.80	4.6	0.183 ± 0.006
<i>Swift</i> XRT	WT	00321174059	54 910.38	209.85	6.0	0.177 ± 0.005
<i>Swift</i> XRT	WT	00321174060	54 926.39	225.87	3.9	0.177 ± 0.007
<i>Swift</i> XRT	WT	00321174061	54 940.56	240.04	5.2	0.126 ± 0.005
<i>XMM–Newton</i> EPN	SW	0604220101	55 073.93	373.40	24.6	0.224 ± 0.003
<i>Swift</i> XRT	PC	00321174062	55 111.81	411.29	3.3	0.074 ± 0.005
<i>Swift</i> XRT	PC	00321174063	55 114.81	414.29	3.9	0.077 ± 0.004
<i>Swift</i> XRT	PC	00321174064	55 115.29	414.76	6.0	0.100 ± 0.004
<i>Swift</i> XRT	PC	00321174065	55 172.27	471.75	13.4	0.072 ± 0.002
<i>Swift</i> XRT	PC	00321174066	55 245.45	544.92	2.3	0.073 ± 0.006
<i>Swift</i> XRT	PC	00321174067	55 246.89	546.36	4.4	0.069 ± 0.004
<i>Swift</i> XRT	PC	00321174068	55 248.62	548.10	5.0	0.065 ± 0.004

Table A8. Log of all X-ray observations of 1E 1547–5408 following the 2008 October outburst. The outburst onset occurred on MJD 54 742.39453704 (Krimm et al. 2008). All reported count rates are not corrected for pile-up. Part of these observations were already analysed by Israel et al. (2010), Ng et al. (2011), Dib et al. (2012) and Kuiper et al. (2012).

Instrument	Mode	Obs. ID	Mid point of observation (MJD)	Time since outburst onset (d)	Exposure (ks)	Source net count rate (counts s ⁻¹)
<i>Swift</i> XRT	PC	00330353000	54 742.46	0.07	4.1	0.60 ± 0.01
<i>Swift</i> XRT	WT	00330353001	54 742.80	0.40	14.2	0.539 ± 0.006
<i>Swift</i> XRT	WT	00330353002	54 743.79	1.40	4.8	0.45 ± 0.01
<i>Swift</i> XRT	WT	00330353004	54 745.14	2.75	10.5	0.389 ± 0.006
<i>Swift</i> XRT	WT	00330353005	54 746.51	4.12	7.7	0.407 ± 0.007
<i>Chandra</i> ACIS-S	CC	8811	54 746.60	4.21	12.1	1.39 ± 0.01
<i>Swift</i> XRT	WT	00330353006	54 747.11	4.72	4.5	0.380 ± 0.009
<i>Swift</i> XRT	WT	00330353007	54 748.39	6.00	3.7	0.314 ± 0.009
<i>Swift</i> XRT	WT	00330353008	54 749.46	7.07	3.9	0.328 ± 0.009
<i>Chandra</i> ACIS-S	CC	8812	54 749.50	7.11	15.1	1.209 ± 0.009
<i>Swift</i> XRT	WT	00330353010	54 751.53	9.14	3.7	0.309 ± 0.009
<i>Swift</i> XRT	WT	00330353011	54 752.40	10.01	3.4	0.31 ± 0.01
<i>Swift</i> XRT	WT	00330353012	54 755.14	12.75	4.0	0.303 ± 0.009
<i>Swift</i> XRT	WT	00330353013	54 757.38	14.99	5.0	0.352 ± 0.008
<i>Chandra</i> ACIS-S	CC	8813	54 757.60	15.21	10.1	1.20 ± 0.01
<i>Swift</i> XRT	WT	00330353014	54 759.80	17.41	3.9	0.322 ± 0.009
<i>Chandra</i> ACIS-S	CC	10792	54 760.80	18.41	10.1	1.11 ± 0.01
<i>Swift</i> XRT	WT	00330353015	54 761.43	19.04	3.9	0.35 ± 0.01
<i>Swift</i> XRT	WT	00330353016	54 763.21	20.82	3.6	0.34 ± 0.01
<i>Chandra</i> ACIS-S	CC	8814	54 765.10	22.71	23.1	1.032 ± 0.007

Table A9. Log of all X-ray observations of 1E 1547–5408 following the 2009 January outburst. The outburst onset occurred on MJD 54 853.03740937 (Connaughton & Briggs 2009). All reported count rates are not corrected for pile-up. We did not include the following *Swift* observations: obs. ID 0003095041, because the source PSF falls on a column of bad pixels in this case; obs. ID 00030956050, 00090404025 and 00091032011, owing to the low number of net source counts (about 80 counts in the former two cases and 40 counts in the latter case). Part of these observations were already analysed by Bernardini et al. (2011b), Ng et al. (2011), Scholz & Kaspi (2011), Dib et al. (2012) and Kuiper et al. (2012).

Instrument	Mode	Obs. ID	Mid point of observation (MJD)	Time since outburst onset (d)	Exposure (ks)	Source net count rate (counts s ⁻¹)
<i>Swift</i> XRT	PC	00340923000	54 854.65	1.61	1.7	0.99 ± 0.02
<i>Chandra</i> /HETG	CC	10185	54 855.04	2.00	10.1	1.04 ± 0.01
<i>Swift</i> XRT	WT	00090007026	54 855.05	2.01	8.2	1.18 ± 0.01
<i>Swift</i> XRT	PC	00340986000	54 855.21	2.17	2.9	0.77 ± 0.02
<i>Swift</i> XRT	PC	00030956031	54 855.32	2.28	2.5	0.69 ± 0.02
<i>Swift</i> XRT	WT	00090007027	54 856.19	3.15	3.3	1.10 ± 0.02
<i>Swift</i> XRT	PC	00341055000	54 856.20	3.16	4.0	0.68 ± 0.01
<i>Chandra</i> ACIS-S	CC	10186	54 856.73	3.70	12.1	3.33 ± 0.02
<i>Swift</i> XRT	PC	00341114000	54 856.96	3.92	4.6	0.64 ± 0.01
<i>Swift</i> XRT	WT	00090007028	54 857.25	4.21	3.5	0.99 ± 0.02
<i>Swift</i> XRT	PC	00030956032	54 858.20	5.16	6.2	0.67 ± 0.01
<i>Swift</i> XRT	WT	00090007029	54 858.43	5.39	1.8	0.86 ± 0.02
<i>Swift</i> XRT	PC	00030956033	54 859.59	6.55	5.0	0.57 ± 0.01
<i>Swift</i> XRT	WT	00090007030	54 859.91	6.87	1.9	0.55 ± 0.02
<i>Swift</i> XRT	PC	00030956034	54 860.18	7.14	5.9	0.63 ± 0.01
<i>Swift</i> XRT	WT	00090007031	54 860.78	7.74	2.1	0.83 ± 0.02
<i>Chandra</i> ACIS-S	CC	10187	54 860.84	7.80	13.1	2.69 ± 0.01
<i>Swift</i> XRT	WT	00090007032	54 861.69	8.65	2.9	0.74 ± 0.02
<i>Swift</i> XRT	WT	00030956035	54 861.72	8.68	3.0	0.80 ± 0.02
<i>Swift</i> XRT	WT	00030956036	54 862.18	9.14	3.0	0.72 ± 0.02
<i>Swift</i> XRT	WT	00090007033	54 862.83	9.79	2.5	0.79 ± 0.02
<i>Swift</i> XRT	WT	00030956037	54 863.61	10.57	2.0	0.68 ± 0.02
<i>Swift</i> XRT	WT	00090007034	54 863.76	10.72	2.0	0.76 ± 0.02
<i>Swift</i> XRT	PC	00030956038	54 865.66	12.62	5.9	0.474 ± 0.009
<i>Swift</i> XRT	PC	00341965000	54 865.84	12.80	0.9	0.68 ± 0.03
<i>XMM–Newton</i> EPN	FF	0560181101	54 866.09	13.06	48.9	4.99 ± 0.01
<i>Swift</i> XRT	PC	00030956039	54 866.84	13.80	6.1	0.56 ± 0.01
<i>Swift</i> XRT	WT	00030956040	54 867.57	14.53	6.1	0.60 ± 0.01
<i>Chandra</i> ACIS-S	CC	10188	54 868.68	15.64	14.3	2.35 ± 0.01
<i>Swift</i> XRT	WT	00030956042	54 869.59	16.55	1.6	0.68 ± 0.02
<i>Swift</i> XRT	WT	00090007036	54 874.32	21.28	4.6	0.47 ± 0.01
<i>Swift</i> XRT	WT	00090007037	54 884.63	31.59	4.6	0.55 ± 0.01
<i>Swift</i> XRT	WT	00090007038	54 894.61	41.57	3.9	0.45 ± 0.01
<i>Swift</i> XRT	WT	00090007039	54 904.45	51.41	4.0	0.46 ± 0.01
<i>Swift</i> XRT	WT	00090007040	54 914.90	61.86	4.2	0.288 ± 0.008
<i>Swift</i> XRT	WT	00030956043	54 950.47	97.43	1.7	0.44 ± 0.02
<i>Swift</i> XRT	WT	00030956044	54 964.32	111.28	1.8	0.43 ± 0.02
<i>Swift</i> XRT	WT	00030956045	54 978.52	125.48	2.2	0.36 ± 0.01
<i>Swift</i> XRT	PC	00030956047	55 006.88	153.84	1.8	0.29 ± 0.01
<i>Swift</i> XRT	PC	00030956048	55 020.80	167.76	2.5	0.29 ± 0.01
<i>Swift</i> XRT	PC	00030956049	55 034.12	181.08	1.7	0.33 ± 0.01
<i>Swift</i> XRT	PC	00030956051	55 062.11	209.07	2.4	0.30 ± 0.01
<i>Swift</i> XRT	WT	00030956053	55 090.52	237.48	1.5	0.32 ± 0.01
<i>Swift</i> XRT	WT	00030956054	55 104.63	251.59	3.3	0.35 ± 0.01
<i>Swift</i> XRT	WT	00030956055	55 118.09	265.05	2.0	0.25 ± 0.01
<i>Swift</i> XRT	WT	00030956056	55 200.35	347.31	1.9	0.28 ± 0.01
<i>Swift</i> XRT	WT	00030956057	55 214.10	361.06	2.0	0.25 ± 0.01
<i>Swift</i> XRT	WT	00030956058	55 228.87	375.83	2.0	0.26 ± 0.01
<i>XMM–Newton</i> EPN	LW	0604880101	55 237.44	384.41	39.4	1.819 ± 0.007
<i>Swift</i> XRT	WT	00030956059	55 256.06	403.02	2.0	0.25 ± 0.01
<i>Swift</i> XRT	WT	00030956060	55 270.86	417.82	1.9	0.23 ± 0.01
<i>Swift</i> XRT	WT	00030956061	55 284.96	431.92	2.0	0.28 ± 0.01

Table A9. – *continued*

Instrument	Mode	Obs. ID	Mid point of observation (MJD)	Time since outburst onset (d)	Exposure (ks)	Source net count rate (counts s ⁻¹)
<i>Swift</i> XRT	PC	00090404001	55 287.82	434.78	0.9	0.14 ± 0.01
<i>Swift</i> XRT	PC	00090404002	55 291.37	438.33	3.6	0.180 ± 0.007
<i>Swift</i> XRT	PC	00090404003	55 298.72	445.68	5.7	0.156 ± 0.005
<i>Swift</i> XRT	PC	00090404004	55 307.90	454.86	3.5	0.195 ± 0.008
<i>Swift</i> XRT	PC	00090404005	55 317.22	464.18	2.3	0.166 ± 0.009
<i>Swift</i> XRT	PC	00090404006	55 327.63	474.59	3.0	0.171 ± 0.008
<i>Swift</i> XRT	PC	00090404007	55 337.91	484.87	3.0	0.188 ± 0.008
<i>Swift</i> XRT	PC	00090404008	55 347.50	494.46	2.9	0.187 ± 0.008
<i>Swift</i> XRT	WT	00030956062	55 357.31	504.27	2.8	0.25 ± 0.01
<i>Swift</i> XRT	PC	00090404010	55 377.39	524.35	2.8	0.181 ± 0.008
<i>Swift</i> XRT	PC	00090404011	55 387.59	534.55	3.3	0.148 ± 0.007
<i>Swift</i> XRT	PC	00090404012	55 398.77	545.73	3.2	0.167 ± 0.007
<i>Swift</i> XRT	PC	00090404013	55 407.22	554.18	3.6	0.162 ± 0.007
<i>Swift</i> XRT	PC	00090404014	55 417.41	564.37	3.0	0.193 ± 0.008
<i>Swift</i> XRT	PC	00090404015	55 427.38	574.34	2.9	0.189 ± 0.008
<i>Swift</i> XRT	PC	00090404016	55 436.25	583.21	3.6	0.171 ± 0.007
<i>Swift</i> XRT	PC	00090404017	55 447.08	594.04	3.0	0.144 ± 0.007
<i>Swift</i> XRT	PC	00090404018	55 457.53	604.49	3.1	0.180 ± 0.008
<i>Swift</i> XRT	PC	00090404019	55 467.09	614.05	3.5	0.191 ± 0.007
<i>Swift</i> XRT	PC	00090404020	55 477.26	624.22	3.5	0.159 ± 0.007
<i>Swift</i> XRT	PC	00090404021	55 487.14	634.10	3.1	0.172 ± 0.007
<i>Swift</i> XRT	PC	00090404022	55 493.86	640.82	2.8	0.186 ± 0.008
<i>Swift</i> XRT	PC	00090404023	55 567.69	714.65	3.2	0.154 ± 0.007
<i>Swift</i> XRT	PC	00090404024	55 578.14	725.10	3.0	0.179 ± 0.008
<i>Swift</i> XRT	PC	00090404026	55 607.45	754.41	2.8	0.107 ± 0.006
<i>Swift</i> XRT	PC	00090404027	55 617.27	764.23	3.2	0.134 ± 0.007
<i>Swift</i> XRT	PC	00090404028	55 627.91	774.88	3.3	0.175 ± 0.007
<i>Swift</i> XRT	PC	00090404029	55 637.86	784.82	2.3	0.148 ± 0.008
<i>Swift</i> XRT	PC	00090404030	55 647.43	794.39	2.9	0.153 ± 0.007
<i>Swift</i> XRT	PC	00091032001	55 656.33	803.29	2.5	0.128 ± 0.007
<i>Swift</i> XRT	PC	00091032002	55 666.55	813.51	3.1	0.135 ± 0.007
<i>Swift</i> XRT	PC	00091032003	55 676.45	823.41	3.3	0.141 ± 0.007
<i>Swift</i> XRT	PC	00091032004	55 687.09	834.05	2.7	0.132 ± 0.007
<i>Swift</i> XRT	PC	00091032005	55 696.83	843.79	3.2	0.148 ± 0.007
<i>Swift</i> XRT	PC	00091032006	55 706.57	853.54	2.7	0.151 ± 0.008
<i>Swift</i> XRT	PC	00091032007	55 716.46	863.42	2.8	0.138 ± 0.007
<i>Swift</i> XRT	PC	00091032008	55 726.62	873.59	3.0	0.093 ± 0.006
<i>Swift</i> XRT	PC	00091032009	55 736.73	883.69	2.3	0.156 ± 0.008
<i>Swift</i> XRT	PC	00091032011	55 749.45	896.41	1.4	0.16 ± 0.01
<i>Swift</i> XRT	PC	00091032012	55 756.27	903.23	3.0	0.154 ± 0.007
<i>Swift</i> XRT	PC	00091032013	55 766.60	913.56	2.9	0.161 ± 0.008
<i>Swift</i> XRT	PC	00091032015	55 780.15	927.11	1.5	0.14 ± 0.01
<i>Swift</i> XRT	PC	00091032016	55 786.43	933.39	1.7	0.146 ± 0.009
<i>Swift</i> XRT	PC	00091032017	55 790.71	937.68	3.3	0.164 ± 0.007
<i>Swift</i> XRT	PC	00091032018	55 796.84	943.80	2.6	0.157 ± 0.008
<i>Swift</i> XRT	PC	00091032019	55 806.41	953.37	2.9	0.150 ± 0.007
<i>Swift</i> XRT	PC	00091032020	55 816.45	963.41	3.2	0.153 ± 0.007
<i>Swift</i> XRT	WT	00091032021	55 826.23	973.20	2.6	0.25 ± 0.01
<i>Swift</i> XRT	WT	00091032022	55 836.27	983.23	3.1	0.214 ± 0.008
<i>Swift</i> XRT	PC	00091032023	55 846.88	993.84	3.0	0.146 ± 0.007
<i>Swift</i> XRT	PC	00091032024	55 856.40	1003.36	2.7	0.129 ± 0.007

Table A10. Log of all X-ray observations of SGR 0418+5729 following the 2009 June outburst. The outburst onset occurred on MJD 54 987.86167685 (van der Horst et al. 2009). Part of these observations were already analysed by Esposito et al. (2010a) and Rea et al. (2010, 2013a).

Instrument	Mode	Obs. ID	Mid point of observation (MJD)	Time since outburst onset (d)	Exposure (ks)	Source net count rate (counts s ⁻¹)
<i>Swift</i> XRT	PC	00031422001	55 020.91	33.05	2.9	0.241 ± 0.009
<i>Swift</i> XRT	PC	00031422002	55 021.41	33.54	10.6	0.249 ± 0.005
<i>Swift</i> XRT	PC	00031422003	55 022.15	34.29	5.6	0.188 ± 0.006
<i>Swift</i> XRT	WT	00031422004	55 024.32	36.46	7.1	0.286 ± 0.006
<i>Swift</i> XRT	WT	00031422006	55 027.81	39.95	7.7	0.321 ± 0.007
<i>Swift</i> XRT	WT	00031422007	55 028.51	40.65	16.4	0.276 ± 0.004
<i>XMM</i> –Newton EPN	SW	0610000601	55 056.26	68.40	45.0	1.480 ± 0.006
<i>Swift</i> XRT	PC	00031422008	55 095.42	107.56	9.4	0.067 ± 0.003
<i>Swift</i> XRT	PC	00031422009	55 096.50	108.64	7.6	0.077 ± 0.003
<i>Swift</i> XRT	PC	00031422010	55 143.49	155.63	15.1	0.046 ± 0.002
<i>Swift</i> XRT	PC	00031422011 ^{a1}	55 210.51	222.64	3.6	0.020 ± 0.002
<i>Swift</i> XRT	PC	00031422012 ^{a1}	55 211.66	223.79	3.6	0.015 ± 0.002
<i>Swift</i> XRT	PC	00031422013 ^{a1}	55 212.45	224.59	4.0	0.021 ± 0.002
<i>Swift</i> XRT	PC	00031422014 ^{a1}	55 213.36	225.50	3.7	0.024 ± 0.003
<i>Swift</i> XRT	PC	00031422015 ^{a2}	55 241.84	253.97	4.5	0.020 ± 0.002
<i>Swift</i> XRT	PC	00031422016 ^{a2}	55 242.84	254.97	4.5	0.017 ± 0.002
<i>Swift</i> XRT	PC	00031422017 ^{a2}	55 243.30	255.44	4.5	0.017 ± 0.002
<i>Swift</i> XRT	PC	00031422018 ^{a2}	55 244.68	256.82	4.6	0.016 ± 0.002
<i>Swift</i> XRT	PC	00031422019 ^{a2}	55 245.81	257.95	3.4	0.018 ± 0.002
<i>Swift</i> XRT	PC	00031422020 ^{a2}	55 246.25	258.39	3.2	0.017 ± 0.002
<i>Swift</i> XRT	PC	00031422021 ^{a3}	55 386.63	398.77	3.6	0.005 ± 0.001
<i>Swift</i> XRT	PC	00031422022 ^{a3}	55 387.87	400.00	5.1	0.0023 ± 0.0007
<i>Swift</i> XRT	PC	00031422023 ^{a3}	55 388.30	400.44	5.0	0.0026 ± 0.0008
<i>Swift</i> XRT	PC	00031422024 ^{a3}	55 389.07	401.21	5.4	0.0032 ± 0.0008
<i>Swift</i> XRT	PC	00031422025 ^{a3}	55 390.14	402.28	4.8	0.0014 ± 0.0007
<i>Chandra</i> ACIS-S	TE	12312	55 400.81	412.95	27.2	0.0170 ± 0.0008
<i>XMM</i> –Newton EPN	FF	0605852201	55 463.31	475.45	8.6	0.040 ± 0.002
<i>Chandra</i> ACIS-S	TE	13148	55 529.43	541.57	27.2	0.0045 ± 0.0004
<i>XMM</i> –Newton EPN	LW	0672670201	55 630.34	642.48	11.6	0.007 ± 0.001
<i>Chandra</i> ACIS-S	TE	13235	55 762.56	774.70	69.8	0.0034 ± 0.0002
<i>XMM</i> –Newton EPN	LW	0672670401 ^{a4}	55 813.84	825.98	25.9	0.0062 ± 0.0006
<i>XMM</i> –Newton EPN	LW	0672670501 ^{a4}	55 816.19	828.33	28.7	0.0070 ± 0.0006
<i>Chandra</i> ACIS-S	TE	13236	55 891.94	904.08	68.0	0.0029 ± 0.0002
<i>XMM</i> –Newton EPN	LW	0693100101	56 165.04	1177.18	54.3	0.0060 ± 0.0004
<i>XMM</i> –Newton EPN	LW	0723810101 ^{a5}	56 520.00	1532.14	32.7	0.0045 ± 0.0005
<i>XMM</i> –Newton EPN	LW	0723810201 ^{a5}	56 522.19	1534.33	35.3	0.0053 ± 0.0005
<i>XMM</i> –Newton EPN	LW	0741970201 ^{a6}	56 883.20	1895.34	36.0	0.0046 ± 0.0004
<i>XMM</i> –Newton EPN	LW	0741970301 ^{a6}	56 885.20	1897.33	41.2	0.0044 ± 0.0004
<i>XMM</i> –Newton EPN	LW	0741970401 ^{a6}	56 887.20	1899.34	30.9	0.0038 ± 0.0004

Note. ^aThe spectral files and responses of these observations were combined to improve the fit statistics.

Table A11. Log of all X-ray observations of SGR 1833–0832 following the 2010 March outburst. The outburst onset occurred on MJD 55 274.77418981 (Gelbord et al. 2010). Part of these observations were already analysed by Gögüs et al. (2010a) and Esposito et al. (2011).

Instrument	Mode	Obs. ID	Mid point of observation (MJD)	Time since outburst onset (d)	Exposure (ks)	Source net count rate (counts s ⁻¹)
<i>Swift</i> XRT	PC	00416485000	55 275.21	0.44	29.0	0.031 ± 0.001
<i>Swift</i> XRT	PC	00416485001	55 276.41	1.64	10.7	0.036 ± 0.002
<i>Swift</i> XRT	WT	00416485002	55 276.90	2.13	9.9	0.121 ± 0.004
<i>Swift</i> XRT	PC	00416485003	55 277.60	2.82	13.3	0.038 ± 0.002
<i>Chandra</i> ACIS-I	TE	11114	55 278.27	3.49	33.1	0.100 ± 0.002
<i>XMM</i> –Newton EPN	FF	0605851901	55 278.67	3.90	18.5	0.320 ± 0.004
<i>Swift</i> XRT	PC	00416485004	55 278.68	3.91	12.8	0.032 ± 0.002
<i>Swift</i> XRT	PC	00416485005	55 279.52	4.75	10.3	0.034 ± 0.002
<i>Swift</i> XRT	PC	00416485006	55 280.53	5.76	9.9	0.036 ± 0.002
<i>Swift</i> XRT	PC	00416485007	55 281.73	6.96	10.0	0.032 ± 0.002
<i>Swift</i> XRT	PC	00416485008	55 282.66	7.89	9.8	0.036 ± 0.002
<i>Swift</i> XRT	PC	00416485009	55 283.38	8.60	10.9	0.034 ± 0.002
<i>Swift</i> XRT	PC	00416485010	55 284.71	9.93	9.5	0.032 ± 0.002
<i>Swift</i> XRT	PC	00416485011	55 286.49	11.72	7.9	0.030 ± 0.002
<i>XMM</i> –Newton EPN	FF	0605852001	55 288.63	13.86	18.2	0.317 ± 0.005
<i>Swift</i> XRT	PC	00416485012	55 289.80	15.03	10.0	0.026 ± 0.002
<i>Swift</i> XRT	PC	00416485013	55 293.75	18.98	10.1	0.031 ± 0.002
<i>Swift</i> XRT	PC	00416485014	55 298.67	23.90	5.1	0.026 ± 0.002
<i>Swift</i> XRT	PC	50041648015	55 299.24	24.46	4.0	0.029 ± 0.003
<i>XMM</i> –Newton EPN	FF	0605852101	55 299.30	24.53	14.6	0.266 ± 0.004
<i>Swift</i> XRT	PC	00416485016	55 301.24	26.46	9.4	0.026 ± 0.002
<i>Swift</i> XRT	PC	00416485017	55 304.96	30.19	8.8	0.025 ± 0.002
<i>Swift</i> XRT	PC	00416485018	55 307.36	32.59	10.3	0.025 ± 0.002
<i>Swift</i> XRT	PC	00416485019	55 310.05	35.28	7.6	0.027 ± 0.002
<i>Swift</i> XRT	PC	00416485020	55 315.82	41.05	5.5	0.026 ± 0.002
<i>Swift</i> XRT	PC	00416485021	55 316.16	41.39	4.4	0.030 ± 0.003
<i>Swift</i> XRT	PC	00416485022	55 340.39	65.62	18.0	0.019 ± 0.001
<i>Swift</i> XRT	PC	00416485023 ^a	55 432.30	157.52	5.3	0.012 ± 0.002
<i>Swift</i> XRT	PC	00416485024 ^a	55 433.67	158.90	2.2	0.009 ± 0.002
<i>Swift</i> XRT	PC	00416485025 ^a	55 434.51	159.73	9.9	0.010 ± 0.001
<i>Swift</i> XRT	PC	00416485026 ^a	55 435.28	160.51	2.5	0.011 ± 0.002

Note. ^aThe spectral files and responses of these observations were combined to improve the fit statistics.

Table A12. Log of all X-ray observations of Swift J1822.3–1606 following the 2011 July outburst. The outburst onset occurred on MJD 55 756.53318403 (Cummings et al. 2011). We did not include the following *Swift* observations: obs. ID 00032033038, because the source was located at the edge of the detector and only a few counts were collected from the source; obs. ID 00032033041, because the source PSF falls on a column of bad pixels. Moreover, one *Chandra* observation was performed with the HRC-I (obs. ID 13511), with no sufficient spectral information, and thus was not included in our analysis as well. Part of these observations were already analysed by Livingstone et al. (2011b), Rea et al. (2012a), Scholz et al. (2012), Scholz, Kaspi & Cumming (2014) and Rodríguez Castillo et al. (2016).

Instrument	Mode	Obs. ID	Mid point of observation (MJD)	Time since outburst onset (d)	Exposure (ks)	Source net count rate (counts s ⁻¹)
<i>Swift</i> XRT	PC	00032033001	55 757.75	1.2 2	1.6	2.18 ± 0.04
<i>Swift</i> XRT	WT	00032033002	55 758.68	2.1 5	2.0	5.16 ± 0.05
<i>Swift</i> XRT	WT	00032033003	55 759.69	3.1 6	2.0	4.29 ± 0.05
<i>Swift</i> XRT	WT	00032033005	55 761.54	5.01	0.5	3.98 ± 0.09
<i>Swift</i> XRT	WT	00032033006	55 762.24	5.71	1.8	3.78 ± 0.05
<i>Swift</i> XRT	WT	00032033007	55 763.30	6.77	1.6	3.46 ± 0.05
<i>Swift</i> XRT	WT	00032033008	55 765.85	9.32	2.2	2.10 ± 0.03
<i>Swift</i> XRT	WT	00032033009	55 766.28	9.75	1.7	2.98 ± 0.04
<i>Chandra</i> ACIS-S	CC	12612	55 769.28	12.75	15.0	11.64 ± 0.03
<i>Swift</i> XRT	WT	00032033010	55 769.50	12.97	2.1	2.54 ± 0.03
<i>Swift</i> XRT	WT	00032033011	55 770.40	13.87	2.1	2.44 ± 0.03
<i>Swift</i> XRT	WT	00032033012	55 771.23	14.70	2.1	2.38 ± 0.03
<i>Swift</i> XRT	WT	00032033013	55 772.40	15.87	2.1	2.13 ± 0.03
<i>Chandra</i> ACIS-S	CC	12613	55 777.22	20.68	13.6	7.45 ± 0.02
<i>Swift</i> XRT	WT	00032051001	55 778.11	21.58	1.7	1.74 ± 0.03
<i>Swift</i> XRT	WT	00032051002	55 779.19	22.66	1.7	1.66 ± 0.03
<i>Swift</i> XRT	WT	00032051003	55 780.50	23.97	2.3	1.59 ± 0.03
<i>Swift</i> XRT	WT	00032051004	55 781.50	24.97	2.3	1.57 ± 0.03
<i>Swift</i> XRT	WT	00032051005	55 786.42	29.89	2.2	1.28 ± 0.02
<i>Swift</i> XRT	WT	00032051006	55 787.59	31.06	2.2	1.29 ± 0.02
<i>Swift</i> XRT	WT	00032051007	55 788.26	31.73	2.3	1.25 ± 0.02
<i>Swift</i> XRT	WT	00032051008	55 789.66	33.13	2.2	1.17 ± 0.02
<i>Swift</i> XRT	WT	00032051009	55 790.36	33.83	2.2	1.07 ± 0.02
<i>Swift</i> XRT	WT	00032033015	55 800.86	44.33	2.9	0.85 ± 0.02
<i>Swift</i> XRT	WT	00032033016	55 807.49	50.96	2.4	0.77 ± 0.02
<i>Chandra</i> ACIS-S	CC	12614	55 822.80	66.26	10.0	2.68 ± 0.02
<i>Swift</i> XRT	PC	00032033017	55 822.83	66.30	4.9	0.45 ± 0.01
<i>Swift</i> XRT	WT	00032033018	55 824.71	68.18	1.5	0.60 ± 0.02
<i>XMM</i> –Newton EPN	LW	0672281801	55 827.25	70.72	9.9	5.03 ± 0.02
<i>Swift</i> XRT	WT	00032033019	55 829.45	72.92	2.3	0.61 ± 0.02
<i>Swift</i> XRT	WT	00032033020	55 835.54	79.01	2.6	0.53 ± 0.01
<i>Swift</i> XRT	WT	00032033021	55 842.06	85.53	4.2	0.44 ± 0.01
<i>XMM</i> –Newton EPN	LW	0672282701	55 847.02	90.49	24.0	3.71 ± 0.01
<i>Swift</i> XRT	WT	00032033022	55 849.62	93.09	3.4	0.40 ± 0.01
<i>Swift</i> XRT	WT	00032033023	55 856.58	100.05	2.2	0.37 ± 0.01
<i>Swift</i> XRT	PC	00032033024	55 862.59	106.06	10.2	0.263 ± 0.005
<i>Chandra</i> ACIS-S	CC	12615	55 867.18	110.65	16.2	1.47 ± 0.01
<i>Swift</i> XRT	PC	00032033025	55 977.17	220.64	6.2	0.152 ± 0.005
<i>Swift</i> XRT	WT	00032033026	55 978.53	222.00	10.2	0.198 ± 0.005
<i>Swift</i> XRT	PC	00032033027	55 981.99	225.46	11.0	0.137 ± 0.004
<i>Swift</i> XRT	WT	00032033028	55 982.96	226.43	6.6	0.194 ± 0.006
<i>Swift</i> XRT	WT	00032033029	55 985.18	228.65	7.0	0.201 ± 0.006
<i>Swift</i> XRT	WT	00032033030	55 985.55	229.02	7.0	0.195 ± 0.006
<i>Swift</i> XRT	WT	00032033031	55 991.09	234.56	6.8	0.193 ± 0.006
<i>XMM</i> –Newton EPN	LW	0672282901	56 023.12	266.59	23.0	1.421 ± 0.008
<i>Swift</i> XRT	WT	00032033032	56 031.14	274.61	4.2	0.236 ± 0.008
<i>Chandra</i> ACIS-S	CC	14330	56 037.09	280.56	20.0	0.663 ± 0.006
<i>Swift</i> XRT	WT	00032033033	56 052.66	296.13	5.1	0.242 ± 0.007
<i>Swift</i> XRT	WT	00032033034	56 073.25	316.72	4.9	0.200 ± 0.007
<i>Swift</i> XRT	WT	00032033035	56 095.59	339.67	5.6	0.179 ± 0.006
<i>Swift</i> XRT	WT	00032033036	56 104.55	348.02	6.2	0.167 ± 0.005
<i>Swift</i> XRT	WT	00032033037	56 114.30	357.77	6.8	0.146 ± 0.005
<i>Swift</i> XRT	WT	00032033039	56 156.20	399.67	4.9	0.205 ± 0.007
<i>Swift</i> XRT	WT	00032033040	56 161.70	405.17	5.0	0.214 ± 0.007

Table A12. – *continued*

Instrument	Mode	Obs. ID	Mid point of observation (MJD)	Time since outburst onset (d)	Exposure (ks)	Source net count rate (counts s ⁻¹)
<i>XMM–Newton</i> EPN	LW	0672283001	56 178.85	422.32	20.2	0.950 ± 0.007
<i>Swift</i> XRT	WT	00032033042	56 206.01	449.48	5.0	0.147 ± 0.006
<i>Swift</i> XRT	WT	00032033043	56 238.71	482.18	4.9	0.117 ± 0.005
<i>Swift</i> XRT	WT	00032051010	56 334.76	578.23	9.5	0.114 ± 0.004
<i>Swift</i> XRT	WT	00032051011	56 355.40	598.87	8.2	0.142 ± 0.004
<i>Swift</i> XRT	WT	00032051012	56 386.91	630.38	2.7	0.157 ± 0.008
<i>Swift</i> XRT	WT	00032051013	56 387.28	630.75	7.7	0.180 ± 0.005
<i>Swift</i> XRT	WT	00032051014	56 409.09	652.55	8.4	0.105 ± 0.004
<i>Swift</i> XRT	WT	00032051016	56 456.35	699.82	8.8	0.141 ± 0.004
<i>Swift</i> XRT	WT	00032051017	56 459.66	703.13	7.1	0.104 ± 0.004
<i>Swift</i> XRT	WT	00032051018	56 490.67	734.14	4.0	0.142 ± 0.006
<i>Swift</i> XRT	WT	00032051019	56 491.52	734.98	18.0	0.165 ± 0.003
<i>Swift</i> XRT	WT	00032051020	56 536.11	779.58	13.8	0.132 ± 0.003
<i>Swift</i> XRT	WT	00032051021	56 598.52	841.99	6.3	0.119 ± 0.005
<i>Swift</i> XRT	WT	00032051022	56 599.99	843.46	9.1	0.128 ± 0.004
<i>XMM–Newton</i> EPN	FF	0722520101	56 724.58	968.05	40.3	0.139 ± 0.002

Table A13. Log of all X-ray observations of Swift J1834.9–0846 following the 2011 August outburst. The outburst onset occurred on MJD 55 780.83178241 (D’Elia et al. 2011). We did not include two *Swift*XRT WT-mode observations carried out within 6 h since the outburst onset (obs ID 00458907001, 00458907002) because they lasted only 91 and 141 s, respectively, and provided a low number of counts for a meaningful spectral analysis. Part of these observations were already analysed by Kargaltsev et al. (2012) and Esposito et al. (2013).

Instrument	Mode	Obs. ID	Mid point of observation (MJD)	Time since outburst onset (d)	Exposure (ks)	Source net count rate (counts s ⁻¹)
<i>Swift</i> XRT	PC	00458907000	55 780.87	0.04	1.5	0.14 ± 0.01
<i>Swift</i> XRT	WT	00458907003	55 781.62	0.79	1.7	0.05 ± 0.006
<i>Swift</i> XRT	WT	00458907004	55 781.84	1.00	1.0	0.051 ± 0.008
<i>Swift</i> XRT	WT	00458907006	55 782.10	1.27	2.7	0.053 ± 0.005
<i>Swift</i> XRT	WT	00458907007	55 785.34	4.51	5.7	0.046 ± 0.003
<i>Swift</i> XRT	WT	00458907008	55 787.28	6.45	5.4	0.033 ± 0.003
<i>Swift</i> XRT	WT	00458907009	55 791.46	10.63	8.0	0.041 ± 0.002
<i>Swift</i> XRT	WT	00458907010	55 794.43	13.60	2.5	0.038 ± 0.004
<i>Chandra</i> ACIS-S	TE	14329	55 795.74	14.91	13.0	0.071 ± 0.002
<i>Swift</i> XRT	WT	00458907011	55 797.81	16.98	0.9	0.033 ± 0.006
<i>Swift</i> XRT	WT	00458907012	55 800.35	19.52	1.9	0.029 ± 0.004
<i>Swift</i> XRT	PC	00501752000	55 803.06	22.23	2.6	0.010 ± 0.002
<i>Swift</i> XRT	WT	00458907013	55 803.38	22.54	2.2	0.029 ± 0.004
<i>Swift</i> XRT	PC	00458907014	55 806.47	25.64	2.1	0.016 ± 0.003
<i>Chandra</i> ACIS-S	TE	14055	55 809.59	28.76	16.3	0.056 ± 0.002
<i>Swift</i> XRT	PC	00458907016	55 814.45	33.61	2.0	0.007 ± 0.002
<i>Swift</i> XRT	WT	00032097001	55 819.28	38.45	9.1	0.025 ± 0.002
<i>XMM–Newton</i> EPN	FF	0679380201	55 821.80	40.96	23.7	0.116 ± 0.002
<i>Swift</i> XRT	WT	00032097002	55 822.27	41.43	10.4	0.035 ± 0.002
<i>Swift</i> XRT	WT	00032097003	55 825.60	44.77	7.7	0.033 ± 0.002
<i>Swift</i> XRT	WT	00032097004	55 828.52	47.69	8.1	0.028 ± 0.002
<i>Chandra</i> ACIS-S	TE	14056	55 836.71	55.88	24.5	0.023 ± 0.001
<i>Chandra</i> ACIS-S	TE	14057	55 877.60	96.77	37.6	0.0014 ± 0.0002
<i>XMM–Newton</i> EPN	FF	0723270101	56 733.38	952.54	58.0	0.0052 ± 0.0005
<i>XMM–Newton</i> EPN	FF	0743020201	56 946.78	1165.95	50.3	<0.003 ^a

Note. ^aThe upper limit is quoted at the 3σ c.l., and is derived by applying the EUPPER task of SAS. The corresponding upper limits on the fluxes and luminosities were estimated by assuming an absorbed blackbody spectral model with the same parameters as those of the spectrum of the penultimate *XMM–Newton* observation (obs ID: 0723270101).

Table A14. Log of all X-ray observations of CXOU J164710.2–455216 following the 2011 September outburst. The outburst onset occurred on MJD 55 823.88623843 (Baumgartner et al. 2011). Part of these observations were already analysed by An et al. (2013) and Rodríguez Castillo et al. (2014).

Instrument	Mode	Obs. ID	Mid point of observation (MJD)	Time since outburst onset (d)	Exposure (ks)	Source net count rate (counts s ⁻¹)
<i>Swift</i> XRT	PC	00030806020	55 829.58	5.69	3.1	0.103 ± 0.006
<i>XMM</i> –Newton EPN	LW	0679380501	55 832.03	8.14	15.5	0.770 ± 0.007
<i>Swift</i> XRT	PC	00030806022	55 835.46	11.57	4.3	0.063 ± 0.004
<i>Swift</i> XRT	PC	00030806023	55 839.41	15.52	3.6	0.058 ± 0.004
<i>Swift</i> XRT	PC	00030806024	55 840.72	16.83	3.7	0.065 ± 0.004
<i>Swift</i> XRT	PC	00030806025	55 842.40	18.51	3.9	0.063 ± 0.004
<i>Swift</i> XRT	PC	00030806026	55 844.37	20.48	4.0	0.064 ± 0.004
<i>Swift</i> XRT	PC	00030806027	55 849.42	25.53	8.8	0.064 ± 0.003
<i>Chandra</i> ACIS-S	TE	14360	55 857.78	33.90	19.1	0.244 ± 0.004

Table A15. Log of the X-ray observations of 1E 1048.1–5937 following the 2011 December outburst. No burst signalling the outburst onset was detected in this case. The outburst onset is thus considered to be occurred on MJD 55 926, when an increase in the X-ray flux was measured (the previous *Swift* observation was carried out on MJD 55 877.20). Part of these observations were already analysed by Archibald et al. (2015). We focus here on the observations covering the first ~ 1000 d of the outburst. We did not include the *Swift* observation 00031220126, because the source PSF falls on a column of bad pixels in this case.

Instrument	Mode	Obs. ID	Mid point of observation (MJD)	Time since outburst onset (d)	Exposure (ks)	Source net count rate (counts s $^{-1}$)
<i>Swift</i> XRT	WT	00031220066	55 926.27	0.27	2.0	0.96 ± 0.02
<i>Swift</i> XRT	WT	00031220067	55 927.04	1.04	2.0	0.91 ± 0.02
<i>Swift</i> XRT	WT	00031220068	55 936.07	10.07	2.2	0.88 ± 0.02
<i>Swift</i> XRT	WT	00031220069	55 936.32	10.32	1.1	0.85 ± 0.03
<i>Swift</i> XRT	WT	00031220070	55 937.04	11.04	1.3	0.66 ± 0.02
<i>Swift</i> XRT	WT	00031220071	55 946.19	20.19	3.2	0.74 ± 0.02
<i>Swift</i> XRT	WT	00031220073	55 947.12	21.12	2.2	0.64 ± 0.02
<i>Swift</i> XRT	WT	00031220074	55 956.05	30.05	2.0	0.72 ± 0.02
<i>Swift</i> XRT	WT	00031220077	55 962.84	36.84	6.3	0.72 ± 0.01
<i>Swift</i> XRT	WT	00031220078	55 966.09	40.09	2.3	0.74 ± 0.02
<i>Swift</i> XRT	WT	00031220081	55 969.86	43.86	7.4	0.73 ± 0.01
<i>Swift</i> XRT	WT	00031220085	55 977.14	51.14	1.9	0.46 ± 0.02
<i>Chandra</i> ACIS-S	CC	14139	55 980.95	54.95	6.1	3.09 ± 0.02
<i>Swift</i> XRT	WT	00031220086	55 981.75	55.75	5.0	0.73 ± 0.01
<i>Swift</i> XRT	WT	00031220090	55 998.15	72.15	1.8	0.58 ± 0.02
<i>Swift</i> XRT	WT	00031220095	56 016.12	90.12	1.9	0.43 ± 0.02
<i>Swift</i> XRT	WT	00031220098	56 027.44	101.44	2.0	0.61 ± 0.02
<i>Chandra</i> ACIS-S	CC	14140	56 027.56	101.56	12.0	2.68 ± 0.02
<i>Swift</i> XRT	WT	00031220099	56 040.21	114.21	1.3	0.60 ± 0.02
<i>Swift</i> XRT	WT	00031220102	56 054.10	128.10	2.2	0.59 ± 0.02
<i>Swift</i> XRT	WT	00031220105	56 068.25	142.25	0.6	0.60 ± 0.03
<i>Swift</i> XRT	WT	00031220110	56 083.25	157.25	1.9	0.59 ± 0.02
<i>Swift</i> XRT	WT	00031220113	56 097.24	171.24	1.6	0.55 ± 0.02
<i>Swift</i> XRT	WT	00031220116	56 111.24	185.24	2.1	0.51 ± 0.02
<i>Swift</i> XRT	WT	00031220133	56 160.05	234.05	1.6	0.53 ± 0.02
<i>Swift</i> XRT	WT	00031220147	56 196.04	270.04	1.6	0.39 ± 0.02
<i>Swift</i> XRT	WT	00031220148	56 202.05	276.05	1.5	0.41 ± 0.02
<i>Swift</i> XRT	WT	00031220158	56 223.27	297.27	1.5	0.44 ± 0.02
<i>Swift</i> XRT	WT	00031220167	56 244.28	318.28	1.8	0.47 ± 0.02
<i>Swift</i> XRT	WT	00031220177	56 266.34	340.34	1.5	0.39 ± 0.02
<i>Swift</i> XRT	WT	00031220181	56 280.31	354.31	1.5	0.39 ± 0.02
<i>Swift</i> XRT	WT	00031220189	56 300.28	374.28	1.3	0.37 ± 0.02
<i>Swift</i> XRT	WT	00031220192	56 307.12	381.12	1.2	0.37 ± 0.02
<i>Swift</i> XRT	WT	00031220201	56 327.30	401.30	1.2	0.46 ± 0.02
<i>Swift</i> XRT	WT	00031220211	56 349.39	423.39	1.4	0.42 ± 0.02
<i>Swift</i> XRT	WT	00031220220	56 370.20	444.20	1.6	0.40 ± 0.02
<i>Swift</i> XRT	WT	00031220224	56 403.25	477.25	1.0	0.35 ± 0.02
<i>Swift</i> XRT	WT	00031220231	56 433.07	507.07	1.2	0.39 ± 0.02
<i>Swift</i> XRT	WT	00031220234	56 446.39	520.39	1.1	0.37 ± 0.02
<i>Swift</i> XRT	WT	00031220238	56 460.46	534.46	0.8	0.38 ± 0.02
<i>XMM</i> –Newton EPN	FF	0723330101	56 496.13	570.13	48.3	2.395 ± 0.007
<i>Swift</i> XRT	WT	00031220246	56 502.12	576.12	1.5	0.36 ± 0.02
<i>Swift</i> XRT	WT	00031220249	56 516.07	590.07	1.4	0.32 ± 0.02
<i>Swift</i> XRT	WT	00032923002	56 538.55	612.55	1.4	0.37 ± 0.02
<i>Swift</i> XRT	WT	00032923008	56 566.38	640.38	1.3	0.33 ± 0.02
<i>Swift</i> XRT	WT	00032923012	56 581.48	655.48	1.5	0.35 ± 0.02
<i>Swift</i> XRT	WT	00032923014	56 594.45	668.45	1.6	0.37 ± 0.02
<i>Swift</i> XRT	WT	00032923016	56 609.42	683.42	1.4	0.36 ± 0.02
<i>Swift</i> XRT	WT	00032923023	56 650.12	724.12	1.4	0.28 ± 0.01
<i>Swift</i> XRT	WT	00032923026	56 664.07	738.07	1.4	0.30 ± 0.01
<i>Swift</i> XRT	WT	00032923029	56 678.27	752.27	0.8	0.20 ± 0.02
<i>Swift</i> XRT	WT	00032923039	56 721.45	795.45	1.7	0.28 ± 0.01
<i>Swift</i> XRT	WT	00032923048	56 763.87	837.87	1.4	0.31 ± 0.02
<i>Swift</i> XRT	WT	00032923058	56 805.72	879.72	1.3	0.32 ± 0.02
<i>Swift</i> XRT	WT	00032923069	56 848.78	922.78	1.8	0.31 ± 0.01
<i>Swift</i> XRT	WT	00032923078	56 875.20	949.20	1.5	0.29 ± 0.01
<i>Swift</i> XRT	WT	00032923082	56 885.53	959.53	1.2	0.27 ± 0.02

Table A16. Log of X-ray observations of 1E 2259+586 following the 2012 April outburst and up to the return to quiescence. The outburst onset occurred on MJD 56 038.34564479 (Foley et al. 2012). One *Chandra* observation was performed with the HRC-I (obs. ID 15265), and was not included in our analysis. Part of these observations were already analysed by Archibald et al. (2013).

Instrument	Mode	Obs. ID	Mid point of observation (MJD)	Time since outburst onset (d)	Exposure (ks)	Source net count rate (counts s ⁻¹)
<i>Swift</i> XRT	WT	00032035021	56 045.45	7.10	3.9	1.74 ± 0.02
<i>Swift</i> XRT	WT	00032035022	56 049.06	10.71	6.6	1.68 ± 0.02
<i>Swift</i> XRT	WT	00032035023	56 054.41	16.07	3.9	1.65 ± 0.02
<i>Swift</i> XRT	WT	00032035026	56 075.37	37.03	3.9	1.15 ± 0.02
<i>Swift</i> XRT	WT	00032035029	56 096.55	58.20	1.1	1.47 ± 0.04
<i>Swift</i> XRT	WT	00032035033	56 124.02	85.68	0.9	0.99 ± 0.03
<i>Swift</i> XRT	WT	00032035036	56 161.80	123.46	1.9	1.44 ± 0.03
<i>Swift</i> XRT	WT	00032035037	56 166.77	128.43	1.0	1.38 ± 0.04
<i>Swift</i> XRT	WT	00032035040	56 208.62	170.28	2.9	0.86 ± 0.02
<i>Swift</i> XRT	WT	00032035041	56 215.64	177.30	2.9	1.31 ± 0.02
<i>Swift</i> XRT	WT	00032035042	56 222.54	184.20	2.7	1.21 ± 0.02
<i>Swift</i> XRT	WT	00032035046	56 246.12	207.77	1.4	1.46 ± 0.03
<i>Swift</i> XRT	WT	00032035049	56 264.91	226.56	3.3	1.34 ± 0.02
<i>Swift</i> XRT	WT	00032035051	56 274.47	236.12	2.8	1.42 ± 0.02
<i>Swift</i> XRT	WT	00032035052	56 292.33	253.98	3.2	1.13 ± 0.02
<i>Swift</i> XRT	WT	00032035055	56 355.68	317.33	3.3	0.66 ± 0.01
<i>Swift</i> XRT	WT	00032035056	56 376.48	338.13	2.9	1.31 ± 0.02
<i>Swift</i> XRT	WT	00032035057	56 397.81	359.47	3.4	1.24 ± 0.02
<i>Swift</i> XRT	WT	00032035058	56 418.11	379.77	3.7	1.30 ± 0.02
<i>Swift</i> XRT	WT	00032035061	56 481.50	443.16	3.2	1.27 ± 0.02
<i>Swift</i> XRT	WT	00032035062	56 502.49	464.15	3.5	1.28 ± 0.02
<i>Swift</i> XRT	WT	00032035065	56 565.61	527.27	1.6	0.94 ± 0.02
<i>Swift</i> XRT	WT	00032035069	56 632.89	594.55	1.5	1.38 ± 0.03
<i>Swift</i> XRT	WT	00032035072	56 692.59	654.24	3.2	1.17 ± 0.02
<i>Swift</i> XRT	WT	00032035073	56 712.55	674.20	3.3	1.25 ± 0.02
<i>Swift</i> XRT	WT	00032035076	56 776.29	737.95	3.4	1.18 ± 0.02
<i>Swift</i> XRT	WT	00032035077	56 797.59	759.25	2.7	1.22 ± 0.02
<i>Swift</i> XRT	WT	00032035079	56 839.51	801.16	2.9	1.11 ± 0.02
<i>Swift</i> XRT	WT	00032035083	56 902.72	864.38	3.5	1.25 ± 0.02
<i>Swift</i> XRT	WT	00032035084	56 923.61	885.26	2.0	1.24 ± 0.03
<i>Swift</i> XRT	WT	00032035087	56 965.22	926.88	3.3	1.16 ± 0.02
<i>Swift</i> XRT	WT	00032035088	56 986.31	947.97	4.0	1.07 ± 0.02
<i>Swift</i> XRT	WT	00032035089	57 007.77	969.43	2.6	1.17 ± 0.02
<i>Swift</i> XRT	WT	00032035091	57 028.59	990.25	5.5	0.97 ± 0.01
<i>Swift</i> XRT	WT	00032035092	57 049.20	1010.86	1.3	1.02 ± 0.03
<i>Swift</i> XRT	WT	00032035093	57 070.48	1032.13	3.9	1.21 ± 0.02
<i>Swift</i> XRT	WT	00032035096	57 133.39	1095.04	3.9	0.89 ± 0.02
<i>Swift</i> XRT	WT	00032035097	57 154.58	1116.23	3.3	1.15 ± 0.02
<i>Swift</i> XRT	WT	00032035101	57 196.43	1158.09	1.2	1.10 ± 0.03
<i>Swift</i> XRT	WT	00032035104	57 204.93	1166.59	0.6	1.17 ± 0.05
<i>Swift</i> XRT	WT	00032035107	57 260.71	1222.37	3.8	0.96 ± 0.02
<i>Swift</i> XRT	WT	00032035108	57 286.61	1248.26	3.5	0.97 ± 0.02
<i>Swift</i> XRT	WT	00032035114	57 343.45	1305.11	3.2	1.31 ± 0.02

Table A17. Log of *Chandra* observations of SGR 1745–2900 following the 2013 April outburst. The outburst onset occurred on MJD 56 407.80237269 (Barthelmy et al. 2013). All reported count rates are not corrected for pile-up. Part of these observations were already analysed by Rea et al. (2013b) and Coti Zelati et al. (2015a, 2017).

Instrument	Mode	Obs. ID	Mid point of observation (MJD)	Time since outburst onset (d)	Exposure (ks)	Source net count rate (counts s ⁻¹)
<i>Chandra/HRC -S</i>	TE	14701	56 411.70	3.90	9.7	0.081 ± 0.003
<i>Chandra ACIS-S</i>	TE	14702	56 424.55	16.75	13.7	0.545 ± 0.006
<i>Chandra/HETG</i>	TE	15040	56 437.63	29.83	23.8	0.150 ± 0.003
<i>Chandra ACIS-S</i>	TE	14703	56 447.48	39.68	16.8	0.455 ± 0.005
<i>Chandra/HETG</i>	TE	15651	56 448.99	41.19	13.8	0.141 ± 0.003
<i>Chandra/HETG</i>	TE	15654	56 452.25	44.45	9.0	0.128 ± 0.004
<i>Chandra ACIS-S</i>	TE	14946	56 475.41	67.61	18.2	0.392 ± 0.005
<i>Chandra ACIS-S</i>	TE	15041	56 500.36	92.56	45.4	0.346 ± 0.003
<i>Chandra ACIS-S</i>	TE	15042	56 516.25	108.45	45.7	0.317 ± 0.003
<i>Chandra ACIS-S</i>	TE	14945	56 535.55	127.75	18.2	0.290 ± 0.004
<i>Chandra ACIS-S</i>	TE	15043	56 549.30	141.50	45.4	0.275 ± 0.002
<i>Chandra ACIS-S</i>	TE	14944	56 555.42	147.62	18.2	0.273 ± 0.004
<i>Chandra ACIS-S</i>	TE	15044	56 570.01	162.21	42.7	0.255 ± 0.002
<i>Chandra ACIS-S</i>	TE	14943	56 582.78	174.98	18.2	0.246 ± 0.004
<i>Chandra ACIS-S</i>	TE	14704	56 588.62	180.82	36.3	0.240 ± 0.003
<i>Chandra ACIS-S</i>	TE	15045	56 593.91	186.11	45.4	0.234 ± 0.002
<i>Chandra ACIS-S</i>	TE	16508	56 709.77	301.97	43.4	0.156 ± 0.002
<i>Chandra ACIS-S</i>	TE	16211	56 730.71	322.91	41.8	0.149 ± 0.002
<i>Chandra ACIS-S</i>	TE	16212	56 751.40	343.60	45.4	0.135 ± 0.002
<i>Chandra ACIS-S</i>	TE	16213	56 775.41	367.61	45.0	0.128 ± 0.002
<i>Chandra ACIS-S</i>	TE	16214	56 797.31	389.51	45.4	0.118 ± 0.002
<i>Chandra ACIS-S</i>	TE	16210	56 811.24	403.44	17.0	0.110 ± 0.003
<i>Chandra ACIS-S</i>	TE	16597	56 842.98	435.18	16.5	0.097 ± 0.002
<i>Chandra ACIS-S</i>	TE	16215	56 855.22	447.42	41.5	0.090 ± 0.001
<i>Chandra ACIS-S</i>	TE	16216	56 871.43	463.63	42.7	0.085 ± 0.001
<i>Chandra ACIS-S</i>	TE	16217	56 899.43	491.63	34.5	0.079 ± 0.002
<i>Chandra ACIS-S</i>	TE	16218	56 950.59	542.79	36.3	0.071 ± 0.001
<i>Chandra ACIS-S</i>	TE	16963	57 066.18	658.38	22.7	0.056 ± 0.002
<i>Chandra ACIS-S</i>	TE	16966	57 156.53	748.72	22.7	0.045 ± 0.001
<i>Chandra ACIS-S</i>	TE	16965	57 251.60	843.80	22.7	0.035 ± 0.001
<i>Chandra ACIS-S</i>	TE	16964	57 316.41	908.60	22.6	0.026 ± 0.001
<i>Chandra ACIS-S</i>	TE	18055	57 431.53	1023.73	22.7	0.0133 ± 0.0008
<i>Chandra ACIS-S</i>	TE	18056	57 432.76	1024.96	21.8	0.0146 ± 0.0009
<i>Chandra ACIS-S</i>	TE	18731	57 582.27	1174.47	78.4	0.0102 ± 0.0004
<i>Chandra ACIS-S</i>	TE	18732	57 588.00	1180.20	76.6	0.0118 ± 0.0004
<i>Chandra ACIS-S</i>	TE	18057	57 669.95	1262.15	22.7	0.0130 ± 0.0008
<i>Chandra ACIS-S</i>	TE	18058	57 675.61	1267.80	22.7	0.0135 ± 0.00081

Table A18. Log of all X-ray observations of SGR 1935+2154 following the 2014 July outburst. The outburst onset occurred on MJD 56 843.39777778 (Stamatikos et al. 2014). Part of these observations were already analysed by Israel et al. (2016).

Instrument	Mode	Obs. ID	Mid point of observation (MJD)	Time since outburst onset (d)	Exposure (ks)	Source net count rate (counts s ⁻¹)
<i>Swift</i> XRT	PC	00603488000	56 843.44	0.04	3.4	0.033 ± 0.003
<i>Swift</i> XRT	PC	00603488001	56 844.72	0.32	9.9	0.027 ± 0.002
<i>Swift</i> XRT	PC	00603488003	56 845.36	1.96	3.9	0.019 ± 0.002
<i>Swift</i> XRT	PC	00603488006	56 846.77	3.37	3.7	0.028 ± 0.003
<i>Swift</i> XRT	PC	00603488007	56 847.67	4.27	3.6	0.018 ± 0.002
<i>Swift</i> XRT	PC	00603488009	56 851.39	7.99	3.0	0.025 ± 0.003
<i>Swift</i> XRT	PC	00603488008	56 851.62	8.23	5.3	0.022 ± 0.002
<i>Chandra</i> ACIS-S	TE	15874	56 853.66	10.26	9.1	0.110 ± 0.003
<i>Swift</i> XRT	PC	00603488010	56 854.51	11.11	7.1	0.024 ± 0.002
<i>Swift</i> XRT	PC	00603488011	56 858.54	15.14	2.9	0.019 ± 0.003
<i>Chandra</i> ACIS-S	CC	15875	56 866.48	23.08	75.1	0.115 ± 0.001
<i>Swift</i> XRT	PC	00033349001	56 869.76	26.36	2.1	0.019 ± 0.003
<i>Swift</i> XRT	PC	00033349002	56 876.70	33.30	2.2	0.022 ± 0.003
<i>Swift</i> XRT	PC	00033349003	56 883.75	40.35	1.5	0.023 ± 0.004
<i>Swift</i> XRT	PC	00033349004	56 890.41	47.01	1.7	0.019 ± 0.003
<i>Swift</i> XRT	PC	00033349005	56 894.65	51.25	3.7	0.020 ± 0.002
<i>Swift</i> XRT	PC	00033349006	56 897.55	54.15	1.7	0.022 ± 0.004
<i>Chandra</i> ACIS-S	CC	17314	56 900.21	56.81	29.0	0.107 ± 0.002
<i>Swift</i> XRT	PC	00033349007	56 904.79	61.39	1.1	0.016 ± 0.004
<i>Swift</i> XRT	PC	00033349008	56 906.51	63.11	1.5	0.022 ± 0.004
<i>Swift</i> XRT	PC	00033349009	56 911.27	67.88	1.5	0.023 ± 0.004
<i>Swift</i> XRT	PC	00033349010	56 914.31	70.91	2.4	0.024 ± 0.003
<i>Swift</i> XRT	PC	00033349011	56 918.57	75.17	1.4	0.019 ± 0.004
<i>Swift</i> XRT	PC	00033349012	56 924.50	81.10	2.3	0.019 ± 0.003
<i>XMM–Newton</i> EPN	FF	0722412501	56 927.06	83.66	16.9	0.190 ± 0.003
<i>XMM–Newton</i> EPN	FF	0722412601	56 928.32	84.92	17.8	0.189 ± 0.003
<i>XMM–Newton</i> EPN	FF	0722412701	56 934.36	90.96	16.1	0.197 ± 0.004
<i>XMM–Newton</i> EPN	FF	0722412801	56 946.17	102.77	8.6	0.194 ± 0.005
<i>XMM–Newton</i> EPN	FF	0722412901	56 954.19	110.79	6.4	0.201 ± 0.006
<i>XMM–Newton</i> EPN	FF	0722413001	56 958.03	114.63	11.2	0.189 ± 0.004
<i>XMM–Newton</i> EPN	FF	0748390801	56 976.27	132.87	9.5	0.194 ± 0.005
<i>Swift</i> XRT	PC	00632158000	57 075.59	232.19	7.3	0.039 ± 0.002
<i>Swift</i> XRT	PC	00632158001	57 075.84	232.44	1.8	0.042 ± 0.005
<i>Swift</i> XRT	PC	00632158002	57 076.59	233.19	5.9	0.028 ± 0.002
<i>Swift</i> XRT	PC	00033349014	57 078.48	235.08	3.1	0.030 ± 0.003
<i>Swift</i> XRT	PC	00033349015	57 080.35	236.95	5.9	0.022 ± 0.002
<i>Swift</i> XRT	PC	00033349016	57 085.51	242.11	3.9	0.025 ± 0.003
<i>Swift</i> XRT	PC	00033349017	57 092.69	249.29	3.9	0.023 ± 0.002
<i>XMM–Newton</i> EPN	FF	0764820101	57 106.59	263.19	26.5	0.250 ± 0.003
<i>Swift</i> XRT	PC	00033349020	57 127.83	284.43	3.0	0.014 ± 0.002
<i>Swift</i> XRT	PC	00033349023	57 134.62	291.22	1.4	0.029 ± 0.005
<i>Swift</i> XRT	PC	00033349024	57 221.00	377.60	2.0	0.025 ± 0.004
<i>XMM–Newton</i> EPN	FF	0764820201	57 303.04	459.65	11.4	0.207 ± 0.004
<i>Swift</i> XRT	PC	00033349025	57 377.77	534.37	3.9	0.017 ± 0.002
<i>Swift</i> XRT	PC	00686761000	57 526.42	683.02	1.6	0.058 ± 0.006
<i>Swift</i> XRT	PC	00033349026	57 527.81	684.41	2.9	0.020 ± 0.003
<i>Swift</i> XRT	PC	00687123000	57 529.84	686.45	1.2	0.026 ± 0.005
<i>Swift</i> XRT	PC	00033349027	57 534.44	691.04	2.3	0.017 ± 0.003
<i>Swift</i> XRT	PC	00033349028	57 539.99	696.51	2.8	0.015 ± 0.002
<i>Swift</i> XRT	PC	00033349030	57 548.89	705.49	1.7	0.014 ± 0.003
<i>Swift</i> XRT	PC	00033349031	57 554.23	710.83	2.6	0.020 ± 0.003
<i>Swift</i> XRT	PC	00033349032	57 561.42	718.02	1.6	0.020 ± 0.004
<i>Swift</i> XRT	PC	00033349033	57 567.59	724.19	2.0	0.023 ± 0.003
<i>Swift</i> XRT	PC	00033349034	57 569.82	726.42	2.4	0.019 ± 0.003
<i>Swift</i> XRT	PC	00033349035	57 576.88	733.48	2.8	0.020 ± 0.003
<i>Swift</i> XRT	PC	00033349036	57 586.36	742.96	2.5	0.020 ± 0.003
<i>Swift</i> XRT	PC	00033349037	57 597.51	754.11	2.8	0.024 ± 0.003

Table A19. Log of the X-ray observations of 1E 1048.1–5937 following the 2016 July outburst. No burst signalling the outburst onset was detected in this case. The outburst onset is thus considered to be occurred on \sim MJD 57 592, when an increase in the X-ray flux was measured (the previous *Swift* observation was carried out on MJD 57 588; Archibald et al. 2016b). The source is currently being regularly monitored by *Swift*.

Instrument	Mode	Obs. ID	Mid point of observation (MJD)	Time since outburst onset (d)	Exposure (ks)	Source net count rate (counts s $^{-1}$)
<i>Swift</i> XRT	WT	00032923248	57 592.49	0.49	1.2	0.85 ± 0.03
<i>Swift</i> XRT	WT	00032923249	57 598.47	6.47	1.4	0.95 ± 0.03
<i>Swift</i> XRT	WT	00032923250	57 598.80	6.80	1.1	0.81 ± 0.03
<i>Swift</i> XRT	WT	00032923251	57 605.97	13.97	0.3	0.55 ± 0.04
<i>Swift</i> XRT	WT	00032923252	57 607.53	15.53	0.9	0.78 ± 0.03
<i>Swift</i> XRT	WT	00032923253	57 608.27	16.27	0.6	0.56 ± 0.03
<i>Swift</i> XRT	WT	00032923254	57 608.38	16.38	1.0	0.65 ± 0.03
<i>Swift</i> XRT	WT	00032923255	57 612.02	20.02	0.6	0.69 ± 0.03
<i>Swift</i> XRT	WT	00030912012	57 612.65	20.65	1.4	0.87 ± 0.02
<i>Swift</i> XRT	WT	00030912013	57 613.61	21.61	1.4	0.47 ± 0.02
<i>Swift</i> XRT	WT	00030912016	57 627.91	35.91	0.1	0.59 ± 0.07
<i>Swift</i> XRT	WT	00030912019	57 628.11	36.11	0.9	0.51 ± 0.02
<i>Swift</i> XRT	WT	00030912017	57 629.45	37.45	1.2	0.63 ± 0.02
<i>Swift</i> XRT	WT	00030912020	57 633.13	41.13	1.5	0.47 ± 0.02
<i>Swift</i> XRT	WT	00030912022	57 634.82	42.82	0.6	0.67 ± 0.03
<i>Swift</i> XRT	WT	00030912025	57 640.20	48.20	1.6	0.65 ± 0.21
<i>Swift</i> XRT	WT	00030912023	57 640.50	48.50	1.4	0.51 ± 0.02
<i>Swift</i> XRT	WT	00030912024	57 641.40	49.40	1.5	0.54 ± 0.02
<i>Swift</i> XRT	WT	00030912026	57 654.15	62.15	1.5	0.58 ± 0.02
<i>Swift</i> XRT	WT	00030912027	57 654.39	62.39	1.3	0.53 ± 0.02
<i>Swift</i> XRT	WT	00030912028	57 655.15	63.15	1.4	0.52 ± 0.02
<i>Swift</i> XRT	WT	00030912029	57 667.27	75.27	1.5	0.49 ± 0.02
<i>Swift</i> XRT	WT	00030912030	57 667.41	75.41	1.1	0.44 ± 0.02
<i>Swift</i> XRT	WT	00030912031	57 668.20	76.20	1.4	0.52 ± 0.02
<i>Swift</i> XRT	WT	00030912032	57 677.45	85.45	1.1	0.52 ± 0.02
<i>Swift</i> XRT	WT	00030912033	57 677.85	85.85	1.6	0.53 ± 0.02
<i>Swift</i> XRT	WT	00030912035	57 687.12	95.12	1.4	0.53 ± 0.02
<i>Swift</i> XRT	WT	00030912036	57 687.58	95.58	1.5	0.42 ± 0.02
<i>Swift</i> XRT	WT	00030912037	57 688.17	96.17	1.5	0.52 ± 0.02
<i>Swift</i> XRT	WT	00030912038	57 697.08	105.08	1.6	0.55 ± 0.02
<i>Swift</i> XRT	WT	00030912040	57 698.84	106.84	1.4	0.35 ± 0.02
<i>Swift</i> XRT	WT	00030912041	57 707.35	115.35	1.0	0.38 ± 0.02
<i>Swift</i> XRT	WT	00030912042	57 707.60	115.60	1.5	0.53 ± 0.02
<i>Swift</i> XRT	WT	00030912043	57 708.80	116.80	1.4	0.33 ± 0.02
<i>Swift</i> XRT	WT	00030912044	57 717.34	125.34	1.4	0.39 ± 0.02
<i>Swift</i> XRT	WT	00030912045	57 717.73	125.73	1.5	0.48 ± 0.02
<i>Swift</i> XRT	WT	00030912046	57 718.87	126.87	1.4	0.43 ± 0.02
<i>Swift</i> XRT	WT	00030912047	57 727.02	135.02	1.4	0.39 ± 0.02
<i>Swift</i> XRT	WT	00030912048	57 727.55	135.55	1.5	0.42 ± 0.02
<i>Swift</i> XRT	WT	00030912049	57 728.45	136.45	1.5	0.42 ± 0.02
<i>Swift</i> XRT	WT	00030912050	57 737.22	145.22	1.1	0.49 ± 0.02
<i>Swift</i> XRT	WT	00030912051	57 737.45	145.45	1.3	0.43 ± 0.02
<i>Swift</i> XRT	WT	00030912052	57 738.08	146.08	1.5	0.51 ± 0.02
<i>Swift</i> XRT	WT	00030912053	57 747.15	155.15	1.4	0.46 ± 0.02
<i>Swift</i> XRT	WT	00030912054	57 747.61	155.61	1.6	0.42 ± 0.02
<i>Swift</i> XRT	WT	00030912055	57 748.77	156.77	1.5	0.27 ± 0.01
<i>Swift</i> XRT	WT	00030912057	57 758.77	166.77	1.4	0.41 ± 0.02
<i>Swift</i> XRT	WT	00030912058	57 759.49	167.49	1.3	0.39 ± 0.02
<i>Swift</i> XRT	WT	00030912059	57 778.18	186.18	1.5	0.46 ± 0.02
<i>Swift</i> XRT	WT	00030912060	57 778.57	186.57	1.4	0.45 ± 0.02
<i>Swift</i> XRT	WT	00030912061	57 779.68	187.68	1.4	0.111 ± 0.009
<i>Swift</i> XRT	WT	00030912062	57 785.06	193.06	1.6	0.40 ± 0.02
<i>Swift</i> XRT	WT	00030912063	57 785.89	193.89	1.4	0.40 ± 0.02
<i>Swift</i> XRT	WT	00030912064	57 786.09	194.09	1.5	0.41 ± 0.02
<i>Swift</i> XRT	WT	00030912065	57 793.04	201.04	0.3	0.46 ± 0.04
<i>Swift</i> XRT	WT	00030912066	57 794.92	202.92	1.5	0.39 ± 0.02
<i>Swift</i> XRT	WT	00030912067	57 796.87	204.87	0.6	0.36 ± 0.02
<i>Swift</i> XRT	WT	00030912068	57 797.82	205.82	1.1	0.38 ± 0.02
<i>Swift</i> XRT	WT	00030912069	57 803.21	211.21	1.4	0.38 ± 0.02
<i>Swift</i> XRT	WT	00030912070	57 803.86	211.86	1.5	0.43 ± 0.02

Table A20. Log of all X-ray observations of PSR J1119–6127 following the 2016 July outburst. The outburst onset occurred on MJD 57 597.06100694 (Kennea et al. 2016). Part of these observations were already analysed by Archibald et al. (2016a).

Instrument	Mode	Obs. ID	Mid point of observation (MJD)	Time since outburst onset (d)	Exposure (ks)	Source net count rate (counts s ⁻¹)
<i>Swift</i> XRT	PC	00706396000	57 597.08	0.01	2.2	0.544 ± 0.02
<i>Swift</i> XRT	WT	00034632001	57 597.93	0.87	9.6	0.510 ± 0.008
<i>Swift</i> XRT	WT	00034632002	57 601.02	3.95	4.8	0.53 ± 0.01
<i>Swift</i> XRT	PC	00034632003	57 603.52	6.46	3.0	0.202 ± 0.008
<i>Swift</i> XRT	PC	00034632005	57 606.54	9.48	3.0	0.212 ± 0.008
<i>Swift</i> XRT	WT	00034632007	57 609.56	12.50	5.5	0.49 ± 0.01
<i>Swift</i> XRT	WT	00034632008	57 610.26	13.20	1.3	0.39 ± 0.02
<i>Swift</i> XRT	PC	00034632009	57 612.32	15.25	2.3	0.179 ± 0.009
<i>Swift</i> XRT	WT	00034632010	57 627.32	30.26	3.0	0.40 ± 0.01
<i>Swift</i> XRT	WT	00034632011	57 630.41	33.34	3.2	0.40 ± 0.01
<i>Swift</i> XRT	WT	00034632013	57 637.45	40.38	2.1	0.30 ± 0.01
<i>Swift</i> XRT	WT	00034632014	57 641.73	44.66	2.4	0.28 ± 0.02
<i>Swift</i> XRT	WT	00034632015	57 647.07	50.01	2.1	0.33 ± 0.01
<i>Swift</i> XRT	WT	00034632016	57 647.42	50.36	1.7	0.23 ± 0.01
<i>Swift</i> XRT	WT	00034632017	57 648.07	51.01	1.9	0.40 ± 0.02
<i>Swift</i> XRT	WT	00034632018	57 657.10	60.04	1.9	0.36 ± 0.01
<i>Swift</i> XRT	WT	00034632019	57 657.70	60.63	1.9	0.31 ± 0.01
<i>Swift</i> XRT	WT	00034632020	57 658.05	60.98	2.1	0.34 ± 0.01
<i>Swift</i> XRT	WT	00034632022	57 667.67	70.61	1.6	0.25 ± 0.01
<i>Swift</i> XRT	WT	00034632023	57 668.37	71.30	2.0	0.24 ± 0.01
<i>Swift</i> XRT	WT	00034632024	57 679.05	81.98	2.0	0.17 ± 0.01
<i>Swift</i> XRT	WT	00034632025	57 679.62	82.55	2.0	0.31 ± 0.01
<i>Swift</i> XRT	WT	00034632026	57 680.17	83.11	1.8	0.19 ± 0.01
<i>Swift</i> XRT	WT	00034632027	57 687.21	90.15	1.9	0.22 ± 0.01
<i>Swift</i> XRT	WT	00034632028	57 687.42	90.36	1.9	0.34 ± 0.01
<i>Swift</i> XRT	WT	00034632029	57 688.21	91.14	1.7	0.22 ± 0.01
<i>Swift</i> XRT	WT	00034632030	57 693.19	96.12	2.1	0.23 ± 0.01
<i>Swift</i> XRT	WT	00034632037	57 707.27	110.21	2.5	0.18 ± 0.01
<i>Swift</i> XRT	WT	00034632039	57 708.31	111.25	2.0	0.18 ± 0.01
<i>Swift</i> XRT	WT	00034632040	57 709.87	112.80	2.1	0.16 ± 0.01
<i>Swift</i> XRT	WT	00034632041	57 714.19	117.12	1.9	0.22 ± 0.01
<i>Swift</i> XRT	WT	00034632042	57 714.59	117.52	1.9	0.19 ± 0.01
<i>Swift</i> XRT	WT	00034632043	57 715.18	118.12	2.1	0.146 ± 0.009
<i>Swift</i> XRT	WT	00034632044	57 729.22	132.16	2.6	0.175 ± 0.009
<i>Swift</i> XRT	WT	00034632045	57 729.65	132.59	5.5	0.211 ± 0.007
<i>Swift</i> XRT	WT	00034632046	57 730.14	133.08	4.9	0.142 ± 0.006

APPENDIX B: *Swift* XRT LIGHT CURVES

This section reports a series of figures showing the cooling curves for magnetar outbursts as observed by the X-ray Telescope on board *Swift* and in terms of the count rate. The 0.3–10 keV light curves were created by exploiting both PC- and WT-mode data, and using the online *Swift* XRT data products generator (http://www.swift.ac.uk/user_objects/). This tool corrects for instrumental artefacts such as pile up and bad columns on the CCD (see Evans et al. 2007, 2009 for more details).

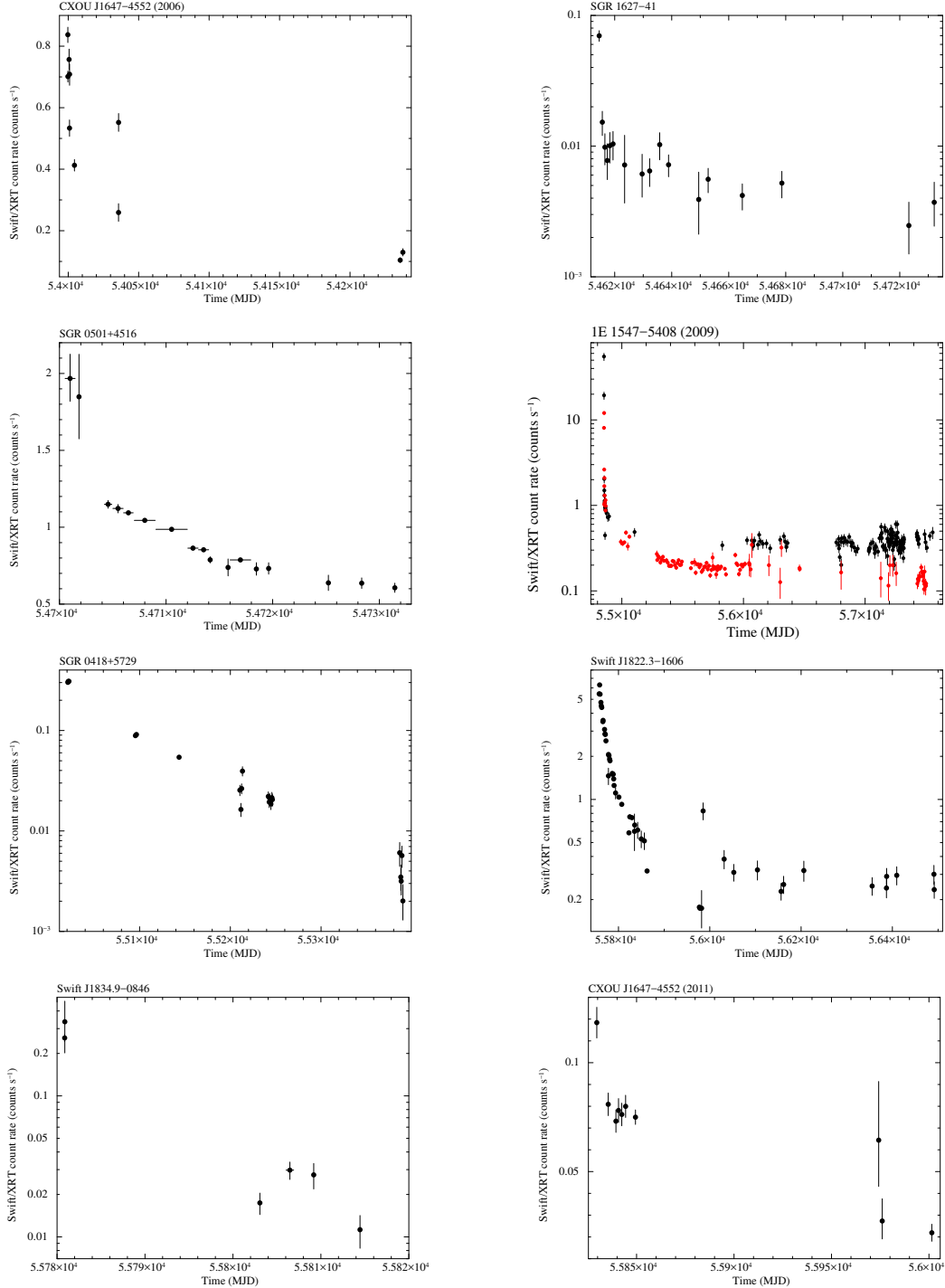


Figure B1. *Swift* XRT long-term 0.3–10 keV light curves of densely monitored magnetar outbursts, created using the online *Swift* XRT data products generator (Evans et al. 2009). In case both PC- and WT-mode data are available, black (red) dots refer to data acquired with the XRT set in WT (PC) mode.

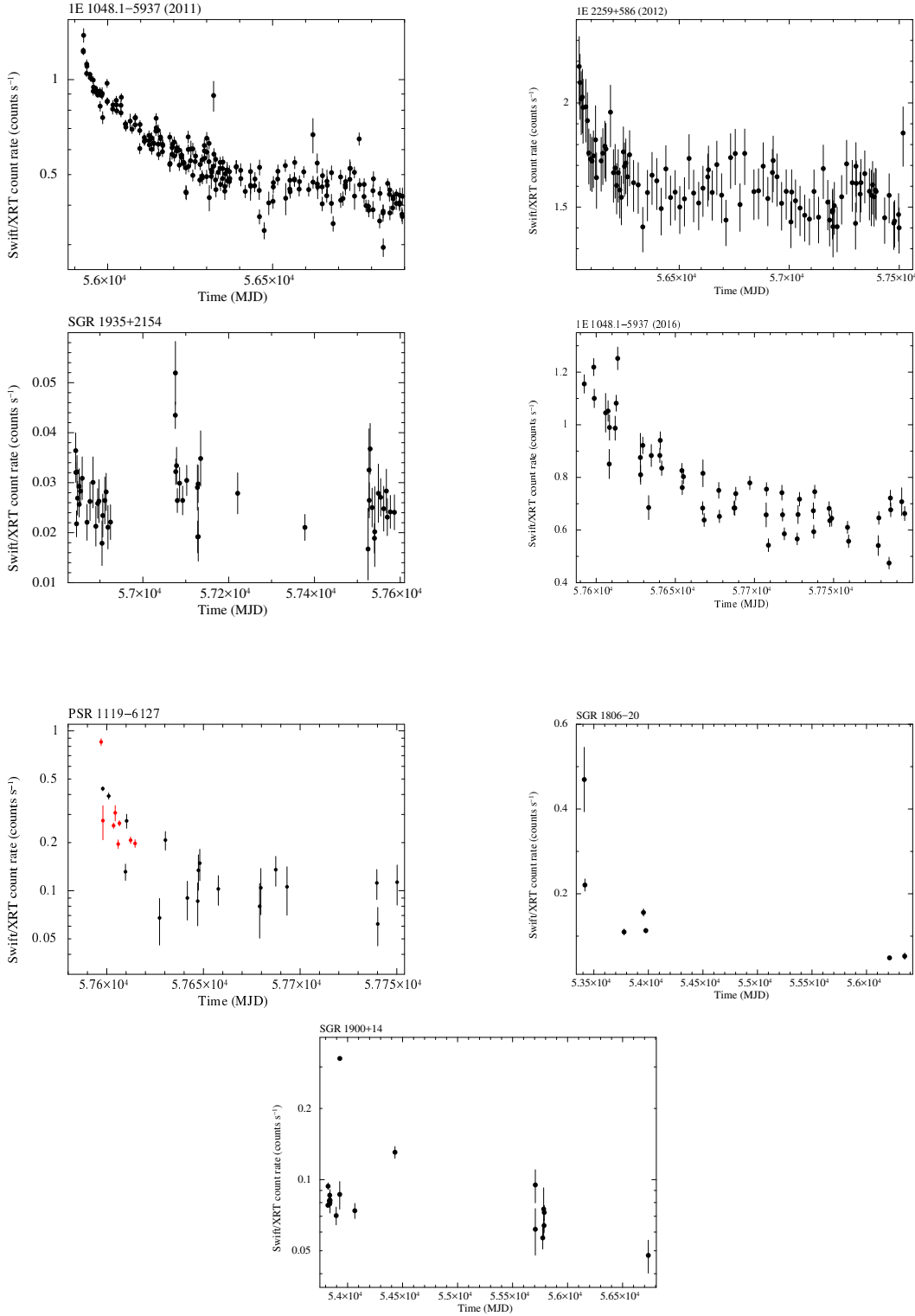


Figure B1. – continued

APPENDIX C: HIGH-STATISTICS QUALITY X-RAY SPECTRA AND FITTED MODELS

This section reports a series of figures showing several high-quality spectra and the best-fitting empirical models (see Table 1) for the outbursts that were repeatedly monitored by the *XMM-Newton* or *Chandra* observatories. In each case we plot the $E \times F(E)$ unfolded spectra and the models, to highlight the contributions of the different spectral components to the total X-ray emission (i.e. multiple blackbodies or blackbody plus power law; see the dotted lines in the figures) as a function of time. Post-fit residuals in units of standard deviations are also plotted at the bottom of each panel. In all cases, the data points were re-binned for plotting purpose, to better visualize the trend in the spectral residuals. The colours are associated with the chronological order of the observations according to the following code: black, red, green, blue, light blue, magenta, yellow, orange, yellow+green, green+cyan, blue+cyan, blue+magenta, red+magenta, dark grey, light grey.

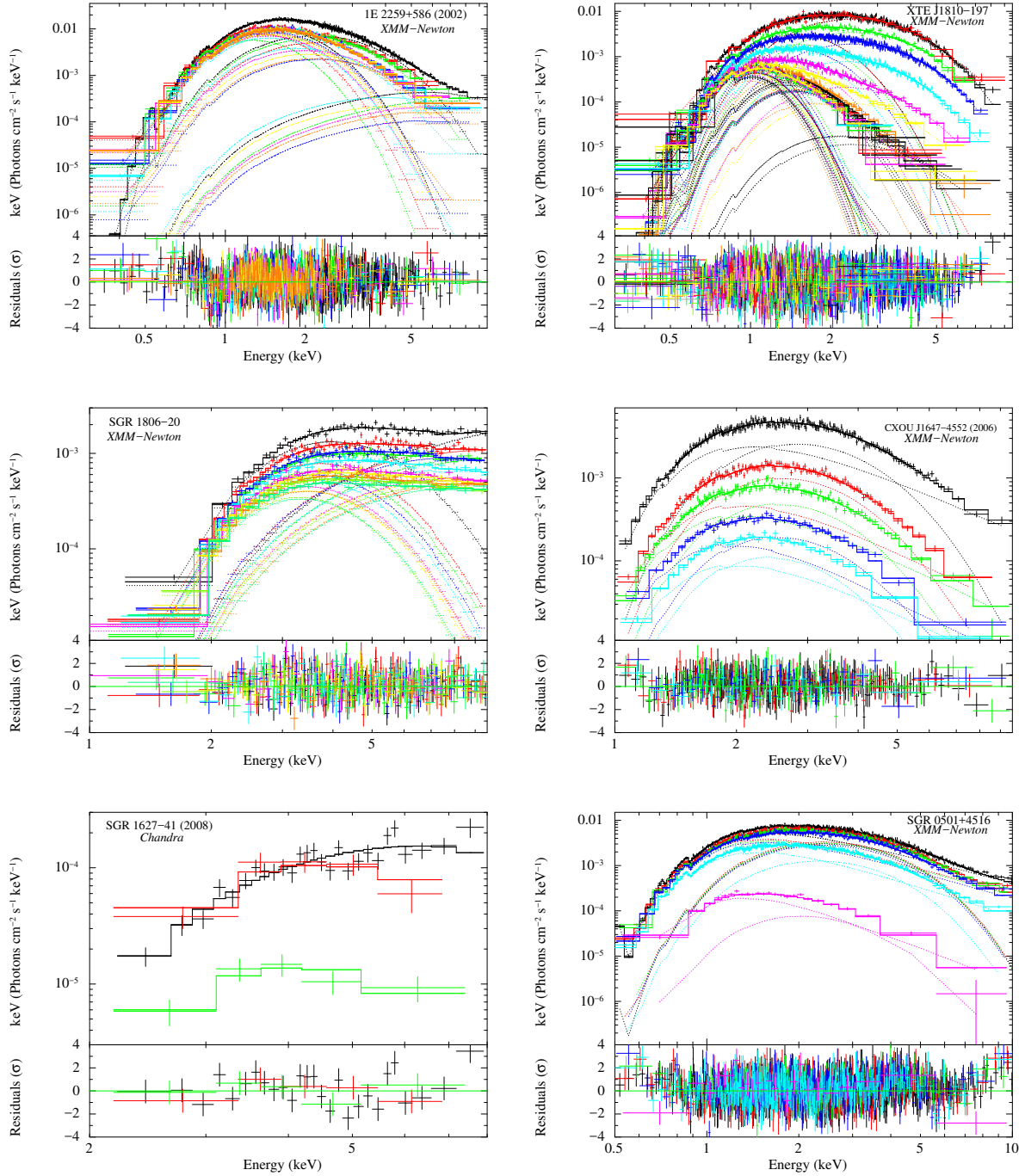


Figure C1. High quality unfolded spectra for magnetar outbursts that were repeatedly monitored with the *XMM-Newton* or *Chandra* observatories. Best-fitting models are marked by the solid lines, whereas the contributions of the different spectral components are marked by the dotted lines (see Table 1 for more details on the models employed).

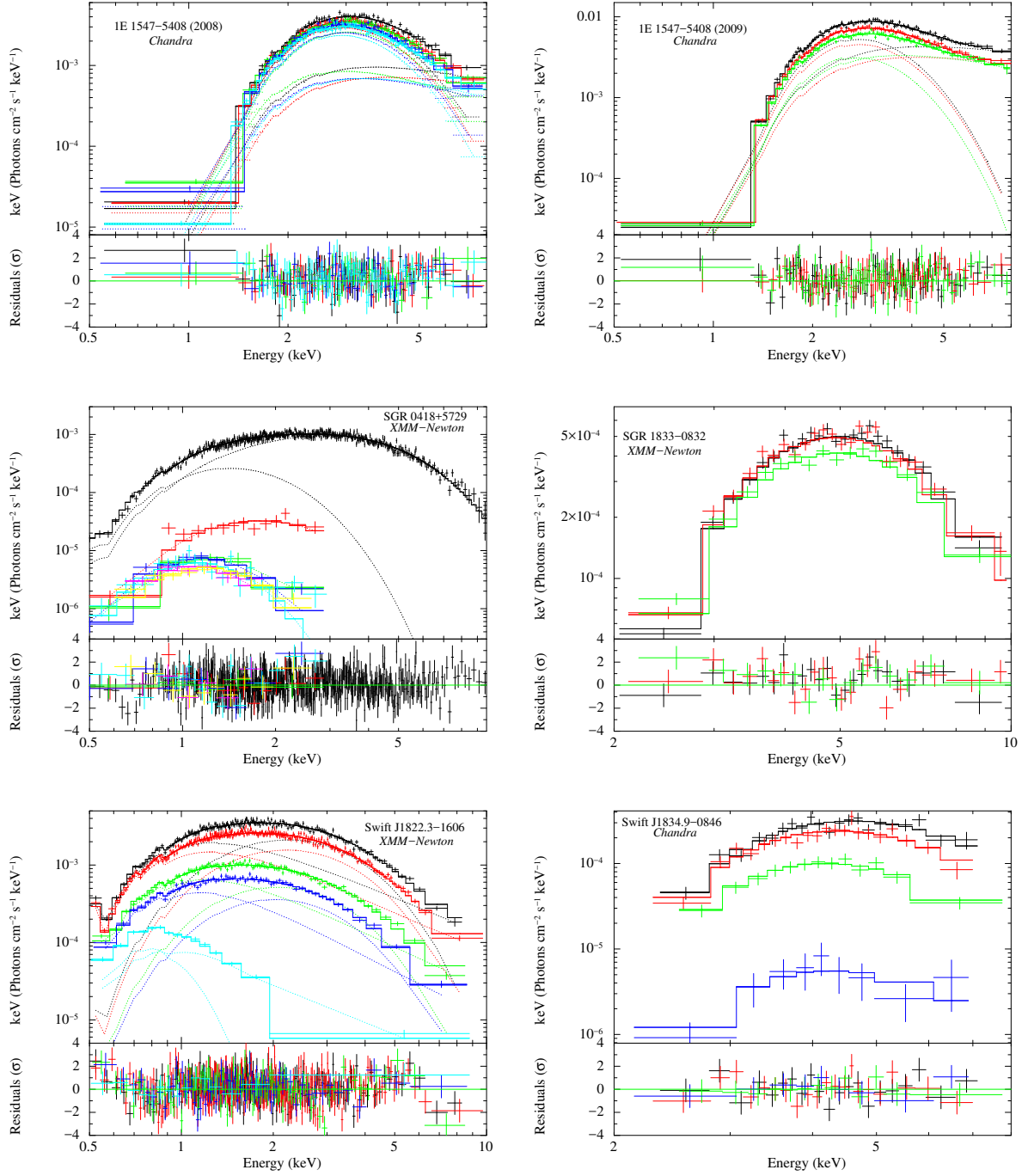
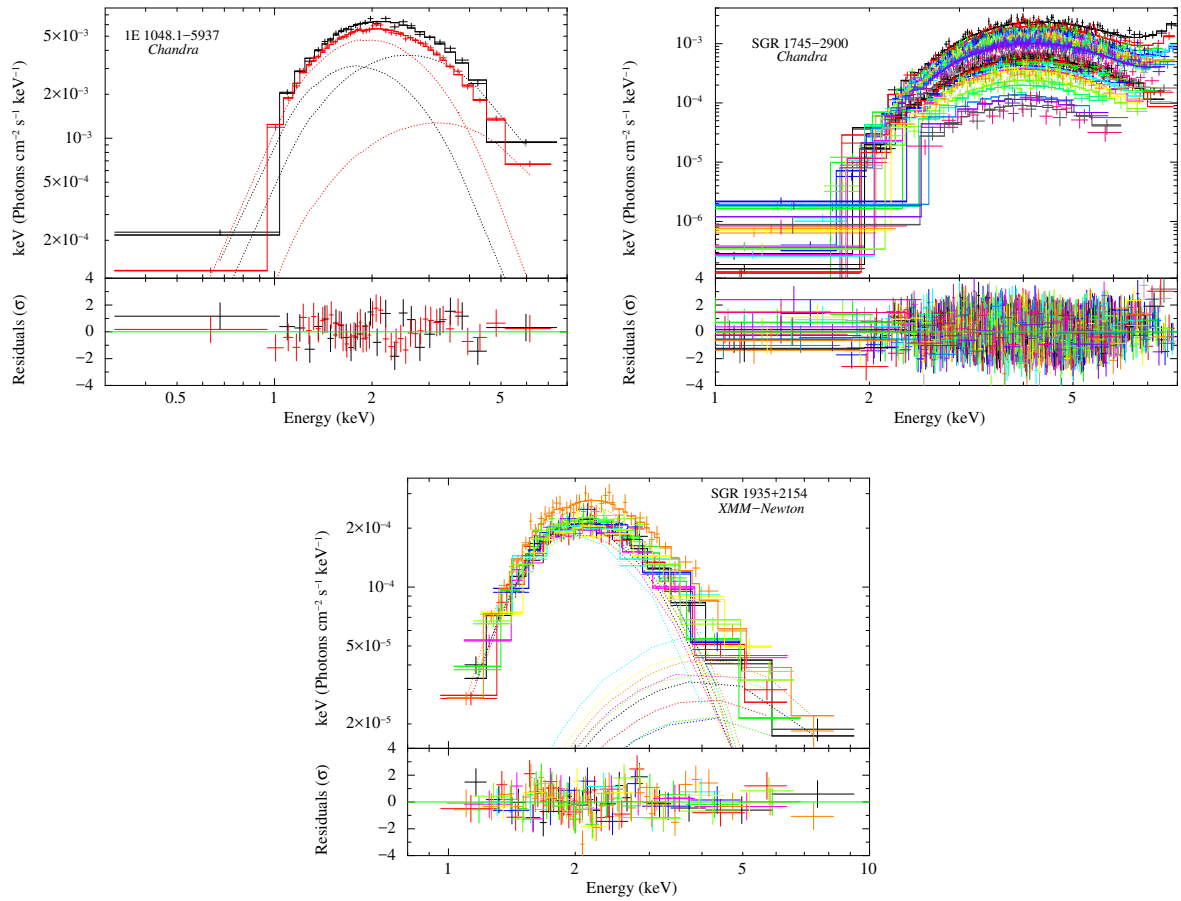


Figure C1. – continued

**Figure C1.** Continued.

APPENDIX D: OUTBURST LIGHT CURVES

This section shows the cooling curves for all magnetar outbursts re-analysed in this study.

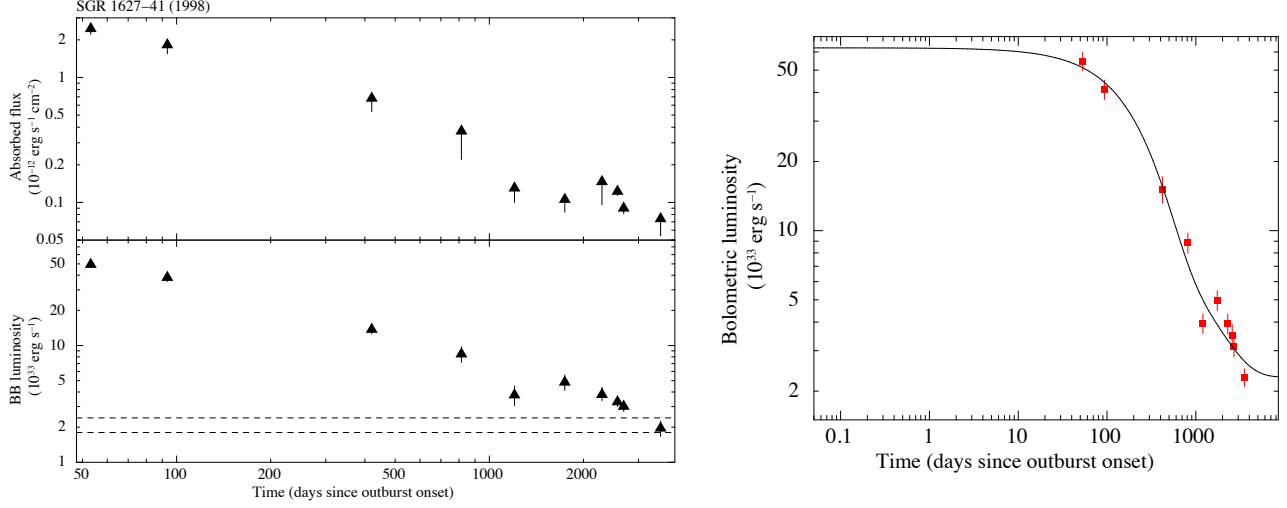


Figure D1. Left-hand panel: temporal evolution of the fluxes and luminosities for the BB model applied to the X-ray data of the 1998 outburst of SGR 1627–41. The dashed lines mark the 1σ c.l. range for the quiescent luminosity (see Table 4). A distance of 11 kpc was assumed. Right-hand panel: temporal evolution of the bolometric luminosity with the best-fitting decay model superimposed.

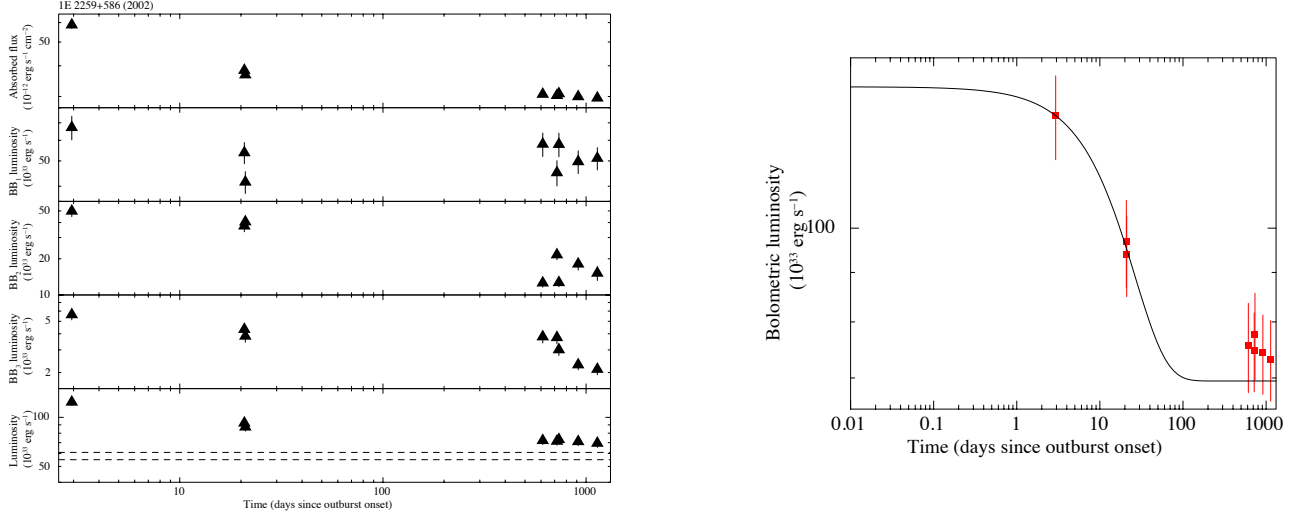


Figure D2. Left-hand panel: temporal evolution of the fluxes and luminosities for the 3BB model applied to the *XMM-Newton* data of the 2002 outburst of 1E 2259+586. The dashed lines mark the 1σ c.l. range for the quiescent luminosity (see Table 4). A distance of 3.2 kpc was assumed. Right-hand panel: temporal evolution of the bolometric luminosity with the best-fitting decay model superimposed.

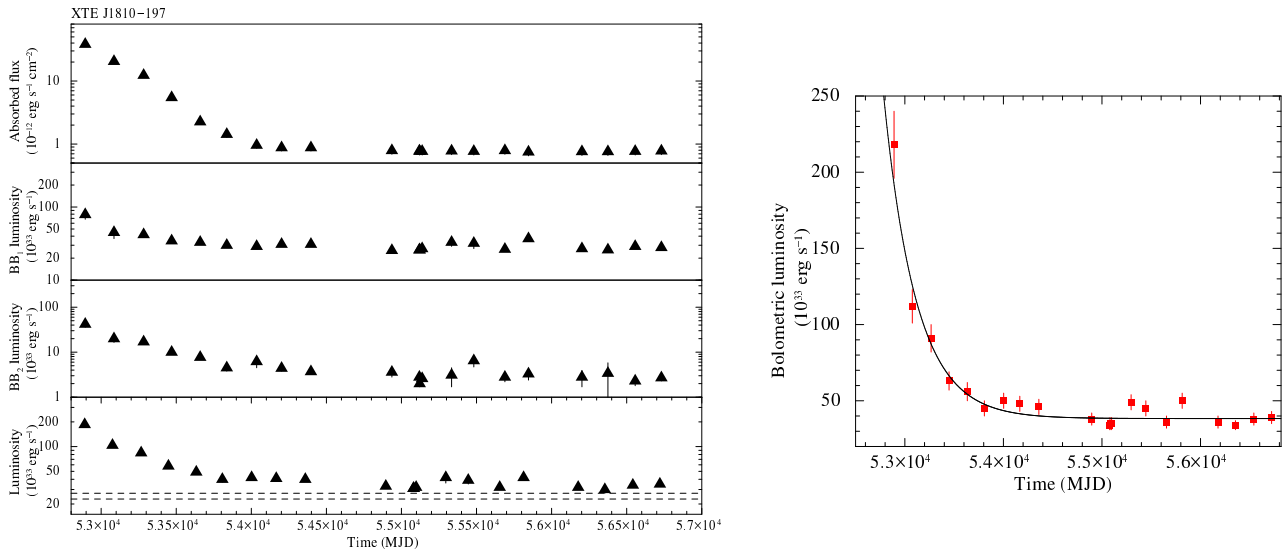


Figure D3. Left-hand panel: temporal evolution of the fluxes and luminosities of the cold and warm blackbody components for the 3BB+2BB model applied to the *XMM-Newton* data of the 2003 outburst of XTE J1810–197. The dashed lines mark the 1σ c.l. range for the quiescent luminosity (see Table 4). A distance of 3.5 kpc was assumed. Right-hand panel: temporal evolution of the bolometric luminosity with the best-fitting decay model superimposed.

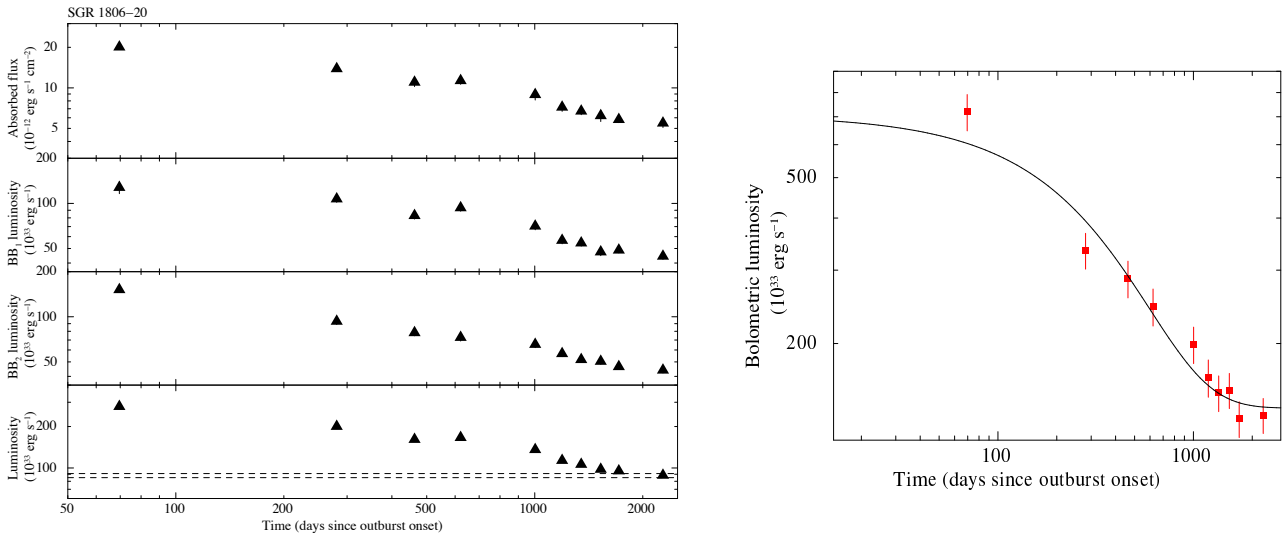


Figure D4. Left-hand panel: temporal evolution of the fluxes and luminosities for the 2BB model applied to the *XMM-Newton* data of SGR 1806–20. The dashed lines mark the 1σ c.l. range for the quiescent luminosity (see Table 4). A distance of 8.7 kpc was assumed. Right-hand panel: temporal evolution of the bolometric luminosity with the best-fitting decay model superimposed.

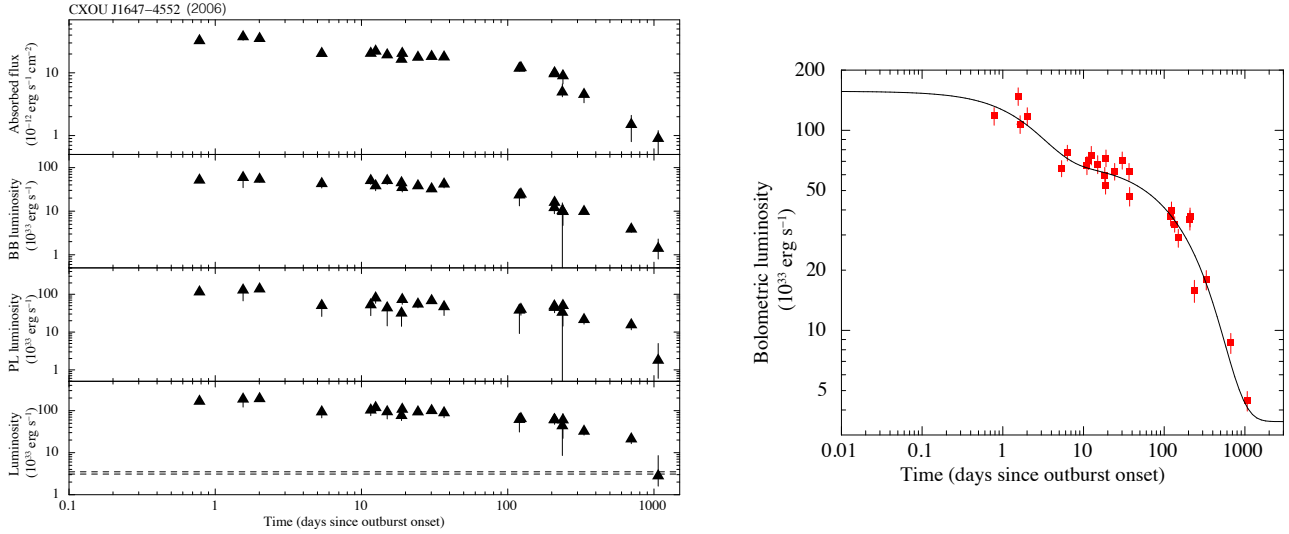


Figure D5. Left-hand panel: temporal evolution of the fluxes and luminosities for the BB+PL model applied to the X-ray data of CXOU J164710.2–455216. The dashed lines mark the 1σ c.l. range for the quiescent luminosity (see Table 4). A distance of 4 kpc was assumed. Right-hand panel: temporal evolution of the bolometric luminosity with the best-fitting decay model superimposed.

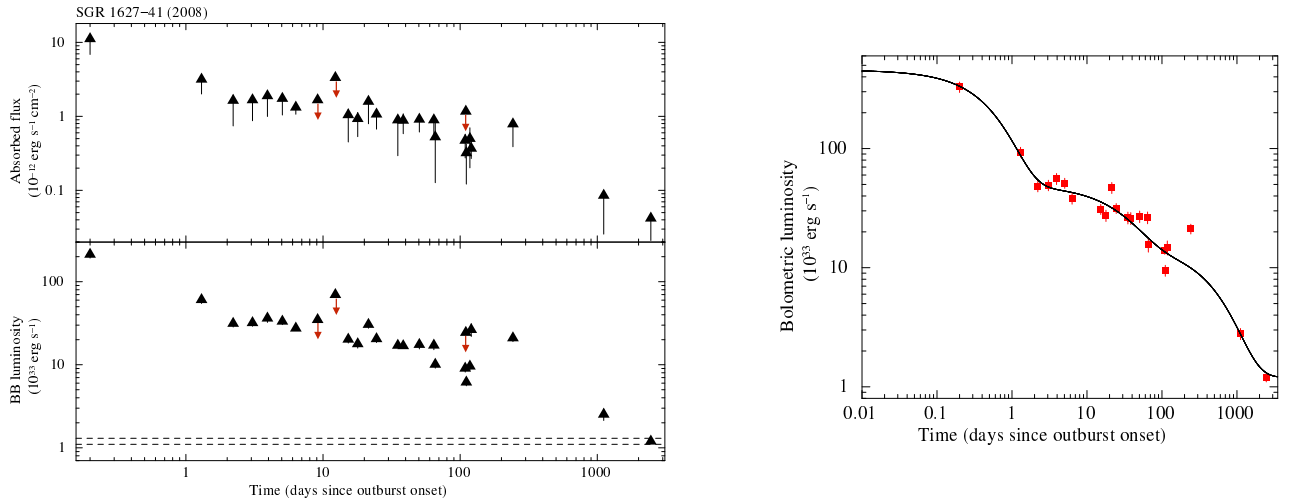


Figure D6. Left-hand panel: temporal evolution of the fluxes and luminosities for the BB model applied to the X-ray data of the 2008 outburst of SGR 1627–41. The dashed lines mark the 1σ c.l. range for the quiescent luminosity (see Table 4). The red downward arrowheads indicate the 3σ upper limits. A distance of 11 kpc was assumed. Right-hand panel: temporal evolution of the bolometric luminosity with the best-fitting decay model superimposed.

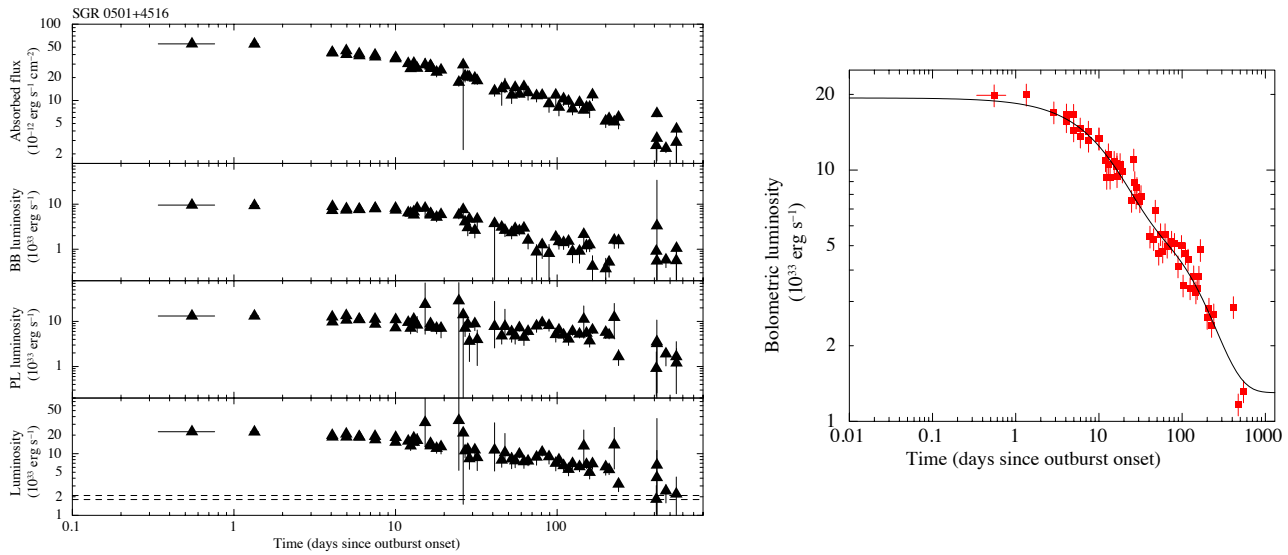


Figure D7. Left-hand panel: temporal evolution of the fluxes and luminosities for the BB+PL model applied to the *Swift* XRT data of SGR 0501+4516. The dashed line marks the approximate value for the quiescent luminosity (see Table 4). A distance of 1.5 kpc was assumed. Right-hand panel: temporal evolution of the bolometric luminosity with the best-fitting decay model superimposed.

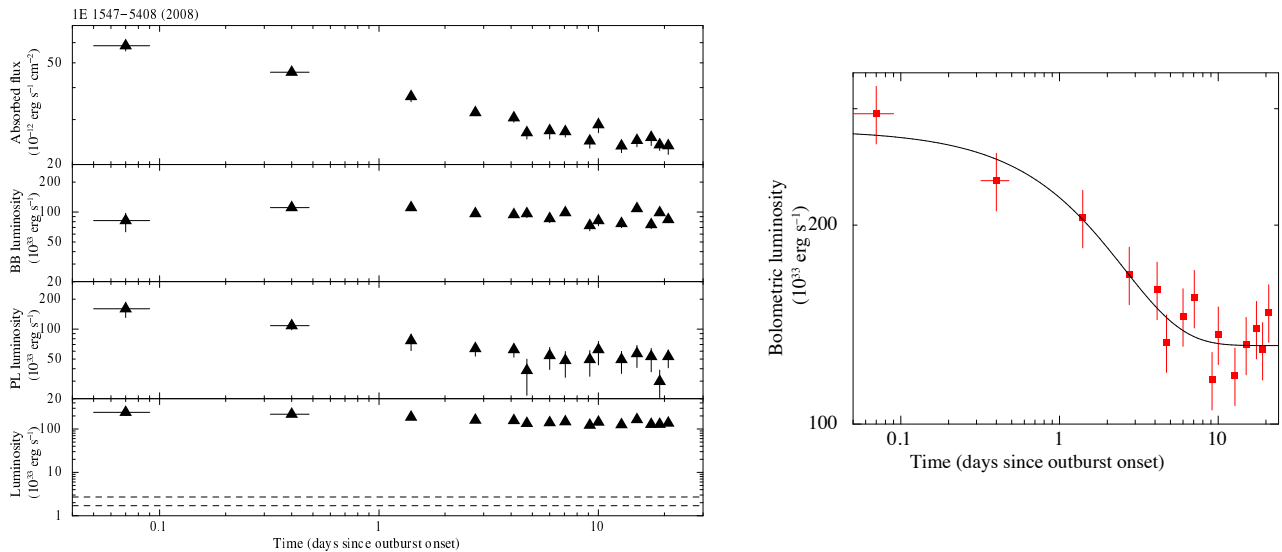


Figure D8. Left-hand panel: temporal evolution of the fluxes and luminosities for the BB+PL model applied to the *Swift* XRT data of the 2008 outburst of IE 1547–5408. The dashed lines mark the 1σ c.l. range for the quiescent luminosity (see Table 4). A distance of 4.5 kpc was assumed. Right-hand panel: temporal evolution of the bolometric luminosity with the best-fitting decay model superimposed.

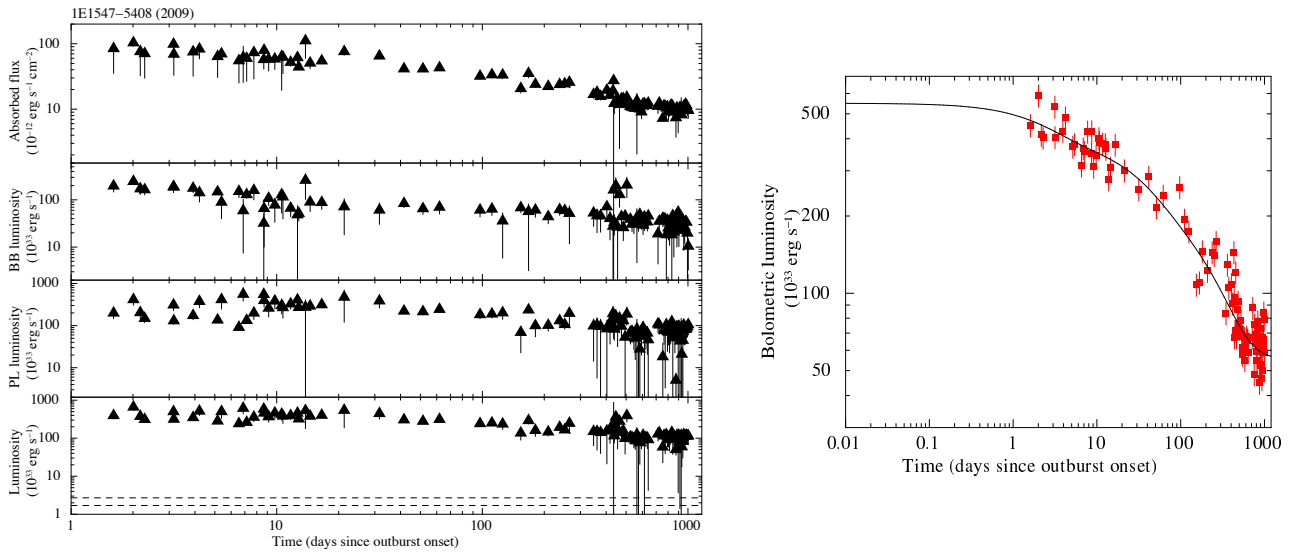


Figure D9. Left-hand panel: temporal evolution of the fluxes and luminosities for the BB+PL model applied to the *Swift* XRT data of the 2009 outburst of 1E 1547–5408. The dashed lines mark the 1σ c.l. range for the quiescent luminosity (see Table 4). A distance of 4.5 kpc was assumed. Right-hand panel: temporal evolution of the bolometric luminosity with the best-fitting decay model superimposed.

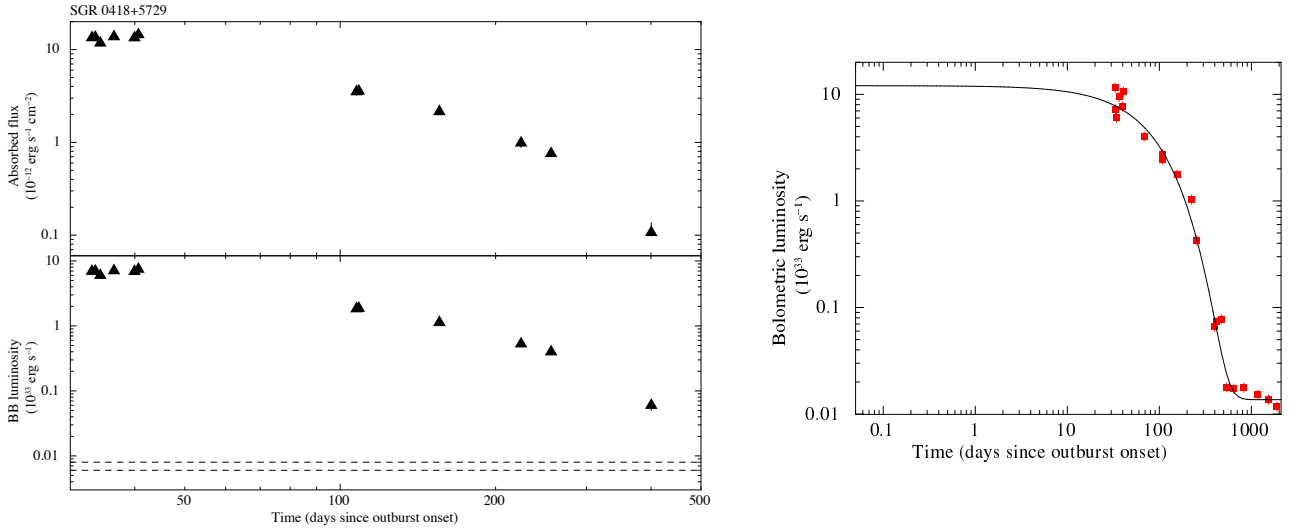


Figure D10. Left-hand panel: temporal evolution of the fluxes and luminosities for the BB model applied to the *Swift* XRT data of the outburst of SGR 0418+5729. The dashed lines mark the 1σ c.l. range for the quiescent luminosity (see Table 4). A distance of 2 kpc was assumed. Right-hand panel: temporal evolution of the bolometric luminosity with the best-fitting decay model superimposed.

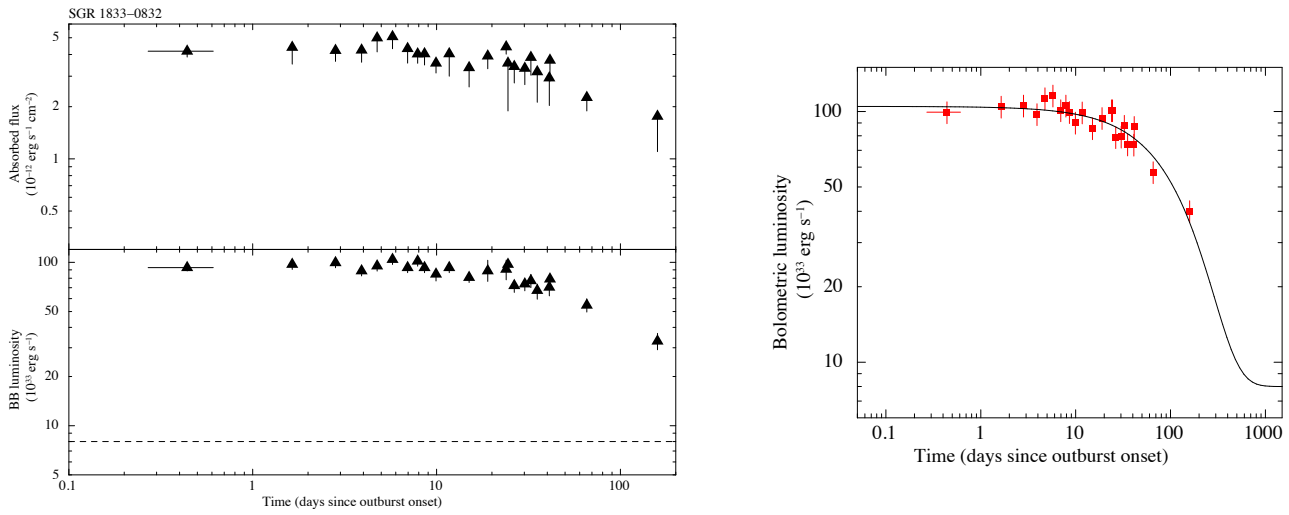


Figure D11. Left-hand panel: temporal evolution of the fluxes and luminosities for the BB+PL model applied to the *Swift* XRT data of the outburst of SGR 1833–0832. The dashed line marks the upper limit (at the 3σ c.l.) for the quiescent luminosity (see Table 4). A distance of 10 kpc was assumed. Right-hand panel: temporal evolution of the bolometric luminosity with the best-fitting decay model superimposed.

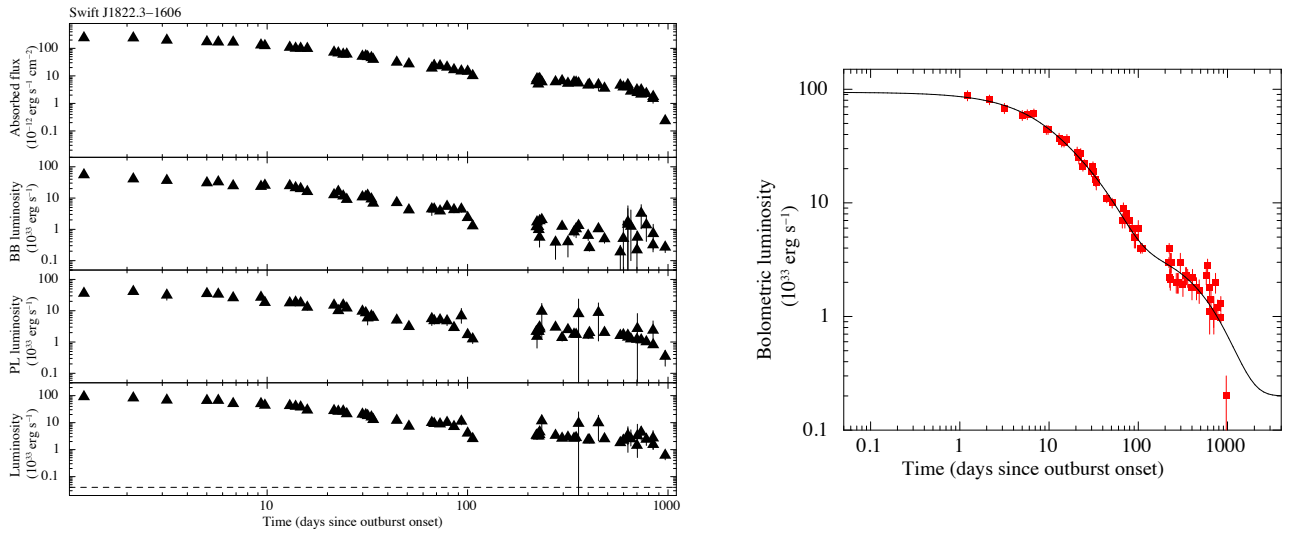


Figure D12. Left-hand panel: temporal evolution of the fluxes and luminosities for the BB+PL model applied to the outburst of Swift J1822.3–1606. The dashed line marks the value for the quiescent luminosity (see Table 4). A distance of 1.6 kpc was assumed. Right-hand panel: temporal evolution of the bolometric luminosity with the best-fitting decay model superimposed.

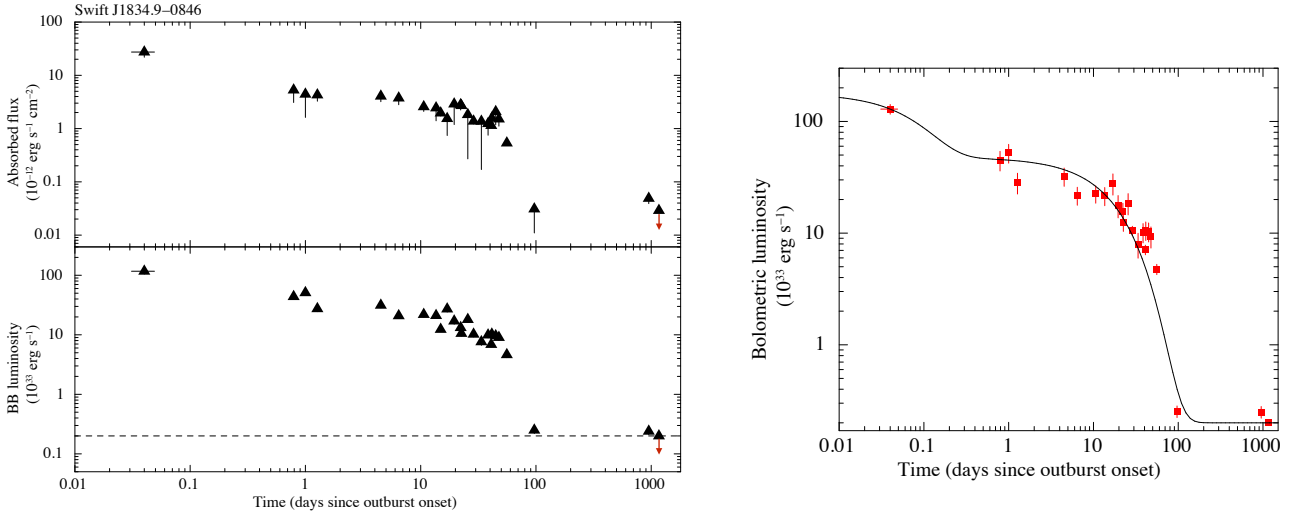


Figure D13. Left-hand panel: temporal evolution of the fluxes and luminosities for the BB model applied to the X-ray data of the outburst of Swift J1834.9–0846. The dashed line marks the upper limit (at the 3σ c.l.) for the quiescent luminosity (see Table 4). Right-hand panel: temporal evolution of the bolometric luminosity with the best-fitting decay model superimposed.

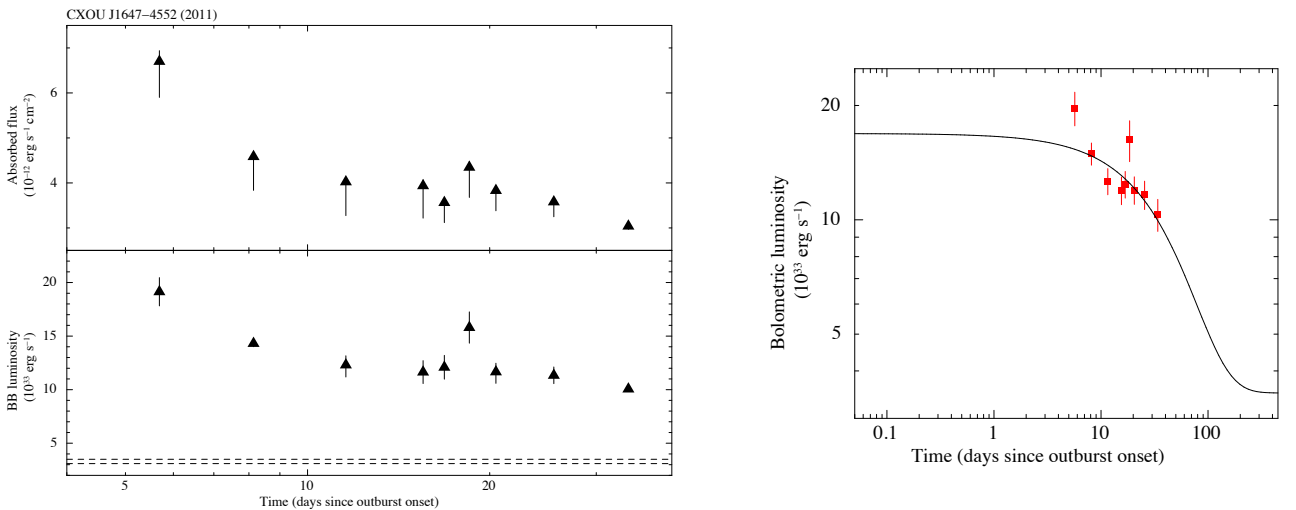


Figure D14. Left-hand panel: temporal evolution of the fluxes and luminosities for the BB model applied to the X-ray data of the 2011 outburst of CXOU J164710.2–455216. The dashed lines mark the 1σ c.l. range for the quiescent luminosity (see Table 4). Right-hand panel: temporal evolution of the bolometric luminosity with the best-fitting decay model superimposed.

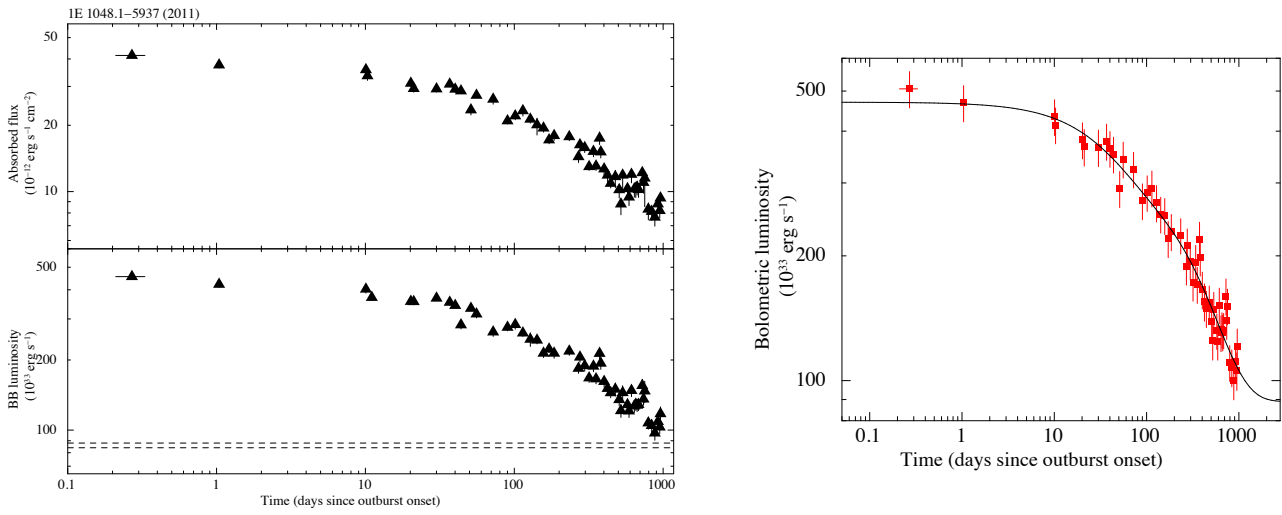


Figure D15. Left-hand panel: temporal evolution of the fluxes and luminosities for the BB model applied to the *Swift* XRT data of the 2011 outburst of 1E 1048.1–5937. The dashed lines mark the 1σ c.l. range for the quiescent luminosity (see Table 4). A distance of 9 kpc was assumed. Right-hand panel: temporal evolution of the bolometric luminosity with the best-fitting decay model superimposed.

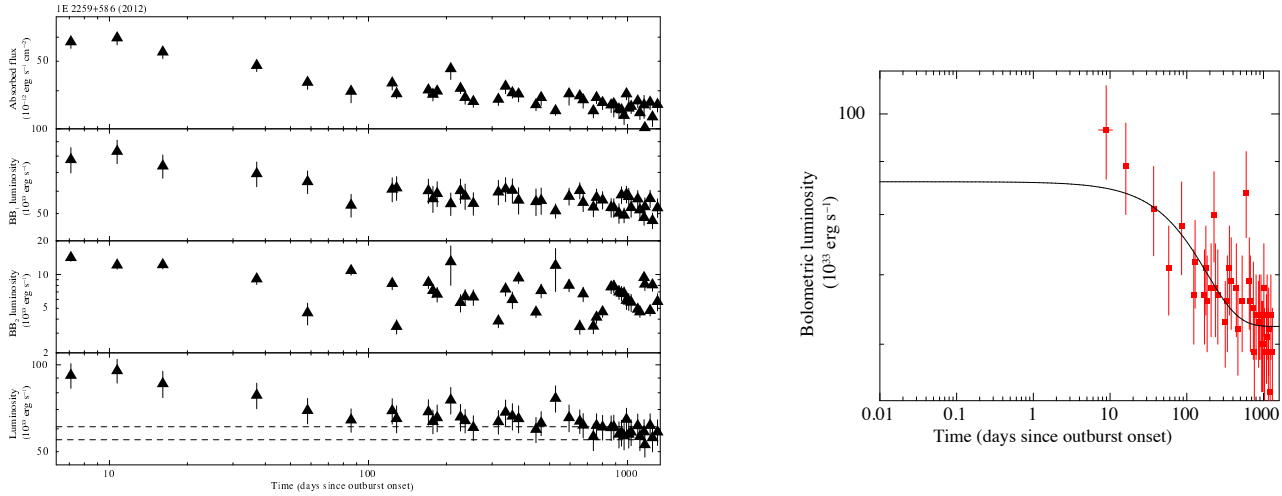


Figure D16. Left-hand panel: temporal evolution of the fluxes and luminosities for the 2BB model applied to the *Swift* data of the 2012 outburst of 1E 2259+586. The dashed lines mark the 1σ c.l. range for the quiescent luminosity (see Table 4). A distance of 3.2 kpc was assumed. Right-hand panel: temporal evolution of the bolometric luminosity with the best-fitting decay model superimposed.

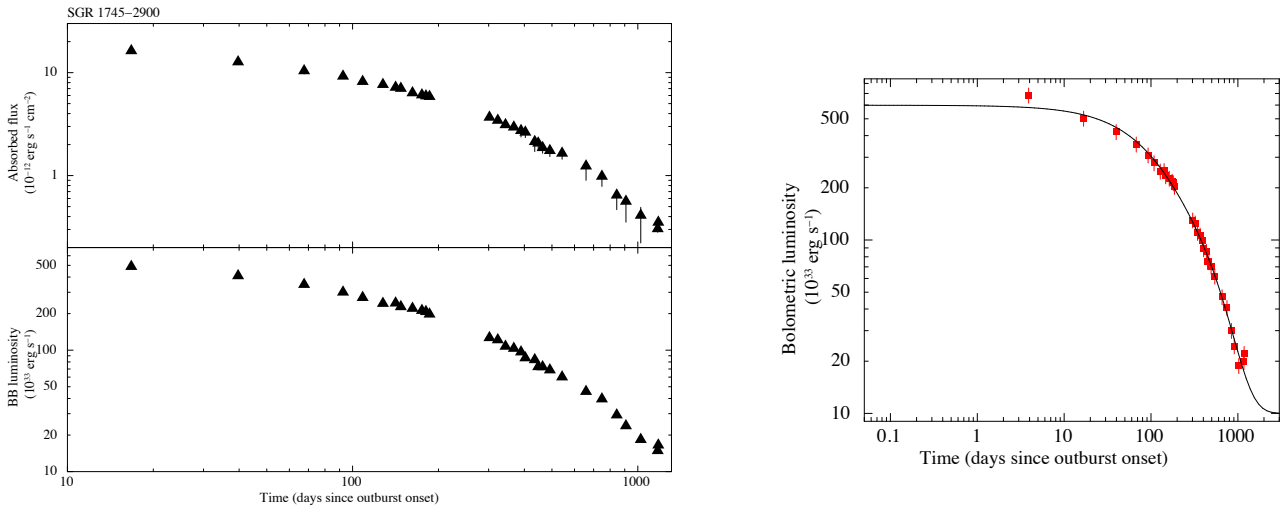


Figure D17. Left-hand panel: temporal evolution of the fluxes and luminosities for the BB+PL model applied to the *Chandra* data of the outburst of SGR 1745–2900. A distance of 8.3 kpc was assumed. Right-hand panel: temporal evolution of the bolometric luminosity with the best-fitting decay model superimposed.

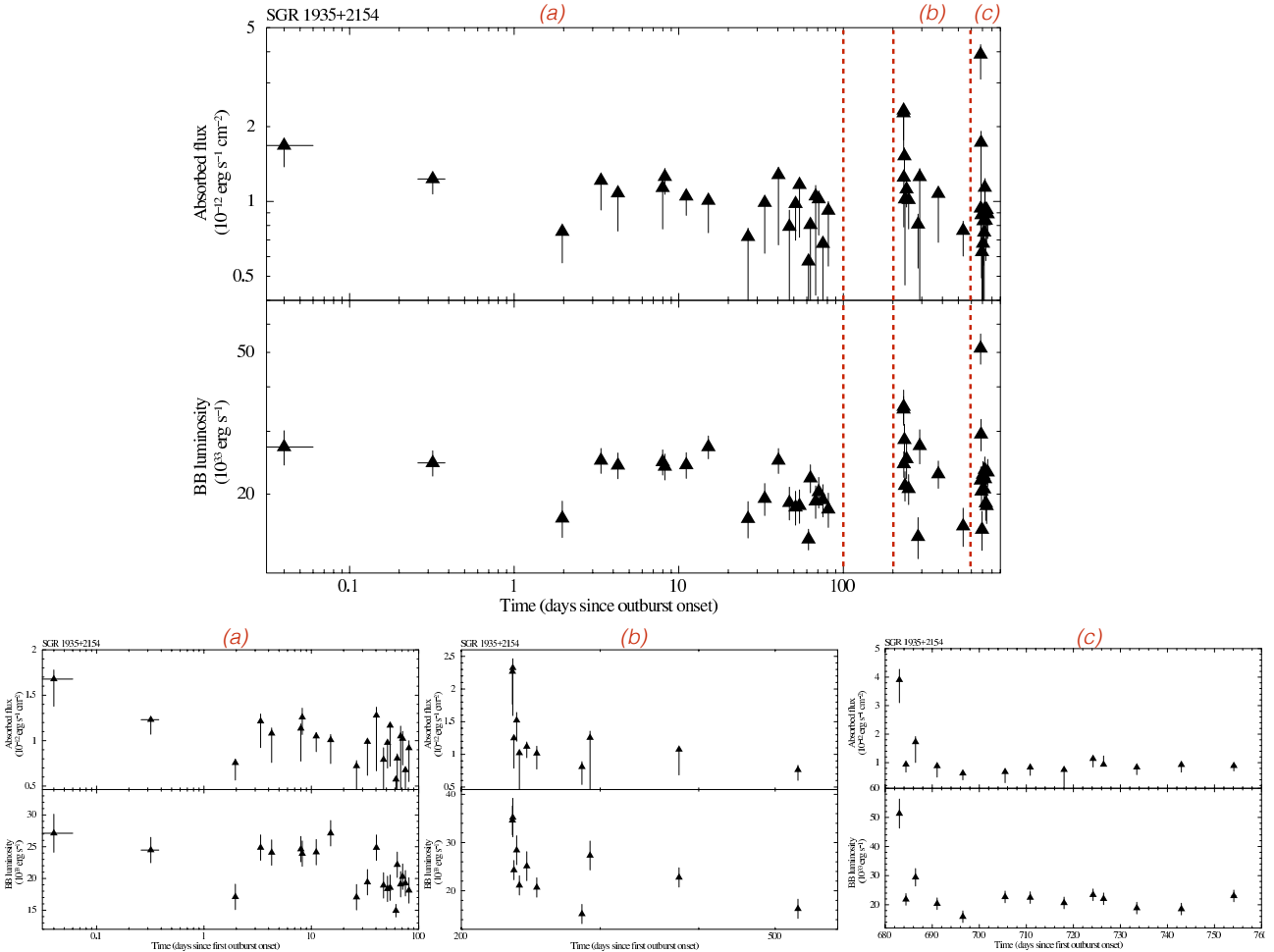


Figure D18. Temporal evolution of the fluxes and luminosities for the BB model applied to the *Swift* XRT data of the outbursts of SGR 1935+2154 (see the bottom panels for a zoom on the individual outbursts). A distance of 9 kpc was assumed (see Israel et al. 2016). The quiescent level is unknown.

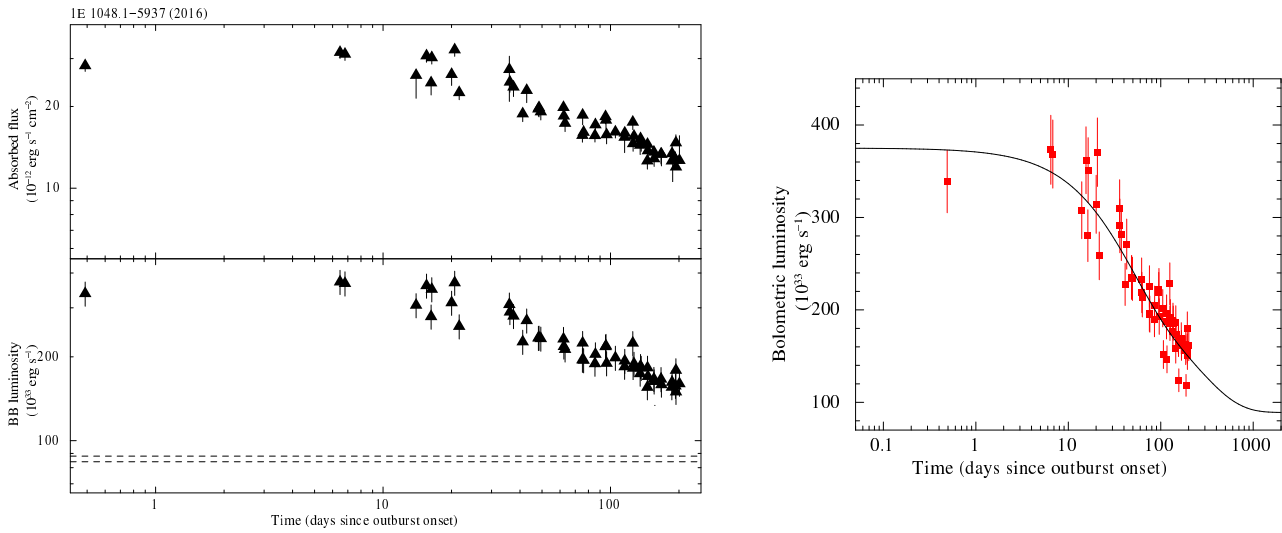


Figure D19. Left-hand panel: temporal evolution of the fluxes and luminosities for the BB model applied to the *Swift* data of the 2016 outburst of 1E 1048.1–5937. The dashed lines mark the 1σ c.l. range for the quiescent luminosity (see Table 4). A distance of 9 kpc was assumed. Right-hand panel: temporal evolution of the bolometric luminosity with the best-fitting decay model superimposed.

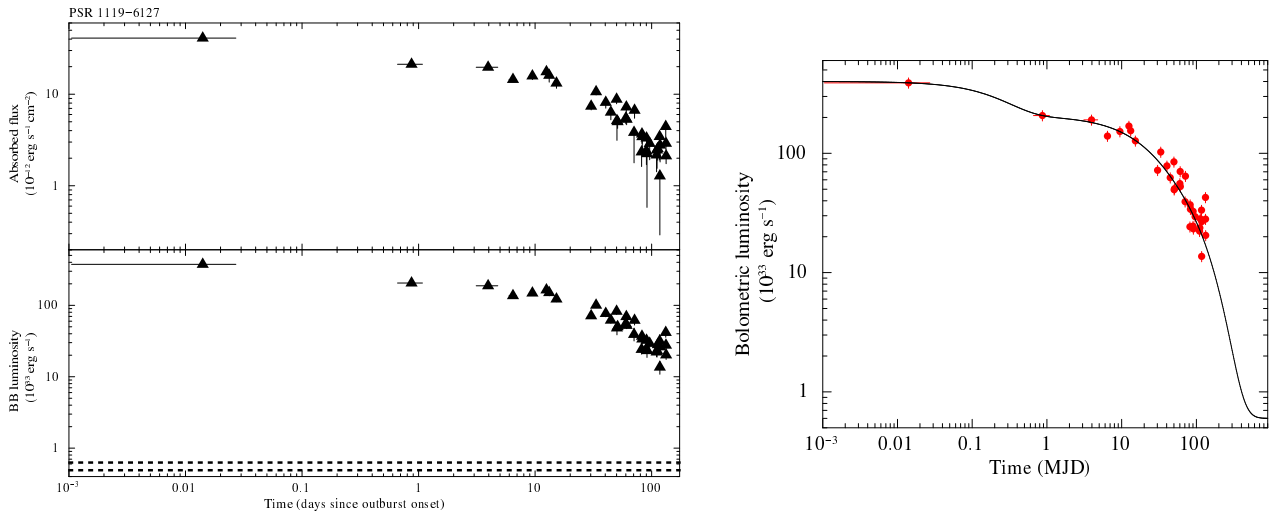


Figure D20. Left-hand panel: temporal evolution of the fluxes and luminosities for the BB model applied to the *Swift* XRT data of the outburst of PSR J1119–6127. The dashed lines mark the 1σ c.l. range for the quiescent luminosity (see Table 4). A distance of 8.4 kpc was assumed. Right-hand panel: temporal evolution of the bolometric luminosity with the best-fitting decay model superimposed.

This paper has been typeset from a $\text{\TeX}/\text{\LaTeX}$ file prepared by the author.